

Dynamics of the Globular Cluster System Associated with M49 (NGC 4472): Cluster Orbital Properties and the Distribution of Dark Matter¹

Patrick Côté², Dean E. McLaughlin³, Judith G. Cohen⁴ and John P. Blakeslee⁵

ABSTRACT

Using the Low Resolution Imaging Spectrometer on the Keck I and II telescopes, we have measured radial velocities for 196 globular clusters (GCs) around M49 (NGC 4472), the brightest member of the Virgo Cluster. Combined with published data, they bring the total number of GCs with measured radial velocities in this galaxy to 263. In terms of sample size, spatial coverage, velocity precision, and the availability of metallicity estimates from Washington photometry, this radial velocity database resembles that presented recently for M87 (NGC 4486), Virgo's cD galaxy and its second-ranked member.

We extract the projected kinematics of the full sample of GCs and of separate subsamples of 158 metal-poor and 105 metal-rich GCs. In agreement with previous results for the global GC kinematics based on smaller datasets, we find that the GC system as a whole exhibits a slow overall rotation that is due almost entirely to a net rotation of the metal-poor GC subsystem alone. In a spatial average, the metal-rich GCs shows essentially no rotation. As a function of galactocentric position, the metal-poor GCs rotate roughly about the photometric minor axis of M49 and at an approximately constant level of $\Omega R \sim 100\text{--}150 \text{ km s}^{-1}$ out to $R \simeq 2R_{\text{eff}}$. The metal-rich GC system shows some evidence (at roughly $1\text{-}\sigma$ significance) for weak rotation ($\Omega R \sim 50 \text{ km s}^{-1}$) beyond $R \gtrsim 0.5R_{\text{eff}}$, also about the galaxy's minor-axis, *but in the opposite direction from the metal-poor GCs*. Outside of $R \sim R_{\text{eff}}$, the line-of-sight velocity dispersion of the metal-poor GCs exceeds that of their metal-rich counterparts by $\sim 50\%$. We also note the presence of a well defined grouping of 10

¹Based on observations obtained at the W.M. Keck Observatory which is operated by the California Association for Research in Astronomy, a scientific partnership between the California Institute of Technology, the University of California, and the National Aeronautics and Space Administration.

²Department of Physics and Astronomy, Rutgers University, 136 Frelinghuysen Road, Piscataway, NJ 08854-8019; pcote@physics.rutgers.edu

³Space Telescope Science Institute, 3700 San Martin Drive, Baltimore, MD 21218; deanm@stsci.edu

⁴California Institute of Technology, Mail Stop 105-24, Pasadena, CA 91125; jlc@astro.caltech.edu

⁵Department of Physics and Astronomy, Center for Astrophysical Sciences, Johns Hopkins University, 3400 North Charles Street, Baltimore, MD 21218; jpb@pha.jhu.edu

metal-rich GCs that are located at opposite poles along the galaxy’s major axis and which appear to be rotating at nearly 300 km s^{-1} about the minor axis. This grouping may be the relic of a past merger or accretion event.

The dynamics of the GC system are modeled by using published catalogs and number counts to define three-dimensional GC density distributions as input to a Jeans-equation analysis. We show that the GC radial velocities alone point unequivocally — and independently of X-ray observations — to the need for a massive dark halo associated with M49 and the Virgo B subcluster around it. We then use a mass model for M49/Virgo B, constructed without reference to any GC data and described in detail in a forthcoming paper, to infer the orbital properties of the M49 globulars. *The GC system as a whole is shown to be consistent with an almost perfectly isotropic velocity ellipsoid.* It is more difficult to draw any firm conclusions on the orbital (an)isotropy of the two metallicity subsamples, owing to the large uncertainties in their individual spatial density profiles and to the poorly observationally defined kinematics of the metal-rich GCs in particular.

After M87, M49 is the second elliptical galaxy for which we have been able to demonstrate velocity isotropy in the globular cluster system overall, when no division based on GC color or metallicity is attempted. Thus, the data for these two galaxies lend support the general *assumption* of isotropy when using GC kinematics to study the dark-matter distribution in early-type galaxies. We also compare the kinematic properties of the GC system of M49 to those of M87, M31, and the Milky Way: the other galaxies for which samples of one hundred or more GC velocities have been accumulated. We argue that, contrary to the traditional view of GCs as non-rotating, or slowly rotating, systems, rotation may in fact be common byproduct of the formation of GC systems. However, the quantitative details of the rotation are still not clear, particularly with regard to the question of possible differences between metal-poor and metal-rich globulars.

Subject headings: galaxies: halos — galaxies: clusters — galaxies: individual (M49) — galaxies: kinematics and dynamics — galaxies: star clusters

1. Introduction

Systems of globular clusters (GCs) can be found in galaxies of virtually all types, from the brightest members of rich galaxy clusters to faint dwarfs in loose groups. Recent studies suggest that, over a range of roughly ten thousand in total luminosity, about 0.25% of the baryonic mass in galaxies takes the form of GCs (Blakeslee, Tonry & Metzger 1997; McLaughlin 1999a; Blakeslee 1999). Given this ubiquity, and the relative ease with which they can be detected and studied in external galaxies, GCs have long been recognized as invaluable probes of galaxy formation

and evolution (see, *e.g.*, Harris 1991 and references therein). To date, observational studies of extragalactic GC systems have most commonly relied on GC specific frequencies, metallicities and, in a few cases, ages, to constrain formation models for GC systems and their host galaxies (*e.g.*, Cohen, Blakeslee & Ryzhov 1998; Kundu *et al.* 1999; Puzia *et al.* 1999; Gebhardt & Kissler-Patig 1999; Larsen *et al.* 2001; Jordán *et al.* 2002; Cohen, Blakeslee & Côté 2003). However, additional insights into the process of galaxy formation may, at least in principle, be gleaned from the dynamical properties of GC systems.

Not only do radial velocity surveys of extragalactic GCs provide a way of tracing out the distribution of dark matter within the host galaxy but, with sufficiently large samples, they offer the hope of measuring directly the shape of the GC velocity ellipsoid. Not surprisingly, the first dynamical studies of an extragalactic GC system focused on the rich GC population of M87=NGC 4486 (*e.g.*, Huchra & Brodie 1987; Mould, Oke & Nemec 1987; Mould *et al.* 1990). However, with radial velocities available for just 44 clusters, only very weak constraints could be placed on the mass distribution — and then only if some assumption (*i.e.*, isotropy) were made *a priori* regarding the GC orbital properties (see Merritt & Tremblay 1993). As Merritt & Tremblay show, dauntingly large samples of order one thousand velocities would be required to constrain, simultaneously and self-consistently in the absence of any other information, both the velocity anisotropy of a GC system and the underlying mass distribution of its parent galaxy.

Only recently have multi-object spectrographs on 4m- and 8m-class telescopes begun to produce anywhere near the large numbers of radial velocities needed to execute such a program in any galaxy. Hanes *et al.* (2001) compiled a radial velocity database of 278 GCs associated with M87 after combining new CFHT velocities with published data from Mould *et al.* (1990), Cohen & Ryzhov (1997) and Cohen (2000). By using an *independent* mass model for M87 and the surrounding “Virgo A” cluster (McLaughlin 1999b), Côté *et al.* (2001) showed from these data that the M87 GC system as a whole has an almost perfectly isotropic velocity dispersion tensor. Considered separately, the metal-poor and metal-rich GC subsystems showed some evidence for weak tangential and radial biases, respectively.

Since M87 contains the richest and most thoroughly studied GC system in the Local Supercluster, it was the obvious first choice for such studies. However, its unique location — at the dynamical center of the Virgo Cluster as traced by both galaxies and intracluster gas — complicates the interpretation of the dynamical properties of its GC system. For instance, Côté *et al.* (2001) noted that the apparent rotation of the metal-poor GCs in M87 might be better described as a velocity “shear” similar to that exhibited on larger scales by the surrounding Virgo cluster *galaxies*. If correct, this would suggest a connection between the M87 GCs and the surrounding population of (mostly dwarf) galaxies, perhaps due to the slow infall of the material onto M87 itself.

If we are to understand which properties of the M87 GC system are generic to early-type galaxies, and which are unique to M87 as a result of its central location in Virgo, then we require

dynamical studies of additional GC systems. An appealing second target is that of M49 (= NGC 4472). As the brightest member of the Virgo cluster, M49 contains ~ 6000 GCs projected within 100 kpc of its center (Lee *et al.* 1998; McLaughlin 1999a; Rhode & Zepf 2001) — just the number expected for an elliptical galaxy with the luminosity of M49 and a “normal” specific frequency. M87, by contrast, has an integrated luminosity about 80% that of M49 but contains some 13,500 GCs projected within 100 kpc of its center. This factor-of-three difference in GC specific frequency between the two galaxies may indicate that some as yet unidentified “second parameter” has played a role in the formation and/or evolution of their GC systems (which otherwise appear remarkably similar; see Côté 2003). However, the relevance of the observed specific frequency difference recently has been called into question by McLaughlin (1999a), who showed that the number of GCs associated with M87 and M49 are both consistent with a “universal” ratio of total GC mass to total baryonic galaxy mass, $\epsilon_{GC} = 0.26 \pm 0.05\%$, once the contribution of X-ray gas mass in each galaxy is included. The principal distinction between the two may then be the fact that M87 sits at the gas-rich center of the main Virgo cluster, while M49 occupies the core of the relatively gas-poor, “Virgo B” subcluster (Binggeli, Tammann & Sandage 1987; Binggeli, Popescu & Tammann 1993; Schindler, Binggeli & Böhringer 1999).

The first radial velocity measurements for M49 GCs were presented by Mould *et al.* (1990), who reported a global velocity dispersion of $340 \pm 50 \text{ km s}^{-1}$ based on a sample of 26 GCs. Building on this work, Sharples *et al.* (1998) presented radial velocities for an additional 47 GCs, found a difference in velocity dispersion between the metal-poor and metal-rich subsystems (320 and 240 km s^{-1} , respectively), and noted the presence of apparent rotation among the metal-poor subsystem. These conclusions were reinforced by Zepf *et al.* (2000), who measured velocities for another 87 GCs and found global velocity dispersions of $356 \pm 25 \text{ km s}^{-1}$ and $221 \pm 22 \text{ km s}^{-1}$ for the metal-poor and metal-rich subsystems, with projected rotation amplitudes of 101 and 15 km s^{-1} for the two populations. These findings are in stark contrast with those for M87, where both GC populations were found to be rapidly rotating, with projected rotation amplitudes of roughly 170 km s^{-1} (Côté *et al.* 2001). Zepf *et al.* also calculated the mass distribution around M49 implied by the velocity-dispersion profile of the full GC system under the *assumption* of orbital isotropy, and showed this to resemble the gravitating-mass profile inferred from X-ray observations (Irwin & Sarazin 1996).

In this paper, we present 196 new radial velocities for GC candidates in M49 obtained with the Keck I and II telescopes. Combining our new radial velocities with those from the literature, we isolate a sample of 263 distinct objects whose colors and radial velocities are consistent with their being GCs belonging to M49. This database is comparable to that presented recently for M87 (Hanes *et al.* 2001) in terms of sample size, spatial coverage (from about 0.1 to 3 effective radii), velocity precision, and the availability of metallicities from Washington photometry. With it, we largely confirm the earlier conclusions summarized above on the global, spatially averaged kinematics of the GC system as a whole and of its metal-poor and metal-rich components. However, with our expanded dataset, we are better able to examine trends in the GC kinematics

as a function of galactocentric position. We see some evidence that the bulk of the metal-rich GC system may in fact rotate—albeit very slowly and with low statistical significance—in a direction opposite to the metal-poor GCs.

We then go on to carry out a dynamical analysis of the three GC samples (full, metal-poor, and metal-rich) based on the Jeans equation following the methodology laid out in McLaughlin (1999b) and Côté *et al.* (2001). We adopt a mass model for M49/Virgo B that we have constructed completely independently of any GC data (McLaughlin & Côté 2003), which allows us to treat the velocity anisotropy of the GC system as a free parameter to be constrained. Our main new result is the demonstration that velocity isotropy suffices fully to describe the velocity ellipsoid of the full globular cluster system (*i.e.*, with no attempt made to separate red GCs from blue). M49 is the second galaxy (after M87) in which we have attempted this sort of analysis, and it is the second in which isotropy has been found to hold to a high level of precision. Quite apart from any bearing that GC dynamics will have on issues of galaxy and globular cluster formation, this suggests that it could very well be reasonable to *assume* orbital isotropy in other GC systems in order to use them as accurate probes of the total mass distribution in early-type galaxies whose mass profiles have not been secured through independent means.

2. Observations, Reductions and the Composite Database

In this section, we describe the criteria used to target candidate GCs for observation with the Low Resolution Imaging Spectrometer (LRIS; Oke *et al.* 1995), the procedures used to acquire and reduce the LRIS spectra, and the methods used to define the composite GC database for M49.

2.1. Sample Selection

Before embarking upon a radial velocity survey, we require a sample of objects whose magnitudes and colors are consistent with those expected for GCs associated with the program galaxy. We used the photometric catalog of Geisler, Lee & Kim (1996) to select candidate GCs for spectroscopic observations. This catalog, which contains GC candidates spread over an area of ~ 256 arcmin² centered on M49, has the benefit that the imaging on which it is based was carried out in Washington C and T_1 filters, a combination that is known to provide excellent metallicity sensitivity for old stellar populations. A total of 1774 GC candidates brighter than $T_1 = 23$ make up the catalog. Since accurate coordinates are needed to design the slit-masks, we combined the GC pixel positions given in Geisler *et al.* (1996) with the coordinates reported by Sharples *et al.* (1998) for 61 GCs to derive astrometric positions for all objects in the Geisler *et al.* (1996) catalog.

2.2. Keck Spectroscopy

Spectra for candidate GCs were obtained in the course of four observing runs at the W.M. Keck Observatory during the 1998, 1999 and 2000 observing seasons. The observing log given in Table 1 records the identification number, observing dates, grating, central wavelength and resolving power for each observing run. A total of 14 LRIS masks were designed, targeting GC candidates in the range $1 \leq (C - T_1) \leq 2.25$ and $20 \leq T_1 \leq 22.25$.⁶ Individual masks contained between 19 and 29 slits, measuring $1''.0$ in width and having a minimum length of $8''.0$. Two different instrumental setups were employed. During runs 1 and 4, we used a 600 line mm^{-1} grating blazed at 5000 \AA and centered at wavelengths of 5200 \AA and 4860 \AA , respectively. During runs 2 and 3, we used a 600 line mm^{-1} grating blazed at 7500 \AA and centered at 8550 \AA . For both configurations, the dispersion was $1.28 \text{ \AA pixel}^{-1}$, giving a spectral resolution of 6 \AA and a wavelength coverage of $\sim 2600 \text{ \AA}$. For each mask, we obtained a pair of exposures ranging between 2400s and 3000s, with comparison spectra for Hg-Ne-Ar-Kr-Xe and quartz lamps taken before and/or after each exposure. On each night, long-slit spectra for 2–4 IAU radial velocity standard stars were obtained during twilight. The extracted, wavelength-calibrated spectra for the candidate GCs were cross-correlated against a master template spectrum created from these spectra. All reductions were performed within the IRAF environment.⁷

Uncertainties for radial velocities measured from spectra acquired during runs 1–3 were derived from the cross-correlation functions using the method of Tonry & Davis (1979). A total of 147 radial velocities were measured during these observing runs; the mean and median uncertainties for these measurements are 104 and 97 km s^{-1} . Spectra obtained during run 4 were typically of the highest quality, as only the brightest GC candidates were selected during this run (*i.e.*, objects with $20.1 \leq T_1 \leq 21.51$). Radial velocities were measured from these spectra following the methods outlined in Cohen & Ryzhov (1997), and representative uncertainties of 25 or 50 km s^{-1} were assigned based on the repeatability of measurements based on multiple strong absorption lines. Including these measurements, the total number of new radial velocities presented here is 196 , with mean and median uncertainties of 86 and 79 km s^{-1} , respectively.

2.3. The Composite Database

Before examining the GC kinematics or carrying out a dynamical analysis, we must combine the new velocities with published measurements to isolate a sample of bona fide GCs. In order to correct for possible systematic differences between radial velocities measured during different

⁶For $\langle C - T_1 \rangle = 1.60$ — the mean color of our 263 GCs — this magnitude range is roughly equivalent to $20.5 \lesssim V \lesssim 22.7$ (Geisler 1996).

⁷IRAF is distributed by the National Optical Astronomy Observatories, which are operated by the Association of Universities for Research in Astronomy, Inc., under contract to the National Science Foundation.

runs, and with different instruments or telescopes, we have transformed the raw velocities from April 1998 and April 1999 (runs 1 and 3, respectively) onto the system defined by our April 2000 observations (run 4) via the relations,

$$\begin{aligned} v_{p,1} &= (1.023)v'_{p,1} + 114 \text{ km s}^{-1} \\ v_{p,3} &= (0.950)v'_{p,3} + 46 \text{ km s}^{-1}, \end{aligned} \quad (1)$$

which were derived from GCs whose velocities were measured during run 4, and either of runs 1 and 3. Since there are no objects in common between runs 2 and 4, no correction was applied to the former dataset. Likewise, no corrections were applied to the velocities of Sharples *et al.* (1998) and Zepf *et al.* (2000), since both datasets show good agreement with our measurements. However, we found it necessary to apply a transformation to the velocities of Mould *et al.* (1990):

$$v_{p,M} = (0.904)v'_{p,M} + 215 \text{ km s}^{-1}. \quad (2)$$

Here $v_{p,M}$ and $v'_{p,M}$ denote the corrected and uncorrected velocities from Mould *et al.* (1990). Both the scale and zero-point terms in this relation agree with those found by Hanes *et al.* (2001) from a comparison of Mould *et al.* (1990) radial velocities for M87 GCs with those measured at Keck and CFHT. Figure 1 compares velocities measured during run 4 with previously published velocities and those obtained during other Keck runs, after applying the above transformations. The dashed line shows the one-to-one relation, while the dotted line indicates the line of best fit.

After transforming the radial velocities onto a common system, the various datasets were merged and a weighted mean velocity, $\langle v_p \rangle$, was calculated from all measurements for each object. Unfortunately, given the galaxy’s low systemic velocity ($v_{\text{gal}} = 997 \pm 7 \text{ km s}^{-1}$ according to the NASA Extragalactic Database) and the large line-of-sight velocity dispersion of the GC system ($\sigma_p \sim 300 \text{ km s}^{-1}$; see §3 below), there is some ambiguity in distinguishing low-velocity GCs from foreground Galactic stars. After some experimentation, we decided to discard those objects with radial velocities outside of the interval,

$$250 \leq \langle v_p \rangle \leq 1950 \text{ km s}^{-1}, \quad (3)$$

where the upper limit was chosen to include a few unambiguous GCs with radial velocities of $\langle v_p \rangle \gtrsim 1900 \text{ km s}^{-1}$. Requiring this range to be symmetric about the systemic velocity would give a low-end cutoff of $\sim 50 \text{ km s}^{-1}$. Such a cutoff would almost certainly result in the inclusion of some halo stars in our sample. If the velocity dispersion of the M49 GC system is $\sim 300 \text{ km s}^{-1}$ then, in a sample of the present size, we expect at most two M49 globulars will fall below the low-end velocity limit in equation (3).

In addition to the above selection on radial velocity, we imposed the condition that true M49 GCs must have colors in the range,

$$1.0 \leq (C - T_1) \leq 2.25 \text{ mag}, \quad (4)$$

and adopted a foreground extinction of $E(B - V) = 0.022$ based on the DIRBE maps of Schlegel, Finkbeiner & Davies (1998). According to the relation of Secker *et al.* (1995), this extinction is

equivalent to $E(C - T_1) = 0.045$. With the color-metallicity calibration of Geisler & Forte (1990), this color range translates to a metallicity interval of $-2.15 \lesssim [\text{Fe}/\text{H}] \lesssim +0.8$ dex. From optical spectroscopy, Beasley *et al.* (2000) showed the M49 GC system to span a range of $-1.6 \lesssim [\text{Fe}/\text{H}] \lesssim 0$ dex, so our selection limits should include the vast majority of GCs in M49.

Figure 2 presents an illustration of these selection criteria. The upper left panel shows color histograms for the 1774 objects with $T_1 \leq 23$ in the the catalog of Geisler *et al.* (1996), as well as for the 276 GC candidates with measured velocities (upper and lower histograms, respectively). The dashed vertical lines show the adopted cutoffs on $(C - T_1)$ color, while the dotted vertical lines indicates the value of $(C - T_1) = 1.625$ used to divide the sample into metal-poor and metal-rich components. According to the color-metallicity relation of Geisler & Forte (1990), this dividing point corresponds to a metallicity of $[\text{Fe}/\text{H}] = -0.68$ dex.⁸

The upper right panel of Figure 2 shows a radial velocity histogram for the same sample of 276 objects. Note that two objects (identification numbers #4497 and #1982 in Geisler *et al.* 1996) fall outside the plotted region. The vertical lines show the adopted cutoffs on radial velocity, while the arrow indicates the velocity of M49 itself. The lower panel of Figure 2 shows the joint constraints on color and radial velocity in the form of a color-velocity diagram. Filled circles show all objects with measured radial velocities, with the exception of #4497 and #1982 which, once again, fall outside the plotted region. The dashed box indicates the adopted selection criteria for color and radial velocity. Note that #2256, the lone circled object inside the boxed region, was not included in the final sample of GCs since two independent velocity measurements for this object differ by more than 700 km s^{-1} . Similarly, two independent measurements for #1982 disagree on whether this object is a true GC or a background galaxy. Discarding it, and the 12 objects that fall outside of the dashed region in Figure 2, brings the final sample to 263 GCs.

The final GC database is given in Table 2. The first five columns of this table record the object identification number from Geisler *et al.* (1996), right ascension, declination, distance from the center of M49 in arcseconds, R , and position angle, Θ , in degrees East of North. In calculating R and Θ , we take the center of M49 to be $\alpha(\text{J2000}) = 12:29:47.5$ and $\delta(\text{J2000}) = +08:00:10.5$ following Sharples *et al.* (1998). The next three columns of Table 2 give the T_1 magnitude, $(C - T_1)$ color, and metallicity based on the color-metallicity relation of Geisler & Forte (1990). Individual radial velocity measurements and their source are presented in the next two columns. The final column gives the weighted mean velocity and uncertainty for each object. The 263 confirmed GCs are listed first in the table; objects classified as foreground stars or background galaxies, and objects with discrepant radial velocity measurements, are given at the end.

The spatial distribution of the final sample of GCs is shown in Figure 3. Metal-poor GCs are indicated by circles, and metal-rich GCs by squares. Open and filled symbols indicate GCs with

⁸Globular cluster metallicities quoted in this paper are $\simeq 0.1$ dex lower than those reported in Geisler *et al.* (1996) since we have adopted the Schlegel *et al.* (1998) extinction of $E(B - V) = 0.022$; Geisler *et al.* (1996) assumed $E(B - V) = 0$.

positive and negative velocity residuals, $\Delta v_p \equiv \langle v_p \rangle - v_{\text{gal}}$, with respect to M49. Symbol sizes are proportional to the absolute value of the residual velocity. The dashed lines show the photometric major and minor axes of the galaxy, with respective position angles of $\Theta = 155^\circ$ and 65° (Kim *et al.* 2000). The large circle shows our determination of galaxy’s effective radius, $R_{\text{eff}} = 3'1$, based on our modeling of the Kim *et al.* surface photometry (see §4.2 below). At our adopted distance of 15 Mpc, $1' = 4.363$ kpc, so that $R_{\text{eff}} = 13.5$ kpc. The full GC sample spans a range of projected galactocentric radius $0'.4 \lesssim R \lesssim 9'.5$, equivalent to $1.9 \lesssim R \lesssim 41$ kpc or $\simeq 0.1\text{--}3R_{\text{eff}}$. A comparison of Figure 3 with Figure 2 of Côté *et al.* (2001) reveals the azimuthal distribution of radial velocity measurements to be somewhat more uniform in M49 than was the case for M87.

3. Kinematics of the Globular Cluster System

Before proceeding with a dynamical analysis of the GC system, we examine its kinematics in a model-independent way. Our aim is to determine the basic parameters that describe the GC system: the average line-of-sight velocity, projected velocity dispersion and, if rotation is important, its amplitude and the position angle of the rotation axis. In this section, we consider both the global kinematic properties of the GC system and their behavior as a function of galactocentric distance.

We fit the observed line-of-sight velocities of the GCs with the function,

$$\langle v_p \rangle = v_{\text{sys}} + (\Omega R) \sin(\Theta - \Theta_0) , \quad (5)$$

where Θ is the projected position angle from a reference axis (taken here to be the North–South direction, such that Θ is measured in degrees East of North) and Θ_0 is the orientation of the rotation axis of the GC system. A complete discussion of the implications of fitting sine curves of this type to projected ($\langle v_p \rangle$, Θ) data is given in Côté *et al.* (2001). Briefly, in so doing we assume that the GC system is spherically symmetric with an intrinsic angular velocity field stratified on spheres, and that the GC rotation axis lies exactly in the plane of the sky (in other words, that the galaxy is being viewed “edge-on”). In principle, the rotation amplitude, ΩR , may then be any function of galactocentric radius R ; fitting equation (5) to our data does not imply an assumption of solid-body rotation or of cylindrical symmetry in the velocity field. Our assumption of spherical symmetry for the GC system is reasonable given its modest projected ellipticity (0.16 according to Lee *et al.* 1998).

3.1. Global Kinematic Properties

Kinematic properties of various subsets of the GC system are summarized in Table 3. The first five columns in this table record the radial range spanned by the cluster sample in question, the median galactocentric distance, $\langle R \rangle$, and number, N , of GCs in each sample, the average radial

velocity (the biweight “location” of Beers, Flynn, & Gebhardt 1990), $\overline{v_p}$, and the rms dispersion about this average (the biweight “scale” of Beers *et al.* 1990), σ_p . Quoted uncertainties represent 68% (1- σ) confidence intervals, determined from a numerical bootstrap procedure in which 1000 artificial datasets are individually analyzed after choosing N clusters at random from the actual subsample under consideration.

Rather than let v_{sys} be a free parameter in the fits of equation (5) to the $\langle v_p \rangle$ - Θ data, we make use of the expectation (confirmed by the results in Column 4 of Table 3) that the average velocity of the GC system should equal that of M49 itself: $v_{\text{sys}} \equiv v_{\text{gal}} = 997 \text{ km s}^{-1}$. In the remaining columns of Table 3, we therefore give the position angle of the rotation axis, Θ_0 , the rotation amplitude, (ΩR), and the dispersion about the best-fit sine curve, $\sigma_{p,r}$, obtained with this constraint placed on v_{sys} .

The first line of each the three subsections of Table 3 presents the results of immediate interest: the global kinematics (*i.e.*, those determined using all appropriate GC data with no discrimination on the basis of galactocentric position) for our full GC sample and for the separate metal-poor and metal-rich subsystems. The remainder of the table applies to further division of the GC data into four wide radial bins; these results are discussed in the next subsection.

The global velocity dispersion of the metal-poor GC system is significantly larger than that of the metal-rich GC system: $\sigma_{p,r} = 342 \text{ km s}^{-1}$ versus 265 km s^{-1} . The global velocity dispersion of the entire GC system, $\sigma_{p,r} = 312 \text{ km s}^{-1}$, is naturally intermediate to these values; it falls somewhat closer to the metal-poor value because that sample is $\sim 50\%$ larger than the metal-rich one. These results are consistent with the previous measurements of Sharples *et al.* (1998) and Zepf *et al.* (2000) based on smaller samples.

Figure 4 plots the individual velocities $\langle v_p \rangle$ against projected position angle Θ for GCs at all galactocentric radii in each of our three metallicity samples. A horizontal, broken line in each panel of this figure marks the velocity of M49, $v_{\text{gal}} = 997 \text{ km s}^{-1}$. It is immediately apparent that the lower dispersion of the metal-rich GC velocities relative to the metal-poor sample stems in part from the absence of even a single GC with $(C - T_1) \geq 1.625$ and $\langle v_p \rangle > 1500 \text{ km s}^{-1}$ — a fact that is also reflected in the empty, upper right-hand corner of the box used to identify globular clusters in the bottom panel of Figure 2. It would appear that this effect is real: if the metal-rich GC velocity dispersion were the same ($\simeq 340 \text{ km s}^{-1}$) as the metal-poor one, then given a sample of 105 metal-rich clusters with $\langle v_p \rangle < 1500 \text{ km s}^{-1}$, we should have also found 8–9 with $\langle v_p \rangle > 1500 \text{ km s}^{-1}$. There is no obvious deficiency in the spatial coverage of the full radial velocity survey that might account for the discrepancy (see Figure 3).

The bold sine curves in the two upper panels of Figure 4 trace the best fits of equation (5) to the entire GC dataset and the metal-poor subset when v_{sys} is held fixed and equal to $v_{\text{gal}} = 997 \text{ km s}^{-1}$ (*i.e.*, with ΩR and Θ_0 given in Columns 6 and 7 of Table 3). For the full sample, the best-fit sine curve has $\Omega R = 53 \text{ km s}^{-1}$ and $\Theta_0 = 105^\circ$. More importantly, we find that $\Omega R = 93 \text{ km s}^{-1}$ and $\Theta_0 = 100^\circ$ for the metal-poor sample, while ΩR is easily consistent with

zero for the metal-rich GC system (hence, the fit to it is not drawn on Figure 4). Thus, averaged over $R \lesssim 3R_{\text{eff}}$ in M49, the metal-rich GC system shows essentially no net rotation, while the metal-poor GC system does. Our result for the metal-poor rotation amplitude is consistent with that of Zepf *et al.* (2000), who found $\Omega R = 101 \text{ km s}^{-1}$ for a sample of 93 blue GCs. Our finding for the metal-rich GC is similarly in keeping with previous analyses (see also Sharples *et al.* 1998).

The position angle of the galaxy’s photometric minor axis is $\Theta_{\text{min}} = 65^\circ$ (Kim *et al.* 2000) and, to within its (large) $1\text{-}\sigma$ errorbars, our fitted rotation axis for the metal-poor GC system is roughly consistent with this. However, it is incompatible at the $1.5\text{-}\sigma$ level with alignment along the photometric *major* axis, which is the solution favored by Zepf *et al.* (2000) for their smaller sample of metal-poor GCs (and their full GC system). Though also similar to the photometric minor axis of M49, the fitted Θ_0 for the metal-rich GCs is effectively meaningless because of the formally null rotation amplitude.

To summarize these *global, spatially averaged* impressions, the average velocity of each GC sample is in very good agreement with that of M49 itself. The global velocity dispersions of the metal-poor and metal-rich samples differ formally by 76 km s^{-1} (although the $2\text{-}\sigma$ errorbars overlap) with the metal-poor GCs being dynamically hotter than their metal-rich counterparts. The GC system appears as a whole to be slowly rotating, but this is purely the result of a net signal from the metal-poor GC subsystem alone; the metal-rich subsystem has none. The velocity dispersions of the full and the metal-poor GC samples are not changed by the correction for rotation, as is apparent from a comparison of the values of $\sigma_{p,r}$ and σ_p in Table 3. Thus, regardless of its statistical significance, rotation is not dynamically important in the M49 GC system. And although it is only loosely determined, the average kinematic axis of the metal-poor GC system does not differ significantly from the photometric minor axis of M49.

3.2. Kinematic Properties as a Function of Projected Radius

Table 3 also presents the GC kinematics that result from further dividing each of the three metallicity samples that we have defined into four broad radial bins: (1) $25'' \leq R < 150''$; (2) $150'' \leq R < 250''$; (3) $250'' \leq R < 350''$; and (4) $350'' \leq R < 570''$. Although the parameters in some bins with small GC numbers must be viewed with caution, the results suggest that there are no drastic changes in the average and rms velocities for each sample.

It is also clear that the lower velocity dispersion of the metal-rich GCs relative to the metal-poor GCs, noted above on the basis of globally averaged kinematics, is only apparent outside of the first radial bin; the metal-poor and metal-rich clusters within $R \leq 150'' \simeq 0.8R_{\text{eff}}$ have the same σ_p and $\sigma_{p,r}$. Figures 5 and 6 demonstrate these points visually. Figure 5 is a plot of individual GC velocities versus projected galactocentric radii, for the entire sample regardless of color and for the metal-poor and metal-rich subsamples separately. Overplotted are large, open squares at the median radius and average velocity of each radial bin, as reported in Columns 2

and 4 of Table 3. The vertical errorbars on these large squares represent the dispersion about the average velocity (Column 5 of Table 3), and the horizontal errorbars delimit the bins themselves. The broken horizontal line through each panel shows the systemic velocity of the galaxy.

The scatter of points about the line $\langle v_p \rangle = 997 \text{ km s}^{-1}$ in the top panel of Figure 5 implies that the average and dispersion of $\langle v_p \rangle$ in the full GC system are indeed essentially constant as functions of galactocentric position — until the region beyond $R \gtrsim 7.5 \simeq 33 \text{ kpc}$, where there is an obvious dearth of high-velocity GCs in our sample. We suspect that this is an artifact of the small sample size, but we cannot rule out with certainty that is a real, physical effect. Until the question can be addressed directly (with still more GC velocity measurements at large radii), any kinematics referring to $R \gtrsim 30 \text{ kpc}$ in the M49 GC system should perhaps be viewed as provisional. Meanwhile, the middle and bottom panels of Figure 5 suggest that the average velocities of the metal-poor and metal-rich subsamples agree separately, at all $R \lesssim 30 \text{ kpc}$, with the galaxy’s systemic velocity. The bottom panel also shows again the absence of any red GCs with $\langle v_p \rangle > 1500 \text{ km s}^{-1}$, and it further reveals a deficit of clusters with $v \lesssim 700 \text{ km s}^{-1}$ at radii $R \gtrsim 3' \sim R_{\text{eff}}$.

We have also constructed “smoothed”, binning-independent radial profiles of average and rms GC velocity, following the procedure of Côté *et al.* (2001): a radial bin of fixed width (chosen here to be $\Delta R = 120'' \simeq 8.7 \text{ kpc}$) is slid through the GC dataset, centering on each globular in turn, and if the number of objects falling within this spatial bin exceeds a minimum of 20 then the biweight average and rms velocity at that position are calculated. (Equation [5] is also fit to the $\langle v_p \rangle$ - Θ data in the bin around every point; the rotation profiles that result are discussed below.) Confidence intervals about the best-fit kinematics are defined by the same bootstrap method that was used to calculate the errorbars in Table 3.

The profile of average GC velocity as a function of galactocentric position that results from this procedure only confirms that \bar{v}_p is constant (inside $R \lesssim 30 \text{ kpc}$) and equal to v_{gal} for each metallicity sample. The velocity dispersion profiles that we obtain are shown in Figure 6 for the full GC system and the metal-poor and metal-rich subsets (filled squares represent the dispersion σ_p of velocities about the average; open squares, the dispersion $\sigma_{p,r}$ about the best-fit sine curve at each point). The horizontal errorbar in the top panel represents the $2'$ width of the sliding radial bin that we have used; only points separated by this distance in these plots are statistically independent. The dotted and solid lines around the points in each panel denote the 68% and 95% confidence intervals for each measurement. All in all, the impressions gleaned from Table 3 and Figure 5 are confirmed in Figure 6.

The velocity dispersion of the full GC system is remarkably constant as a function of radius inside $R \lesssim 30 \text{ kpc}$, never straying by more than 1σ from the global average of 312 km s^{-1} (dashed horizontal line in the top panel). We do not see the gradual decline in $\sigma_p(R)$ with radius that was inferred by Zepf *et al.* (2000) on the basis of a heavily spatially smoothed representation of a smaller dataset. The dispersion profile of the metal-poor GCs is also relatively flat; if anything, it

tends to increase towards larger radii (although this trend is not highly significant). This behavior is opposite to that found by Zepf *et al.* (2000).

The metal-rich GC system is roughly as dynamically hot as the metal-poor GC sample at small galactocentric radii, but it becomes colder beyond $R \sim 3' \simeq 13 \text{ kpc} \simeq 1R_{\text{eff}}$ before possibly increasing slightly again towards $R \sim 6' \sim 2R_{\text{eff}}$. None of this variation, however, is significant at more than the 68% confidence level. Also, note that we are unable to trace the metal-rich GC kinematics beyond $R = 6'$ in the present approach, because there are fewer than 20 red clusters between that radius and $R \simeq 9'5$, whereas every point in Figure 6 relies on data for at least 20 GCs within a $2'$ interval in R . Thus, we have included in the bottom panel of Figure 6 (as a large open square with vertical errorbars corresponding to 68% and 95% confidence intervals) the estimate for σ_p in the outermost radial bin of Table 3. Zepf *et al.* (2000) presented a smoothed velocity dispersion profile for the metal-rich GC system that appears somewhat flatter than ours inside $R \lesssim 6'$.

The “rotation-corrected” GC velocity dispersions, $\sigma_{p,r}$, are nowhere, in any of the three metallicity samples, dramatically different from the dispersions, σ_p , about the average velocity. This is yet another demonstration that rotation is dynamically unimportant in the globular cluster system of this galaxy. Nevertheless, it is of some interest to consider the rotation properties of the GCs as a function of galactocentric radius, as they appear to be somewhat more subtle than suggested by the global view of §3.1, in which the metal-poor GCs show a statistically significant, if small, net rotation while the metal-rich ones do not.

We show in Figure 7 plots of GC velocity versus projected position angle, for each of the four radial bins defined in Table 3. A broken, horizontal line in each panel again indicates the overall velocity of M49, $v_{\text{gal}} = 997 \text{ km s}^{-1}$, and the bold sine curves trace the best fits of equation (5) to the metal-poor (filled points and solid curves) and metal-rich (open points and broken curves) GCs in each bin. (The fit parameters are again those in Columns 6 and 7 of Table 3.) This gives some indication of the quality of the sine fits we are able to achieve with the data so finely divided, and the extent to which such fits are even feasible given the data. Note that we do not present any rotation fit for the metal-rich GCs in the bin $250'' \leq R < 350''$, for reasons that we shall discuss shortly.

For more detail, Figures 8–10 plot the runs of ΩR and Θ_0 with galactocentric radius in the full GC system and in the metal-poor and metal-rich subsystems, obtained during the same “smoothing” process that resulted in the velocity dispersion profiles in Figure 6.

Figure 8, which presents the results for our full sample of 263 GCs, is included primarily for completeness, as it is somewhat more profitable to consider the metal-poor and metal-rich subsamples separately. Worthy of note here, however, are the large uncertainties at every radius in the Θ_0 and ΩR determinations (as in Figure 6, 68% and 95% confidence intervals are indicated here), even when our full dataset is analyzed in bins as wide as $2'$. Much larger numbers of GC velocities will be required if the rotation properties of the system are to be characterized

point-by-point in this way with any real confidence.

Figure 9 shows the rotation axis and amplitude as functions of R in the metal-poor GC system only. Inside $R \lesssim 25$ kpc, Θ_0 is essentially constant and generally within 1σ of the photometric minor axis of M49 (drawn as the bold, solid lines in the top panel of Figure 9). Indeed, it is made clear in this plot that the rotation axis of the metal-poor GC system by and large falls closer to the galaxy’s minor axis than its major axis. The ΩR profile is similarly rather flat, holding roughly steady (again, within the $1\text{-}\sigma$ uncertainties) at the level of $100\text{--}150$ km s $^{-1}$. It is nonzero almost everywhere at better than the 68% confidence level, but less than the $2\text{-}\sigma$ level. The obvious exception is at very small radii, $R < 2'$. The strong negative rotation suggested in the innermost radial bin of Table 3, and illustrated in the top panel of Figure 7, is seen here simply not to be significant; it is an artifact of the small sample size.

It could be of considerable interest that the metal-poor rotation axis appears to switch suddenly to align with the photometric *major* axis of M49 (indicated by the bold, dashed lines in the top panel of Figure 9) at the largest radii probed by our sample, $R \gtrsim 6'$. This is clearly responsible for a similar, though slightly more muted, trend in the full GC system (Figure 8). However, since every point plotted in these graphs incorporates all GC data from within $1'$ on either side of it, the measurements beyond $6'$ all rely on some velocities from $R > 7' \simeq 30$ kpc, which is the regime that was mentioned as somewhat suspect on the basis of Figure 5. A larger dataset is required to confirm this potential major-axis rotation at large radii in the metal-poor GC system.

Figure 10 presents the analysis as applied to the metal-rich GC system. Since the “smoothed” profiles cannot be calculated beyond $R \gtrsim 6'$ in this case, a single large data point is used to represent the sine-fit parameters for all metal-rich GCs with $350'' \leq R < 570''$ (18 kpc $\lesssim R \lesssim 41$ kpc) together. At small radii $R \lesssim 4'$, the axis of GC rotation is poorly determined but is consistent, within the 95% confidence bands, with alignment everywhere along the photometric minor axis (or coincidence with the formal best fit, $\Theta_0 = 100^\circ$, to the metal-poor GC rotation). Notably, and despite the vanishing net rotation of the globally averaged metal-rich GC sample, ΩR at these small radii differs from zero at the $\sim 1\text{-}\sigma$ level and is of *opposite sign* to that found for the metal-poor GCs. Thus, there is marginal evidence for some counter-rotation in the metal-rich GC subsystem, relative to the metal-poor one, inside $R \lesssim 4'.5 \sim 1.5R_{\text{eff}}$ in M49.

The situation appears in Figure 10 to change suddenly around $R \sim 4'.5$, with ΩR becoming positive, large, and significant at the $> 95\%$ confidence level. The rotation axis also appears to come sharply into line with the minor axis of the galaxy. However, the reversion to a negative rotation of much lower significance in the outermost bin of our sample suggests that this effect may be related to some curiosity in the data between $4' \lesssim R \lesssim 6'$. Indeed, inspection of the metal-rich GC distribution in the third panel of Figure 7 shows immediately that the azimuthal sampling of metal-rich GC velocities in this radial range is highly incomplete: all but a few data points lie within a couple tens of degrees of the photometric major axis on opposite sides of the

galaxy ($\Theta = 155^\circ$ and 335°).

The strong “prograde” rotation that suddenly appears in Figure 10 comes entirely from a small group of 10 metal-rich clusters, all contained in the thin annulus $302'' \leq R \leq 337''$ ($22.0 \text{ kpc} \leq R \leq 24.5 \text{ kpc}$) and located at opposite poles of the photometric major axis. In $(\langle v_p \rangle, \Theta)$ space, these GCs trace almost perfectly (with a dispersion of only $\sim 100 \text{ km s}^{-1}$) a sine curve with peak and trough at the position angles of the major axis and an amplitude $\Omega R = +300 \text{ km s}^{-1}$. Because all 10 objects are so closely spaced around their median radius of $\langle R \rangle = 319''$, all 10 are included in every point with $4'5 \leq R \leq 6'0$ in Figure 10, and they are thus entirely responsible for the behavior in those portions of the smoothed Θ_0 and ΩR profiles (recall that every point in these profiles is computed using all GC velocities within $\pm 1'$ of the indicated position). Similarly, the same 10 objects single-handedly erase a (weak) net negative-rotation signal from the rest of the metal-rich GC system.

In the top panel of Figure 11, we show the velocity-position curve of the GCs in question. The sine fit indicated has $v_{\text{sys}} = 997 \text{ km s}^{-1}$ and $\Theta_0 = 65^\circ$ fixed, and a fitted amplitude of $\Omega R = 296 \text{ km s}^{-1}$ ($2\text{-}\sigma$ lower limit: 145 km s^{-1}). The ID’s of the ten objects from Table 2 are: 677, 830, 929, 1508, 6905, 7043, 7894, 8164, 8740, and 8890. Aside from their galactocentric radius, there is no obvious, common characteristic to distinguish them from any other data, although we do note that five of the 10 clusters have super-solar metallicities, and that the one [#6905] falling farthest from the fitted sine curve is also the most metal-poor.

The bottom panel of Figure 11 is an attempt to delineate the rotation curve of the metal-rich GC system with the clusters at $302'' \leq R \leq 337''$ isolated from the rest of the sample. On the basis of the smoothed profiles at $R < 4'$ and the single-bin datapoints at $R > 6'$ in Figure 10, we fix the position angle of the rotation axis to coincide with the galaxy minor axis for definiteness here ($\Theta_0 \equiv 65^\circ$). The same smoothing procedure is applied as before, to fit for ΩR in equation (5), but only using GC data interior to $R \leq 300''$. The result, shown as the small, solid squares between $2' \lesssim R \leq 4'$ in Figure 11 (but incorporating data from $1' \lesssim R \leq 5'$), can hardly be called a profile any longer, as now only the two endpoints are independent. It does, however, give an impression of the (small) impact that a particular choice of bin boundaries has on the derived GC rotation amplitude. The open square at $R = 5'3 = 23.2 \text{ kpc}$ represents the clusters in the top panel of Figure 11, while the open square at $R = 7'25$ is at the rotation amplitude fit to the GCs with $350'' \leq R < 570''$ with $v_{\text{sys}} = 997 \text{ km s}^{-1}$ and $\Theta_0 = 65^\circ$ both held fixed.

As we suggested just above, the removal of the small group of apparently rapidly rotating clusters around $R = 22\text{--}24.5 \text{ kpc}$ leaves a metal-rich GC system that, beyond $R \sim 2' \simeq 0.6R_{\text{eff}}$ appears to be rotating — albeit slowly, and with less than impressive statistical significance — roughly around the minor axis in a direction counter to the metal-poor GC system. Whether this feature is real or not — and, indeed, whether the highly contaminating influence of the 10 isolated GCs is an unlucky byproduct of sampling statistics or an indication of a real, physical grouping of newly recognized objects — can only be decided by the acquisition of further velocity data.

Additional observations of these clusters would certainly be useful, as they may be the relic of a past merger or accretion event. In any case, it is clear that globally averaged kinematics are bound to miss potentially significant and complex radial variations within a GC system. Any arguments about GC and galaxy formation and evolution that draw only on globally averaged rotation should be regarded in this light.

We have checked that excluding the aberrant metal-rich GCs does not lead to significant changes (no more than a few km s^{-1} for velocities, or degrees in Θ_0) in the derived kinematics of the full GC velocity sample, either in Table 3 or Figure 8. It does, of course, alter the global rotation of the metal-rich GC sample from that quoted in Table 3, and the revised numbers are given in Table 4 below (§5). Their exclusion also leaves too few GCs in the bin $250'' \leq R < 350''$ to derive a reliable rotation solution there, which is why none is given in Table 3. However, the spatial sampling of points around an annulus at a given radius should not affect grossly the estimation of a velocity dispersion there, and thus the metal-rich $\sigma_p(R)$ profile in the bottom panel of Figure 6 (which excludes no data) is likely still reasonable enough—although the points between $4' \lesssim R \lesssim 6'$ should obviously be regarded with due caution.

Finally, we plot in Figure 12 the absolute value of the ratio of rotation amplitude to velocity dispersion as a function of radius in the full GC system, the metal-poor subsystem, and the metal-rich sample. Note that the latter profile corresponds to the rotation solutions as obtained in the bottom panel of Figure 11, rather than Figure 10. For the metal-poor subsystem, a constant $|\Omega R|/\sigma_p \simeq 0.3\text{--}0.4$ could be taken as an adequate description, within the $1\text{-}\sigma$ uncertainties, of the metal-poor GC data at all radii (except perhaps around $7' \simeq 30$ kpc). Thus, as the low statistical significance of all the rotation amplitudes has already suggested, rotation is not an important source of dynamical support in the M49 GC system.

The weighted average for the full GC system, from either of Tables 3 or 4, is $|\Omega R|/\sigma_p \sim 0.15\text{--}0.2$. A similar, though perhaps slightly higher, ratio also applies in the metal-poor GC system. And, with only the exception of the 10 extreme clusters at $R \simeq 23.2$ kpc, the metal-rich GC system is consistent everywhere with $|\Omega R|/\sigma_p \sim 0.1\text{--}0.2$. In the next section, we therefore explore the dynamics of the M49 GC system through a Jeans-equation analysis that ignores altogether the presence of rotation. Nowhere should this expose us to uncertainty or error at any more than a $\sim 10\%$ level.

4. Dynamical Models

We make the simplifying assumption of spherical symmetry to proceed with a dynamical analysis based on the Jeans equation in the absence of rotation:

$$\frac{d}{dr} n_{\text{cl}}(r) \sigma_r^2(r) + \frac{2 \beta_{\text{cl}}(r)}{r} n_{\text{cl}}(r) \sigma_r^2(r) = -n_{\text{cl}}(r) \frac{GM_{\text{tot}}(r)}{r^2}. \quad (6)$$

Here $n_{\text{cl}}(r)$ is the three dimensional density profile of the GC system; $\sigma_r(r)$ is its intrinsic velocity dispersion in the radial direction; $\beta_{\text{cl}}(r) \equiv 1 - \sigma_{\theta}^2(r)/\sigma_r^2(r)$ is a measure of its velocity anisotropy; and $M_{\text{tot}}(r)$ is the total gravitating mass enclosed within a sphere of radius r .

Our analysis of the M49 GC system parallels that undertaken for M87 by Côté *et al.* (2001), and it differs from the approach normally taken in dynamical studies of extragalactic GC systems (*e.g.*, Huchra & Brodie 1987; Mould *et al.* 1990; Cohen & Ryzhov 1997; Sharples *et al.* 1998; Kissler-Patig & Gebhardt 1998; Zepf *et al.* 2000), in which the measured line-of-sight velocity dispersions are used to infer the deprojected profile $\sigma_r(r)$ so as to solve equation (6), under the assumption of orbital isotropy [$\beta_{\text{cl}}(r) \equiv 0$], for the gravitating mass distribution $M_{\text{tot}}(r)$. We opt instead to determine a mass model for M49 and the Virgo B subcluster *a priori* (and independently of any GC data) and then to use this model, along with three-dimensional GC density profiles that fit published number counts, to solve equation (6) for the velocity dispersion profile $\sigma_r(r)$ under a variety of assumptions on the velocity anisotropy $\beta_{\text{cl}}(r)$. These model profiles are then numerically projected for comparison with the observed $\sigma_p(R)$ profiles obtained in §3.2, in order to examine more directly what range of $\beta_{\text{cl}}(r)$ is compatible with the data. (The observed dispersion profiles are still too noisy to be deprojected and used to solve directly for $\beta_{\text{cl}}(r)$ with any confidence.) Romanowsky & Kochanek (2001) present an analysis of the M87 GC system that employs different methodology for the same basic goal.

For later reference, the relevant projection integrals are

$$\sigma_p^2(R) = \frac{2}{N_{\text{cl}}(R)} \int_R^\infty n_{\text{cl}} \sigma_r^2(r) \left(1 - \beta_{\text{cl}} \frac{R^2}{r^2}\right) \frac{r dr}{\sqrt{r^2 - R^2}}, \quad (7)$$

where the surface density profile $N_{\text{cl}}(R)$ is related to the three-dimensional $n_{\text{cl}}(r)$ by

$$N_{\text{cl}}(R) = 2 \int_R^\infty n_{\text{cl}}(r) \frac{r dr}{\sqrt{r^2 - R^2}}. \quad (8)$$

Throughout this Section, we discuss all distances, densities, masses, and luminosities in physical units that assume a distance of 15 Mpc to M49.

4.1. Density Profiles for the GC System

Figure 13 shows the projected number-density profiles, $N_{\text{cl}}(R)$, for GCs of all colors (metallicities), taken from the comprehensive and independent studies of McLaughlin (1999a) and Rhode & Zepf (2001). These authors have already corrected the GC densities to remove contamination by foreground stars and background galaxies, and to account for GCs not directly counted because they are fainter than the limiting magnitudes of their surveys (this latter correction assumes the GC luminosity function, or number of clusters per unit magnitude, to have a Gaussian shape with a peak at $V = 23.75$ mag and a dispersion $\sigma = 1.3$ mag). Thus, the data

points shown here genuinely reflect the total number of GCs per unit area on the sky as a function of projected radius in M49.

For use in equation (6), we treat both sets of data together as a single number-density profile, to which we fit the projections of two simple three-dimensional density functions. Shown as the bold, solid curve in Figure 13 is the best-fit projection of the density profile suggested by Navarro, Frenk, & White (1997) for dark-matter halos, *i.e.*, $n_{\text{cl}} = n_0(r/b)^{-1}(1 + r/b)^{-2}$:

$$n_{\text{cl}}(r) = 0.19 \text{ kpc}^{-3} (r/11.7 \text{ kpc})^{-1} (1 + r/11.7 \text{ kpc})^{-2}, \quad (9)$$

with (correlated) uncertainties of $\pm 0.07 \text{ kpc}^{-3}$ in the normalization and $\pm 1.5 \text{ kpc}$ in the scale radius

The bold, dashed line in Figure 13 shows the best-fit projection of one of the simple family of galaxy models developed by Dehnen (1993): $n_{\text{cl}}(r) = n_0(r/b)^{-\gamma}(1 + r/b)^{\gamma-4}$. We assume $\gamma = 0$ and find

$$n_{\text{cl}}(r) = 0.40 \text{ kpc}^{-3} (1 + r/16.7 \text{ kpc})^{-4}, \quad (10)$$

with correlated uncertainties of $\pm 0.16 \text{ kpc}^{-3}$ in the normalization and $\pm 2.3 \text{ kpc}$ in the scale radius.

The reduced χ^2 values of these two fits are comparable. We prefer the Navarro *et al.* (NFW) form of equation (9), because the total baryonic mass density (stars and X-ray gas) at large radii in M49 appears to fall off roughly as r^{-3} (McLaughlin & Côté 2003), and we expect the GC system to follow this behavior (McLaughlin 1999a). However, the particular form of the density profile in equation (10) was chosen specifically for its contrasting asymptotic behavior at both small and large galactocentric radii; with it, we can check directly the extent to which the functional form of $n_{\text{cl}}(r)$ used in the Jeans equation (6) might influence our conclusions on the GC dynamics.

We wish also to model the dynamics of the metal-poor and metal-rich GC subsystems separately. To define individual density profiles for them, we make use of the catalog of Lee *et al.* (1998), which includes positions and Washington ($C - T_1$) colors for ~ 2000 GC candidates around M49. Although Lee *et al.* (1998) themselves presented separate density profiles for the metal-poor and metal-rich GCs, the criteria they used to divide their sample by color differ slightly from those adopted here, in §2.3. We therefore use their catalog directly to re-derive the surface density profiles of those objects with $1 \leq (C - T_1) < 1.625$ and $1.625 \leq (C - T_1) < 2.25$. We count only the points that are also brighter than $T_1 \leq 23$, to which magnitude the Lee *et al.* catalog is better than 97% complete. Because the catalog includes GCs only out to $R \simeq 8'$ from the center of M49, whereas the full GC system is known to extend to $R \gtrsim 20'$ (Harris & Petrie 1978; Rhode & Zepf 2001), we are unable to measure directly the level of its contamination by stars and background galaxies. The exact choice of background is, however, constrained by the fact that the corrected number density profile for all colors $1 \leq (C - T_1) < 2.25$ should be consistent with the shape of $N_{\text{cl}}(R)$ in Figure 13. The total background density, to the limiting magnitude of $T_1 = 23$, estimated in this way is $N_b \simeq 2.0 \pm 0.2 \text{ arcmin}^{-2}$, or $0.11 \pm 0.01 \text{ kpc}^{-2}$. We then *assume* that the contaminating backgrounds to be subtracted from the separate metal-poor and metal-rich GC

density profiles are 60% and 40% of the total N_b . This 3:2 ratio is somewhat arbitrary, but it is consistent with that predicted by the IAS Galaxy model (Bahcall & Soneira 1980; Bahcall 1986) for foreground star counts to $T_1 = 23$, in our color ranges, in the direction towards M49.

Having thus obtained corrected, metal-poor and metal-rich GC surface density profiles, we fit each with projections of the same two three-dimensional functions that we fit to the full GC system. The results are shown in Figure 14. The top panel presents fits of the NFW function, with an adopted background of $N_b = 2.2 \text{ arcmin}^{-2}$. For the metal-poor and metal-rich GC samples in turn,

$$\begin{aligned} n_{\text{cl}}^{\text{MP}}(r) &\propto (r/20.7 \text{ kpc})^{-1}(1 + r/20.7 \text{ kpc})^{-2} \\ n_{\text{cl}}^{\text{MR}}(r) &\propto (r/5.54 \text{ kpc})^{-1}(1 + r/5.54 \text{ kpc})^{-2} . \end{aligned} \quad (11)$$

The dashed curves running through the open datapoints in the top panel of Figure 14 are the projections of these functions. The bolder dashed curve is their sum; it agrees reasonably well both with the observed density profile of metal-poor and metal-rich GCs *combined* in the catalog of Lee *et al.* (1998) (filled circles), and with the NFW fit (eq. [9]; the bold, solid line) to the combined data of McLaughlin (1999a) and Rhode & Zepf (2001) in Figure 13.

The bottom panel of Figure 14 shows our projected fits of the Dehnen (1993) density model to the metal-poor and metal-rich GC systems,

$$\begin{aligned} n_{\text{cl}}^{\text{MP}}(r) &\propto (1 + r/20.1 \text{ kpc})^{-4} \\ n_{\text{cl}}^{\text{MR}}(r) &\propto (1 + r/9.51 \text{ kpc})^{-4} , \end{aligned} \quad (12)$$

where the adopted background in this case is $N_b = 1.9 \text{ arcmin}^{-2}$. Again, the sum of the two fits is shown as the bold, dashed curve. It is fairly consistent with the observed total GC surface densities and with the Dehnen-model fit of equation (10).

Unlike the case for the full GC system in Figure 13, we do not consider the density profiles for the GC metallicity subsample to be particularly well constrained. The limited spatial coverage of the Lee *et al.* catalog leaves much room for erroneous extrapolations to larger radii, and the lack of direct background density estimates makes the $N_{\text{cl}}(R)$ estimates for the metal-poor and metal-rich subsystems too uncertain for our taste even at directly observed radii. It is nevertheless necessary to specify separate density profiles for the subsamples if their dynamics are to be modeled individually. Note that estimates of the absolute normalizations of $n_{\text{cl}}^{\text{MP}}(r)$ and $n_{\text{cl}}^{\text{MR}}(r)$ are not required in the following analysis, since these cancel out of equation (6).

4.2. The Need for an Extended Dark-Matter Halo in M49/Virgo B

Before going on to constrain the orbital parameters of the GCs in M49, we make a brief aside regarding the evidence for dark matter in M49 and the Virgo B subcluster around it, about which

various claims have been made over the years. Mould *et al.* (1990) argued on the basis of radial velocities for 26 GCs that the galaxy does indeed contain a dark halo, but they were unable to rule out the possibility of a constant mass-to-light ratio due to their small velocity sample and the unknown orbital properties of the GCs. Working with a sample of 144 GC velocities, and assuming that GCs have isotropic orbits, Zepf *et al.* (2000) argued that the mass-to-light ratio at ~ 30 kpc ($2\text{--}2.5 R_{\text{eff}}$) is at least five times that at a distance of a few kpc, implying the presence of substantial dark matter on large spatial scales.

Irwin & Sarazin (1996) used ROSAT X-ray observations of the hot, gaseous corona around M49 to derive a mass profile for M49 extending to $R \sim 100$ kpc $\simeq 8R_{\text{eff}}$, leading them to conclude that dark matter must be present on spatial scales of $R > R_{\text{eff}}$. Inside $R \sim 10\text{--}15$ kpc ($\sim R_{\text{eff}}$), however, Irwin & Sarazin found mass-to-light ratios that are perfectly compatible with the canonical stellar value in elliptical galaxies. Indeed, Brighenti & Mathews (1997) later decomposed Irwin & Sarazin’s (1996) mass distribution into separate stellar and dark-matter components (as we also do, in §4.3), and argued that any dark-matter halo must contribute negligibly to the total mass inside $R \lesssim 7.5$ kpc $\simeq 0.5R_{\text{eff}}$.

Saglia *et al.* (1993) observed a flattening of the stellar velocity dispersion profile in M49 at a much smaller projected radius, $R \simeq 2\text{--}3$ kpc $\sim 0.2R_{\text{eff}}$, and argued that this alone implied the presence of an dynamically dominant, extended dark-matter halo. However, the large scatter in independent measurements of the stellar kinematics beyond $R \gtrsim 1.5$ kpc (see, *e.g.*, Caon, Macchetto & Pastoriza 2000) rather weakens the conclusion; and it is certainly possible to fit self-consistent galaxy models, containing no dark matter, to the stellar kinematics if no other data are considered (*e.g.*, Kronawitter *et al.* 2000).

Our improved GC velocity dispersion profile from §3 can be used to look at this issue again. We consider the hypothesis that light directly traces mass in M49, so that $M_{\text{tot}}(r)$ in equation (6) comes from integrating the stellar luminosity density profile and multiplying by a constant, stellar mass-to-light ratio. We fit the surface brightness profile of the galaxy taken from Kim *et al.* (2000) — converted from their Washington T_1 photometry to Cousins R -band according to the relation of Geisler (1996) — with the projection of the three-dimensional luminosity density profile,

$$j(r) = \frac{(3 - \gamma)(7 - 2\gamma)}{4} \frac{L_{\text{tot}}}{\pi a^3} \left(\frac{r}{a}\right)^{-\gamma} \left[1 + \left(\frac{r}{a}\right)^{1/2}\right]^{2(\gamma-4)}. \quad (13)$$

This slight modification of the models of Dehnen (1993) allows for a more gradual transition from the inner power-law behavior, $j \sim r^{-\gamma}$, to the asymptotic $j \sim r^{-4}$ at large radii.

The projected best fit of equation (13) to the surface-brightness data of Kim *et al.* (1998) is shown in the left panel of Figure 15. For comparison, we also plot the surface brightness profile measured by Caon, Capaccioli, & D’Onofrio (1994), converted from B -band to Cousins R . The fit has parameters $\gamma = 0.7$, $a = 2.82$ kpc, and $L_{\text{tot}} = 1.40 \times 10^{11} L_{R,\odot}$. It is from this model that we derive a (projected) effective radius of $R_{\text{eff}} = 3'.1 \simeq 13.5$ kpc for M49. Our measurement of the galaxy’s effective radius is intermediate to the values of $R_{\text{eff}} = 3'.8$ found by Caon *et al.* (1994)

and that of Kim *et al.* (2000), who obtained $R_{\text{eff}} = 2'0$ by fitting a de Vaucouleurs law to the same data analyzed here. While the precise value of R_{eff} itself has no bearing on our conclusions, we note that the surface brightness profile of M49 is not well described by a de Vaucouleurs law, which is why Kim *et al.* (2000) restricted their fit to the region $7'' < R < 260''$. As their Figure 8 shows, the fitted model falls well below the measured brightness profile for $R \sim 260''$, leading to likely underestimates of the galaxy’s total luminosity and effective radius.

The right panel of Figure 15 illustrates the three-dimensional stellar mass density profile, $\rho_s(r) = \Upsilon_0 j(r)$, with Υ_0 the R -band mass-to-light ratio. We take its value from McLaughlin & Côté (2003), who show that the stellar kinematics at projected radii $0.1 \leq R \leq 1$ kpc in M49 are best fit by a mass model with no dark matter if $\Upsilon_0 = 5.9 M_\odot L_{R,\odot}^{-1}$ and the velocity ellipsoid of the stellar distribution is slightly radially biased: $\beta_s = 0.3$. We note that this mass-to-light ratio corresponds to a B -band value of $8.1 M_\odot L_{B,\odot}^{-1}$, typical of the cores of elliptical galaxies, and that this constant- M/L mass model is very similar to the self-consistent galaxy model of Kronawitter *et al.* (2000).

We are examining here the hypothesis that light traces mass, and thus the total mass profile to be used in the Jeans equation is just the stellar mass

$$M_s(r) = \Upsilon_0 \int_0^r 4\pi x^2 j(x) dx = \Upsilon_0 L_{\text{tot}} \left[\frac{(r/a)^{1/2}}{1 + (r/a)^{1/2}} \right]^{2(3-\gamma)} \left[\frac{(7 - 2\gamma) + (r/a)^{1/2}}{1 + (r/a)^{1/2}} \right], \quad (14)$$

where, again, Υ_0 is independent of radius in the galaxy and has a value of $5.9 M_\odot L_{R,\odot}^{-1}$ when no additional dark-matter component is invoked. Taking $M_{\text{tot}}(r) = M_s(r)$, then, we solve equation (6) for the intrinsic radial velocity dispersion profile of the stars in M49 by replacing $n_{\text{cl}}(r)$ with $\rho_s(r) \propto j(r)$ from equation (13), and by substituting $\beta_s(r) \equiv +0.3$ (McLaughlin & Côté 2003) for $\beta_{\text{cl}}(r)$. The projection integrals of equations (7) and (8) are then applied — again with $j(r)$ in place of $n_{\text{cl}}(r)$ — to predict the stellar line-of-sight velocity dispersion in the absence of an extended dark-matter halo around M49.

This model is shown as a bold, dotted line in Figure 16, where it is compared with the stellar kinematic data of Davies & Birkinshaw (1988), Saglia *et al.* (1993), and Caon *et al.* (2000). It does a respectable job of reproducing the observed velocity dispersions between $0.1 \lesssim R \lesssim 8$ kpc.⁹ Although the success relies in part on the considerable scatter among the different datasets at $R \gtrsim 1$ kpc, the main point is that the stellar kinematics in M49, by themselves, provide no conclusive evidence for the existence of any extended and massive dark-matter halo.

The bold, solid line in Figure 16 traces the line-of-sight velocity dispersion profile $\sigma_p(R)$

⁹The failure of the model stellar $\sigma_p(R)$ to describe the data at $R \lesssim 0.1$ kpc reflects a poor fit of equation (13) to the observed surface brightness profile at $R \lesssim 2''$ in M49; a likely departure of the stellar anisotropy from the average radial bias $\beta_s(r) = 0.3$; and the influence of the nuclear black hole ($M_\bullet \simeq 5 \times 10^8 M_\odot$; Merritt & Ferrarese 2001) at radii $R \lesssim 30$ pc. No attempt was made to model these effects in detail, as the complexity in the inner 100 pc of the galaxy has no bearing on the larger-scale dynamics of interest to us here.

derived from equations (6)–(8) for the full GC system, when the constant- M/L mass model of equation (14) is adopted, the GC density profile is modeled by the NFW form for $n_{\text{cl}}(r)$ (eq. [9]), and orbital isotropy [$\beta_{\text{cl}}(r) \equiv 0$] is assumed. It fails by a wide margin to describe the observed dispersion profile of the GCs, which is taken from the top panel of Figure 6. The bold, short-dashed line is the expected $\sigma_p(R)$ profile under the same main assumptions but taking the GC density profile to be the Dehnen-model fit of equation (10). The lighter, long-dashed lines revert to the NFW GC density profile but assume strongly radially and tangentially biased GC velocity ellipsoids (upper and lower curves). None of these alternate models fares any better in accounting for the observed GC velocity dispersion at $R \gtrsim 6 \text{ kpc} \sim 0.4\text{--}0.5R_{\text{eff}}$. Evidently, the mass-to-light ratio must increase with galactocentric radius if the high velocity dispersion of the GCs is to be understood.

Regardless of any assumptions on its velocity anisotropy or uncertainties in its spatial distribution, the globular cluster system alone therefore provides incontrovertible evidence, independent of any X-ray data, for the presence of an extended dark-matter halo around M49. It is worth emphasizing that the GC data *alone* are unambiguous on this point for spatial scales $R \lesssim R_{\text{eff}}$.

4.3. Total Mass Profile of M49/Virgo B

Having established the presence of a dark-matter halo around M49, we briefly describe a model for it that is developed and discussed in detail by McLaughlin & Côté (2003). The model is constructed to match the available stellar kinematics and X-ray data in M49/Virgo B. It makes no reference to any aspect of the GC system, and it can thus be used as one of two components contributing to $M_{\text{tot}}(r)$ in the Jeans equation (the other being the luminous component of §4.2) as a constraint on the velocity anisotropy of the GC system.

McLaughlin & Côté (2003) consider a variety of possible analytic descriptions for the dark-matter density profile in M49/Virgo B. Among these, the “universal” halo profile of Navarro *et al.* (1997), $\rho_{\text{dm}} = K (r/r_s)^{-1}(1 + r/r_s)^{-2}$ (cf. eqs. [9] and [11]), is one that provides a good match to all available data. We therefore adopt this form here, to specify

$$M_{\text{dm}}(r) = \int_0^r 4\pi x^2 \rho_{\text{dm}}(x) dx = 4\pi K r_s^3 \left[\ln \left(1 + \frac{r}{r_s} \right) - \frac{r/r_s}{1 + r/r_s} \right]. \quad (15)$$

The mass $M_{\text{tot}}(r)$ interior to any (three-dimensional) radius r is then the sum of $M_{\text{dm}}(r)$ and $M_s(r)$ from equation (14). The unknown parameters in the total mass profile are the dark-matter density normalization K and scale length r_s , and the stellar mass-to-light ratio Υ_0 . McLaughlin & Côté fix these by first constraining the total R -band mass-to-light ratio at a radius $r = 1 \text{ kpc}$: $M_{\text{tot}}(r \leq 1 \text{ kpc})/L(r \leq 1 \text{ kpc}) = 5.9M_{\odot} L_{R,\odot}^{-1}$, thereby guaranteeing that the final model will adequately reproduce the observed stellar kinematics in the core of M49 (cf. §4.2). This leaves only two independent parameters in the mass model, and these are fit by comparing to the X-ray

mass measurements of Irwin & Sarazin (1996) and Schindler *et al.* (1999).¹⁰

The best-fit mass model with an NFW halo is drawn as a bold, solid line in Figure 17. The lighter, dashed line is the mass profile of the dark-matter halo alone, given by equation (15) with $K = 1.12 \times 10^{-3} M_{\odot} \text{ pc}$ and $r_s = 196 \text{ kpc}$. The light, dotted line is the stellar mass distribution of equation (14) with a fitted R -band stellar mass-to-light ratio $\Upsilon_0 = 5.7 M_{\odot} L_{R,\odot}^{-1}$ (and the galaxy parameters γ , a , and L_{tot} already fixed by the fit to the surface brightness profile in Figure 15). Explicitly, then, our final model for M49/Virgo B is:

$$\begin{aligned}
 M_{\text{tot}}(r) &= M_{\text{s}}(r) + M_{\text{dm}}(r) \\
 M_{\text{s}}(r) &= 7.98 \times 10^{11} M_{\odot} \left[\frac{(r/2.82 \text{ kpc})^{1/2}}{1 + (r/2.82 \text{ kpc})^{1/2}} \right]^{4.6} \left[\frac{5.6 + (r/2.82 \text{ kpc})^{1/2}}{1 + (r/2.82 \text{ kpc})^{1/2}} \right] \\
 M_{\text{dm}}(r) &= 1.06 \times 10^{14} M_{\odot} \left[\ln(1 + r/196 \text{ kpc}) - \frac{(r/196 \text{ kpc})}{(1 + r/196 \text{ kpc})} \right].
 \end{aligned} \tag{16}$$

Note that the X-ray masses interior to $r \lesssim 10\text{--}15 \text{ kpc}$ in M49 are fully consistent with the mass of the stellar component alone there — although they clearly do not require the complete absence of any dark matter at the center of the galaxy, this component does not begin to dominate the total mass budget until $r \gtrsim 20 \text{ kpc} \simeq 1.5 R_{\text{eff}}$. Again, it is the GC velocity data that show the clearest evidence on smaller spatial scales for the presence of a massive dark halo.

4.4. Velocity Isotropy in the GC System

Figure 18 plots the stellar and GC velocity dispersion data as Figure 16 did, but now with model curves computed using $M_{\text{tot}}(r)$ given by equation (16) rather than $M_{\text{s}}(r)$ alone. The mass model was constructed by requiring, in part, that it agree with the stellar kinematics, and the bold, dotted curve in Figure 18 verifies that this is the case. It is worth noting that our model — which now includes the dark-matter halo that the GC data show must be present — favors the stellar data of Davies & Birkinshaw (1988) and Saglia *et al.* (1993) over those of Caon *et al.* (2000) (the small, open squares that scatter well below the dotted curve in the Figure). The bold, solid line in this plot is the velocity dispersion profile predicted for the full GC system if its three-dimensional density profile $n_{\text{cl}}(r)$ in equations (6)–(8) is given by the NFW functional fit of equation (9), and if velocity isotropy, $\beta_{\text{cl}}(r) \equiv 0$, is assumed. The excellent agreement between this model curve and the GC data over the full range $6 \lesssim R \lesssim 30 \text{ kpc}$ implies that *the assumption of isotropy is, in fact, essentially correct.*

¹⁰The total mass in X-ray gas within a sphere of radius $r = 100 \text{ kpc}$ centered on M49 is only $\sim 1/15$ the mass in stars and $\sim 1/200$ that in dark matter, so the gas mass itself is negligible. As it turns out, though, the X-ray gas traces the dark-matter distribution throughout M49/Virgo B (McLaughlin & Côté 2003), so its contribution to the overall mass budget is actually included in the normalization of $M_{\text{dm}}(r)$.

The bold, dashed line in Figure 18 is the model $\sigma_p(R)$ for the GC system if its density profile is taken from the alternate, Dehnen-model fit of equation (10). Isotropy is still assumed. This model also compares favorably with the data, falling within the 68% confidence interval around the σ_p estimate at almost every point. We note again that we prefer on other grounds the shallower extrapolation of the NFW density profile for the GC system, over the steeper fall-off of the Dehnen profile (see §4.1). However, the present comparison of the models shows that our inference of velocity isotropy in the M49 GC system does not rely on this particular choice.

Figure 19 gives a close-up view of the comparison between the velocity dispersion data and a number of models for the full GC system. The top panel shows the same data as Figures 18, 16, and 6, along with the usual 68% and 95% confidence bands. The bottom panel shows the projected *aperture* dispersion profile, *i.e.*, the velocity dispersion of all objects interior to a given projected radius R , rather than just those in a narrower annulus. For a model, this cumulative spatial average of $\sigma_p(R)$ is defined by

$$\sigma_{\text{ap}}^2(\leq R) = \left[\int_{R_{\text{min}}}^R N_{\text{cl}}(R') \sigma_p^2(R') R' dR' \right] \left[\int_{R_{\text{min}}}^R N_{\text{cl}}(R') R' dR' \right]^{-1}, \quad (17)$$

with R_{min} the projected galactocentric radius of the innermost datapoint in a velocity sample ($R_{\text{min}} = 1.9$ kpc for us). Although the interpretation of the coarsely averaged σ_{ap} profile can be subtler than that of the differential profile $\sigma_p(R)$, it has the significant advantage of reduced noise at large R .

The bold, solid line in the top panel of Figure 19 is the same as that in Figure 18: the predicted $\sigma_p(R)$ profile for the full GC system in the mass distribution of equation (16), if $n_{\text{cl}}(r)$ is given by the NFW profile of equation (9) and $\beta_{\text{cl}}(r) \equiv 0$. The same curve in the bottom panel is just the result of averaging this model profile with equation (17). The bold, short-dashed curves in the two panels of the Figure are analogous to the solid lines but assume the Dehnen-model density profile of equation (10) for the full GC system. The lighter, long-dashed curves assume the NFW profile for $n_{\text{cl}}(r)$ and show predictions for velocity anisotropies ranging from extreme radial bias to extreme tangential bias: from top to bottom, $\beta_{\text{cl}} = 1 - \sigma_\theta^2/\sigma_r^2 = 0.99, 0.5, -1$, and -99 . These anisotropies are included in the models as spatially constant, so that the curves corresponding to them should be viewed as representative of more realistic, spatially varying functions $\beta_{\text{cl}}(r)$ which average out to the constants that we have specified.

The close adherence of the isotropic models to the GC data is striking, particularly in the case of the aperture dispersion profile. The spatial averaging involved there effectively blurs local, apparently noise-driven features in the differential $\sigma_p(R)$ data (*e.g.*, the bump around $R \sim 22$ kpc), such that the σ_{ap} data never stray substantially from the predictions of isotropy for either assumed density profile $n_{\text{cl}}(r)$. The possibility of even modestly radial or tangential average anisotropy (*i.e.*, $\beta_{\text{cl}} = 0.5$ or -1) can be ruled out at the 95% confidence level or better in the full GC system.

Aside from its intrinsic importance for models of GC formation and evolution, the finding of

such a high degree of consistency with velocity isotropy in the full GC system could be of practical use for measurements of the gravitating mass profiles in other early-type galaxies, where data may not be available in the variety and quality required for the type of modeling that we described in §4.3. M49 is now the second galaxy (the other being M87) in which we have been able to show by direct means that an isotropic velocity ellipsoid is a highly accurate description of the GC kinematics. The *assumption* of isotropy in other GC systems may therefore be much better justified than before, making it possible to use the Jeans equation (6) with $\beta_{\text{cl}}(r) \equiv 0$ — provided that $n_{\text{cl}}(r)$ is also well known — to derive $M_{\text{tot}}(r)$ from a set of velocity-dispersion measurements.

Finally, we construct dynamical models for the metal-poor and metal-rich GC subsystems separately. This is a somewhat riskier proposition, given the noisier dispersion profiles of these smaller datasets and the much poorer characterization of the density profiles $n_{\text{cl}}^{\text{MP}}(r)$ and $n_{\text{cl}}^{\text{MR}}(r)$ (Figure 14 in §4.1). With these caveats in mind, we compare the observed and predicted velocity dispersion profiles for the metal-poor and metal-rich GCs in Figures 20 and 21. The various curves in these figures have meanings analogous to those in Figure 19. The bold, solid curves assume orbital isotropy and adopt the NFW fits for the density profiles of the subsystems (eq. [11]), while the bold, short-dashed curves assume isotropy and the Dehnen-model density profiles of equation (12). The light, long-dashed curves assume NFW density profiles and spatially constant anisotropies $\beta_{\text{cl}} = 0.99, 0.5, -1, \text{ and } -99$.

The isotropic NFW density-model curve in Figure 20 provides quite an acceptable description of the observed $\sigma_p(R)$ of the metal-poor globulars until radii $R \gtrsim 20\text{--}25$ kpc, where the subsequent rise in the data might suggest a move to a slight radial bias in the GC orbits. However, the model remains within the 68% confidence bands on the measurements nearly until $R \sim 30$ kpc, the limit of reliability. The observed σ_{ap} data in the bottom panel adhere more closely to the isotropic curve at still larger radii. The model assuming a Dehnen-type density profile for the metal-poor GC system gives a stronger suggestion of radial velocity anisotropy,¹¹ although the isotropic case is still barely consistent (within the 95% confidence bands) with the observed profile. Because of the increased noise in the measured dispersions and, more importantly, the poorly constrained density profile, it is difficult to draw any firm conclusions on the orbital properties of the metal-poor GCs, beyond the obvious: (1) the hypothesis of isotropy is not far wrong, particularly at small galactocentric distances $R \lesssim 20$ kpc $\simeq 1.5R_{\text{eff}}$; and (2) any possible radial bias present at larger projected radii is likely to be modest.

An assessment of the orbital properties of the metal-rich GCs is necessarily more difficult. Not only is the extrapolation of their observed density profile very uncertain, but the difficulties posed by the 10 rapidly rotating objects concentrated around $R \simeq 23.2$ kpc, as discussed in §3.2, leave little in the way of data that can be compared reliably with any model. The top panel shows our smoothed velocity-dispersion profile from Figure 6, with those parts relying on any GC velocities

¹¹Given a fixed, observed velocity dispersion for a tracer population in a fixed gravitational potential, a steeper density profile always implies a more radial anisotropy through the Jeans equation.

from within $302'' \leq R \leq 337''$ excised. The most that can be said is that, at $R \sim R_{\text{eff}} = 13.5$ kpc, the data are once again consistent with velocity isotropy, regardless of which GC density profile $n_{\text{cl}}^{\text{MR}}(r)$ is assumed. Beyond this, however, the steep drop in $\sigma_p(R)$ appears unsupportable in *any* dynamical model that we have constructed. It is true that the outer-radius data point suggests some return to understandable behavior in the metal-rich GC system (*i.e.*, $1\text{-}\sigma$ consistency with isotropy for either $n_{\text{cl}}^{\text{MR}}(r)$ profile), but the trend of the cumulative $\sigma_{\text{ap}}(\leq R)$ profile (towards model curves suggesting a strong tangential bias in the orbital distribution) also suggests that the low velocity dispersion may be problematic.

If the full GC system is perfectly isotropic, and the metal-poor component is fairly closely so, then it stands to reason that the metal-rich GC system should be close to isotropic as well. Thus, its behavior beyond $\sim 1R_{\text{eff}}$ needs to be much better understood empirically before any dynamical sense can be made of it. We noted in §3 (see, *e.g.*, Figure 5) that the low velocity dispersion of the metal-rich GCs is the manifestation of an absence of red objects with $\langle v_p \rangle \gtrsim 1500$ km s⁻¹ from our velocity survey, and a corresponding lack of metal-rich GCs with $\langle v_p \rangle \lesssim 700$ km s⁻¹ outside about one effective radius in the galaxy. It would be useful to know whether these are artifacts of our particular sample or indicative of something more profound. For instance, a velocity dispersion $\sigma_p \lesssim 250$ km s⁻¹ at galactocentric radii $R > R_{\text{eff}}$ is even lower than we would expect for the *stellar light* of M49 (cf. Figure 18). Very closely related to this issue is the density profile of the metal-rich GC system, which will have to be defined reliably out to much larger radii than we have been able to do with existing databases. Even the Dehnen-model density profile that we explored here, with its behavior $n_{\text{cl}} \rightarrow r^{-4}$ at large r , predicts GC kinematics that seem considerably too “hot” compared with the metal-rich data. Either current radial velocity surveys have missed a number of high-velocity, metal-rich GCs at large galactocentric radii — perhaps due to some observational bias or simple bad luck — or the density of metal-rich GCs system falls very rapidly indeed to zero beyond several tens of kpc. Deep, wide-field imaging in a metallicity-sensitive filter combination can directly address the latter possibility, and it will be essential to developing any deeper understanding of GC dynamics in M49.

5. Comparing M49, M87, M31 and the Milky Way

A direct comparison between the kinematic and dynamic properties of GCs in M49 and M87 seems in order, given the similarity in the respective datasets and the methods of analysis. In fact, the GC radial velocities now amassed for these galaxies constitute the two largest radial velocity samples yet assembled for pure Population II tracers in early-type galaxies.

It is worth bearing in mind that that the GC systems of these two galaxies are similar in many respects. For instance, both have bimodal metallicity distributions, with peaks at $[\text{Fe}/\text{H}] \sim -1.5$ and -0.3 dex. The ratio of the number of metal poor to metal rich GCs is very nearly the same in both galaxies. The GC formation efficiencies for the composite GC systems and the two subsystems are quite similar in both cases (*e.g.*, McLaughlin 1999a; Côté 2003). Likewise, the

measured ages of the metal-poor and metal-rich GCs suggest that they are — on the whole — old and *roughly* coeval (Cohen *et al.* 1998; Puzia *et al.* 1999; Beasley *et al.* 2000; Jordán *et al.* 2002; cf. Kundu *et al.* 1999 and Lee & Kim 2000).

To some extent, this similarity extends to the dynamical properties of the two GC systems. Most notably, in both M49 and in M87, the full GC system has an almost perfectly isotropic velocity dispersion tensor (*e.g.*, compare Figure 19 above with Figure 13 of Côté *et al.* 2001). There are, nevertheless, some clear differences in the overall GC kinematics between the two galaxies. For instance, the metal-poor and metal-rich subsystems in M87 share an essentially identical projected velocity dispersion, while in M49, the metal-rich GC sample appears to be significantly colder than the metal-poor component.

Table 4 summarizes the global kinematic properties of the two GC systems. Note that the results for M87 differ slightly from those presented in Côté *et al.* (2001) since we have re-computed the various kinematic properties after fixing the systemic velocity of each GC subsample at the velocity of M87 ($v_{\text{gal}} = 1277 \pm 2 \text{ km s}^{-1}$; van der Marel 1994), identical to the approach taken in §3 for M49. In addition, we have re-calculated the global quantities for the full GC system and the metal-rich component in M49, after removing the 10 rapidly rotating, metal-rich GCs at $22 \lesssim R \lesssim 24.5 \text{ kpc}$.

As Table 4 shows, it is in their rotation properties that obvious differences between the two systems appear. In M87, both the metal-poor and metal-rich GC subsystems show relatively rapid rotation, with $\Omega R/\sigma_{p,r} \sim 0.45$. In M49, however, rotation is somewhat more modest among the metal-poor GCs ($\Omega R/\sigma_{p,r} = 0.27$), and it is very weak indeed in the metal-rich GC system ($\Omega R/\sigma_{p,r}$ of order 0.1 and consistent with 0). The orientation of the rotation axes in the two systems is also noteworthy. In M87, the metal-rich GCs are found to rotate, at all radii, about the galaxy’s minor axis. This is also true of the metal-poor GCs beyond $R \sim 2R_{\text{eff}}$ in that galaxy, but *inside* this radius, the metal-poor GCs in M87 show *major-axis* rotation (see Table 4, and Côté *et al.* 2001). In M49, the metal-poor GCs are consistent with minor-axis rotation inside $R \lesssim 2R_{\text{eff}}$ and suggest a possible transition to major-axis rotation *outside* that radius. Interestingly, the position angles for the rotation axes of the stellar light in M87 and M49 are found to be $\Theta_0 = -23 \pm 10^\circ$ and $59 \pm 3^\circ$, respectively (Davies & Birkinshaw 1988). Thus, to within the measurement errors, and over the range where the GC and stellar data overlap, the metal-poor GCs in both cases seem to trace the rotation of the underlying galaxy. It would be interesting to extend the stellar kinematic measurements to larger radii, to see if this trend continues, *i.e.*, if the stellar rotation axis also “flips” by 90° in M87 especially.¹² Finally, at the radii in M87 where the metal-poor and metal-rich GCs both rotate about the minor axis, they do so in the same direction. By contrast, there is some evidence that the metal-rich GC system of M49 may rotate

¹²At present, the best stellar kinematic data for M87 (Sembach & Tonry 1996) extend only to about $1.5R_{\text{eff}}$. At $2R_{\text{eff}}$, the surface brightness of the galaxy is $\mu_V \sim 23.6 \text{ mag arcsec}^{-2}$, well within the range of modern long-slit spectrographs on large telescopes.

counter to the metal-poor one. We caution that this result is of low statistical significance, as we have a sample of only ~ 100 red GCs spread over an order-of-magnitude range in galactocentric position, but it clearly merits further attention.

These differences between the GC systems of M49 and M87 become all the more puzzling when one considers the results for the GC systems of late-type galaxies. To date, in only two spiral galaxies have samples of a hundred or more GC velocities been accumulated: the Milky Way and M31. In the former case, $\Omega R/\sigma = 0.56 \pm 0.15$ for the GC system as a whole, and $\Omega R/\sigma = 0.32 \pm 0.20$ and 1.05 ± 0.28 for the metal-poor and metal-rich subsystems (Côté 1999). In M31, the global value for all GCs is $\Omega R/\sigma = 0.88 \pm 0.09$, with the metal-poor and metal-rich subsystems having $\Omega R/\sigma = 0.85 \pm 0.09$ and 1.10 ± 0.16 (Perrett *et al.* 2002). Based on this very small sample, it seems that rotation may be more important for the GC systems of disk galaxies than for those of ellipticals. Clearly, however, the four GC systems show considerable diversity in their rotational properties. It seems that the lone common feature among the GC systems of these four galaxies is the tendency for the metal-poor GCs to form a rotating population, albeit with widely varying levels of dynamical importance (*i.e.*, the percentage of total kinetic energy stored in rotation varies by more than an order of magnitude, from $\sim 3\%$ in M49 to $\sim 40\%$ for M31). Furthermore, the metal-rich GCs of M87, M31, and the Milky Way *also* form rotating populations with $\Omega R/\sigma$ ratios that are equal to or greater than those of their metal-poor counterparts. In this regard, the metal-rich GC subsystem in M49 may be something of an anomaly — although such a conclusion may be premature given the current data.

The kinematic properties of the GC systems studied to date undoubtedly contain important clues to the formation histories of their parent galaxies, although the full implications at this point remain unclear. Nevertheless, it seems that the traditional picture of GC systems as non-rotating, or slowly rotating, entities — a view that can be traced to the slow rotation exhibited by halo GCs outside of the central few kpc in the Milky Way — may be in need of revision. The net GC rotation detected in an ever-increasing number of galaxies, which we speculate may be a common property of GC systems, probably reflects the outcome of a complex interplay between any number of processes that could have shaped the observed GC velocity fields: tidal torques from neighboring galaxies, spin-up during gravitational collapse, angular momentum transfer and energy dissipation during gaseous mergers, and the conversion of orbital angular momentum to rotation during gas-poor mergers and accretions. The extraction of quantitative predictions for GC dynamics from models of these processes will be a challenging task — as will be the complete and accurate empirical characterization of kinematics to test those predictions.

6. Summary

We have reported radial velocities for 196 GCs associated with M49, the brightest member of the Virgo cluster. Combining these velocities with previously published measurements brings the total number of GCs with measured radial velocities to 263. This sample is comparable to

that assembled recently for M87 (Hanes *et al.* 2001) in terms of size, spatial coverage, velocity precision, and the availability of metallicities from Washington photometry. Using these data, we have carried out a kinematical and dynamical analysis of the M49 GC system which mirrors that presented recently for M87 by Côté *et al.* (2001).

We confirm previous findings that, when considered in its entirety, the GC system of M49 shows a modest net rotation that is due almost entirely to the rotation of the metal-poor subsystem. Likewise, we verify that, in a global average, the metal-rich subsystem shows essentially no rotation. However, when examined in greater detail, there is some weak evidence that the metal-rich GCs in this galaxy may, in fact, be slowly rotating, but in the opposite direction to the metal-poor GCs. The overall negligible global rotation of the metal-rich component is traced to a small sample of 10 clusters which appear to show very rapid minor-axis rotation, in the same direction as the metal-poor GCs. These objects merit further attention, as they may be the relic of a past merger or accretion event. Given the rather limited sample of metal-rich GCs with measured velocities, the significance of these findings must await additional radial velocity measurements, but it is abundantly clear that conclusions formed on the basis of globally averaged kinematics are likely to miss potentially interesting and complex variations within a given GC system.

A comparison with the results for M87, M31 and the Milky Way suggests that rotation may, in fact, be generic to GC systems, a turnabout from the traditional view of GC populations as slowly rotating systems. Any trends in GC rotational properties with metallicity seem to be quite complex, and will likely require GC radial velocity data for an expanded sample of galaxies before they can be better characterized and understood. We note, however, that in M49 and M87, there is a hint that the orientation of the rotation axes for the metal-poor GCs trace those of the underlying galaxy.

Previous studies of M49, its GC system, and its X-ray halo have produced some conflicting claims on the need for dark matter. We have shown that the GC radial velocities and density profiles alone now provide unmistakable evidence for a massive dark halo in M49/Virgo B. This result, which is corroborated by analyses of its X-ray halo but is independent of the X-ray observations, holds for any choice of GC orbital properties.

We have presented a mass model for M49/Virgo B that satisfies all existing observational constraints on the mass distribution from optical and X-ray surface brightness profiles and stellar kinematical data. A Jeans-equation analysis of the GC radial velocities and density profiles using this mass model reveals the GC system as a whole to be perfectly well described by an isotropic velocity dispersion tensor. This is also likely to be true of the separate metal-poor and metal-rich subsystems, but definite conclusions must await the measurement of additional radial velocities and improved surface density profiles for the subpopulations. Indeed, the poorly constrained density distributions of metal-poor and metal-rich GCs on large scales may now be the principal obstacle limiting our understanding their orbital properties. In any case, the demonstration that

the composite GC system of M49, like that of M87, has an almost perfectly isotropic velocity dispersion tensor lends support to the general assumption of isotropy when using the GC systems of early-type galaxies to derive gravitational masses.

PC and JPB acknowledge support provided by the Sherman M. Fairchild Foundation during the early stages of this work. PC also acknowledges support provided by NASA LTSA grant NAG5-11714. This research has made use of the NASA/IPAC Extragalactic Database (NED) which is operated by the Jet Propulsion Laboratory, California Institute of Technology, under contract with the National Aeronautics and Space Administration. The entire Keck/LRIS user communities owes a debt of gratitude to Jerry Nelson, Gerry Smith, Bev Oke, and the many other people who worked to make the Keck telescopes a reality. We are grateful to the W. M. Keck Foundation for the vision to fund the construction of the W. M. Keck Observatory. The authors wish to extend special thanks to those of Hawaiian ancestry on whose sacred mountain we are privileged to be guests. Without their generous hospitality, none of the observations presented herein would have been possible.

Table 1. Observing Log

Run	Date (d/m/y)	Grating	λ_c (\AA)	$\lambda/\Delta\lambda$
1	16-17/04/1998	600/5000	5200	870
2	24/03/1999	600/7500	8550	1425
3	6/04/1999	600/7500	8550	1425
4	30/04/2000	600/5000	4860	870

Table 2. Radial Velocities for Confirmed and Candidate M49 Globular Clusters

ID	α (J2000)	δ (J2000)	R (arcsec)	Θ (deg)	T_1 (mag)	$(C - T_1)$ (mag)	[Fe/H] (dex)	$v_{p,i}$ (km s ⁻¹)	Source ¹	$\langle v_p \rangle$ (km s ⁻¹)
<u>Globular Clusters</u>										
85	12:29:37.87	7:52:53.9	459.6	198.2	20.52	1.30	-1.43±0.05	826±152 826± 68	1 3	826± 62
117	12:29:33.24	7:53:02.6	477.7	206.4	21.78	1.99	0.17±0.14	851± 66	2	851± 66
150	12:29:58.39	7:53:12.8	447.7	158.9	21.75	1.21	-1.56±0.12	849±122	1	849±122
170	12:29:37.75	7:53:18.0	437.4	199.5	21.19	1.73	-0.44±0.07	1243± 69	Z	1243± 69
179	12:29:26.74	7:53:21.0	513.0	217.1	20.91	1.35	-1.31±0.11	580± 83	2	580± 83
258	12:29:57.99	7:53:44.1	416.4	158.1	22.01	2.12	0.48±0.16	1281±155	1	1281±155
282	12:30:05.42	7:53:49.8	464.3	145.1	20.38	1.65	-0.61±0.13	751± 39	Z	751± 39
288	12:29:22.03	7:53:51.0	536.3	225.0	21.03	1.72	-0.46±0.15	286± 47	2	286± 47
305	12:29:55.59	7:53:54.2	394.8	162.4	20.52	1.96	0.11±0.06	874± 58	3	874± 58
337	12:29:57.61	7:54:00.5	399.1	158.0	20.69	1.39	-1.24±0.08	449±136	1	449±136
342	12:29:27.65	7:54:00.9	473.2	218.7	21.53	1.61	-0.70±0.09	825± 50	2	825± 50
430	12:29:35.07	7:54:14.6	401.2	207.5	20.92	1.29	-1.46±0.04	1167±164	1	1167±164
455	12:29:30.49	7:54:19.4	432.9	215.8	20.71	1.31	-1.42±0.05	294± 77	2	294± 77
460	12:29:57.78	7:54:20.1	382.0	156.6	21.78	1.50	-0.98±0.11	1800±134	1	1800±134
463	12:29:50.42	7:54:21.0	352.1	173.0	19.93	1.59	-0.77±0.05	342± 27	Z	342± 27
522	12:29:53.54	7:54:31.1	350.9	165.3	21.02	1.67	-0.56±0.08	805±129	3	805±129
564	12:29:56.82	7:54:37.9	360.0	157.5	21.06	1.57	-0.81±0.07	1088± 83	1	1088± 83
637	12:29:42.59	7:54:49.5	329.3	192.9	19.95	1.54	-0.88±0.07	814± 31	Z	814± 31
647	12:29:37.12	7:54:50.8	355.2	205.9	21.15	1.34	-1.34±0.07	1101± 39	Z	1101± 39
676	12:29:52.36	7:54:56.0	322.6	167.2	20.72	1.46	-1.07±0.07	1162±167 1304± 56	3 Z	1289± 53
677	12:29:52.89	7:54:56.0	324.3	165.9	22.03	1.82	-0.23±0.14	1090±154	1	1090±154
714	12:30:07.42	7:55:01.1	427.7	136.4	20.32	1.55	-0.85±0.09	1061± 39	Z	1061± 39
744	12:29:53.46	7:55:05.8	317.2	163.9	19.73	1.38	-1.26±0.06	814± 29	Z	814± 29
830	12:29:58.72	7:55:17.9	336.5	150.4	21.24	2.22	0.72±0.10	1313±105	1	1313±105
876	12:30:00.68	7:55:23.9	346.8	145.8	19.63	1.46	-1.06±0.13	1487± 24	Z	1487± 24
888	12:29:53.50	7:55:25.0	298.9	162.8	20.58	1.42	-1.17±0.07	1088±172	3	1088±172
929	12:29:55.43	7:55:29.4	304.6	157.4	21.36	1.93	0.04±0.11	1268±143	1	1268±143
952	12:29:38.07	7:55:31.4	312.6	206.8	21.16	1.52	-0.93±0.08	970±127	1	970±127
995	12:29:18.62	7:55:35.2	510.2	237.4	20.90	1.54	-0.87±0.08	828± 90	Z	828± 90
1047	12:29:33.50	7:55:39.2	342.2	217.6	21.14	1.89	-0.05±0.08	1083± 30 1147± 77	Z 2	1091± 28
1087	12:29:49.75	7:55:43.0	269.5	173.0	19.64	1.44	-1.12±0.06	1070± 29	Z	1070± 29
1095	12:29:39.43	7:55:43.6	292.8	204.3	22.00	1.22	-1.62±0.08	1772±127	1	1772±127
1110	12:29:44.59	7:55:45.8	268.3	189.4	19.88	1.37	-1.28±0.10	1626± 24	Z	1626± 24
1174	12:29:55.89	7:55:51.3	287.4	154.5	21.80	2.05	0.33±0.13	954±185	3	954±185
1193	12:29:57.99	7:55:53.7	300.1	148.9	21.00	1.88	-0.08±0.09	761± 81	1	761± 81
1207	12:29:58.63	7:55:54.9	304.1	147.2	21.34	1.25	-1.57±0.07	739± 69	Z	739± 69
1234	12:29:19.39	7:55:57.4	488.8	238.9	20.81	1.47	-1.03±0.07	1059± 64 1082± 44	Z 2	1075± 36
1255	12:29:52.92	7:55:59.9	263.0	162.4	19.71	1.35	-1.33±0.05	816± 66	Z	816± 66
1300	12:29:54.90	7:56:04.4	269.3	156.1	21.95	2.02	0.26±0.16	761±128	3	761±128
1315	12:29:43.94	7:56:06.4	249.9	192.4	20.68	1.42	-1.15±0.09	1370± 76 1735±103	Z 1	1497± 61
1369	12:29:59.20	7:56:11.7	295.0	144.1	21.21	1.40	-1.22±0.08	1235±117	1	1235±117
1411	12:30:11.66	7:56:15.8	428.3	123.3	21.61	1.30	-1.43±0.11	753± 65	3	753± 65
1423	12:29:35.31	7:56:16.7	296.1	217.9	20.94	1.57	-0.80±0.08	1768± 89	1	1653± 27

Table 2—Continued

ID	α (J2000)	δ (J2000)	R (arcsec)	Θ (deg)	T_1 (mag)	$(C - T_1)$ (mag)	[Fe/H] (dex)	$v_{p,i}$ (km s ⁻¹)	Source ¹	$\langle v_p \rangle$ (km s ⁻¹)
1448	12:29:29.46	7:56:19.5	354.2	229.3	20.79	1.34	-1.34±0.05	1641± 29	Z	
1475	12:29:40.45	7:56:22.5	251.1	204.8	21.15	1.46	-1.07±0.09	1353± 26	Z	1353± 26
								970± 50	4	1001± 29
								1018± 37	Z	
1508	12:30:02.66	7:56:25.6	317.9	135.1	21.49	1.99	0.18±0.11	1316± 50	3	1371± 35
								1425± 50	4	
1518	12:29:40.44	7:56:25.9	248.1	205.2	19.25	1.85	-0.15±0.10	1050± 36	S	1050± 36
1570	12:29:39.07	7:56:31.0	252.9	209.8	20.98	1.58	-0.78±0.08	1034± 61	Z	1034± 61
1587	12:29:59.34	7:56:32.9	279.4	141.2	21.16	1.12	-1.86±0.11	471± 75	Z	471± 75
1650	12:29:55.84	7:56:39.1	244.7	149.8	20.85	1.95	0.09±0.09	973± 25	4	985± 21
								988± 57	3	
								1040± 55	Z	
1712	12:29:40.09	7:56:44.3	234.0	208.3	20.36	1.34	-1.35±0.10	1144± 40	S	1144± 40
1731	12:30:01.35	7:56:46.7	289.2	134.8	20.71	1.82	-0.22±0.09	1241± 25	4	1250± 19
								1246± 40	3	
								1294± 51	Z	
1749	12:29:47.41	7:56:48.1	202.4	180.6	20.92	1.98	0.17±0.10	1407± 88	Z	1407± 88
1764	12:29:44.70	7:56:49.1	205.8	191.9	20.82	1.72	-0.46±0.11	855± 37	Z	855± 37
1782	12:29:37.28	7:56:50.4	251.4	217.3	21.91	1.99	0.18±0.12	967±142	1	986± 97
								1002±135	1	
1798	12:29:45.21	7:56:51.5	202.0	189.9	20.69	1.98	0.16±0.09	785± 25	4	795± 19
								811± 31	Z	
1831	12:29:51.92	7:56:53.5	207.4	161.7	21.86	1.34	-1.35±0.09	1129±148	3	1129±148
1846	12:29:46.42	7:56:54.8	196.4	184.9	21.07	2.02	0.26±0.11	1041± 25	4	1041± 25
1889	12:29:54.02	7:56:58.7	214.6	153.4	20.98	1.25	-1.55±0.06	1105±164	1	1187± 24
								1189± 25	4	
1892	12:30:04.11	7:56:58.8	312.1	127.9	21.09	1.53	-0.91±0.11	1029± 77	3	1077± 42
								1098± 50	4	
1905	12:29:41.13	7:57:00.1	212.9	206.6	21.22	1.36	-1.29±0.11	1483±112	1	1472± 24
								1472± 25	4	
2013	12:29:38.38	7:57:10.2	225.8	217.1	21.28	1.40	-1.21±0.11	517± 25	4	517± 25
2031	12:29:47.67	7:57:11.8	178.7	179.4	20.71	1.37	-1.28±0.08	1438± 65	M	1380± 22
								1366± 25	4	
								1426± 71	3	
2045	12:29:39.05	7:57:13.1	217.6	215.4	20.94	1.77	-0.35±0.09	857± 54	S	950± 22
								970± 25	4	
2060	12:29:39.71	7:57:13.9	211.4	213.4	20.62	1.29	-1.45±0.06	1217± 65	M	1293± 22
								1342±124	1	
								1303± 25	4	
2070	12:29:25.32	7:57:14.6	374.0	242.0	22.14	2.16	0.58±0.15	1193± 79	2	1193± 79
2140	12:29:54.18	7:57:20.9	196.2	149.9	20.45	1.80	-0.28±0.10	730± 53	S	770± 26
								784± 31	Z	
2163	12:29:55.88	7:57:23.2	208.2	143.5	20.15	2.01	0.22±0.05	402± 43	S	402± 43
2178	12:29:37.39	7:57:24.6	224.1	222.3	21.51	1.19	-1.69±0.10	522±136	1	773± 24
								782± 25	4	
2188	12:29:58.57	7:57:25.8	232.3	135.2	21.15	1.33	-1.36±0.11	623±102	1	704± 24
								709± 25	4	
2195	12:29:30.72	7:57:26.1	299.1	236.7	21.33	1.14	-1.80±0.12	1241± 56	Z	1241± 56
2303	12:30:00.66	7:57:34.7	249.5	128.7	21.91	1.33	-1.37±0.12	864± 73	3	864± 73
2306	12:29:57.69	7:57:34.9	216.7	135.9	20.35	1.63	-0.68±0.10	893± 25	4	893± 25
2341	12:29:32.76	7:57:38.3	267.1	235.3	20.76	1.91	-0.01±0.11	1001± 68	S	1073± 55

Table 2—Continued

ID	α (J2000)	δ (J2000)	R (arcsec)	Θ (deg)	T_1 (mag)	$(C - T_1)$ (mag)	[Fe/H] (dex)	$v_{p,i}$ (km s ⁻¹)	Source ¹	$\langle v_p \rangle$ (km s ⁻¹)
2406	12:29:45.80	7:57:44.1	148.6	190.1	20.85	2.03	0.27±0.11	1216± 95	1	1141± 23
								1128± 25	4	
								1244± 70	S	
2420	12:29:41.00	7:57:44.7	175.2	213.7	20.95	2.08	0.40±0.10	763± 92	Z	763± 92
2421	12:29:52.18	7:57:45.0	161.0	154.7	21.09	1.43	-1.13±0.08	1726± 25	4	1729± 24
								1801±117	3	
2452	12:29:57.82	7:57:48.1	208.8	133.0	21.49	1.40	-1.20±0.13	1828± 81	Z	1828± 81
2482	12:29:42.71	7:57:50.0	157.7	207.1	21.58	2.08	0.39±0.13	767± 56	S	767± 56
2502	12:30:00.67	7:57:52.1	239.1	125.4	21.08	1.48	0.01±0.08	930± 25	4	935± 22
								955± 49	3	
2528	12:29:49.33	7:57:53.7	139.4	169.0	20.34	1.46	-1.06±0.08	807± 65	M	795± 23
								794± 25	4	
2543	12:29:52.87	7:57:54.8	157.1	149.8	20.27	1.36	-1.30±0.10	1199± 48	S	1221± 22
								1228± 25	4	
2545	12:29:57.70	7:57:55.1	202.7	131.9	20.64	1.31	-1.41±0.08	414± 53	1	414± 53
2569	12:29:43.87	7:57:57.2	144.1	202.3	20.12	1.89	-0.06±0.12	1056± 46	S	1068± 22
								1072± 25	4	
2622	12:29:52.65	7:58:02.2	149.1	149.4	21.09	1.65	-0.61±0.10	467±164	3	467±164
2634	12:29:39.63	7:58:03.3	173.1	222.8	19.70	1.56	-0.82±0.12	1014± 57	S	1014± 57
2753	12:29:46.19	7:58:12.5	119.7	189.6	20.88	1.19	-1.70±0.09	945±100	Z	945±100
2759	12:29:26.29	7:58:12.6	337.0	249.6	19.97	1.31	-1.42±0.04	654± 92	Z	654± 92
2813	12:29:48.56	7:58:16.0	115.5	172.5	21.00	1.94	0.07±0.11	363± 25	4	363± 25
2817	12:30:03.46	7:58:16.2	262.7	115.8	21.05	1.50	-0.98±0.10	665± 47	Z	665± 47
2938	12:29:27.92	7:58:23.4	310.5	249.9	20.98	1.59	-0.75±0.06	843± 87	2	843± 87
2960	12:29:59.98	7:58:25.0	212.8	119.7	21.63	1.43	-1.13±0.11	637±125	1	637±125
3150	12:29:38.50	7:58:37.5	163.3	235.3	21.40	1.79	-0.29±0.12	952± 42	S	1126± 21
								1188± 25	4	
3208	12:29:53.55	7:58:41.4	126.1	135.0	21.17	1.43	-1.14±0.10	677± 96	1	703± 75
								745±122	3	
3250	12:29:27.74	7:58:44.2	306.6	253.7	21.20	1.23	-1.61±0.09	1117± 56	2	1117± 56
3289	12:29:37.79	7:58:46.2	167.6	239.8	21.48	1.90	-0.04±0.10	1476±101	1	1476±101
3307	12:30:02.45	7:58:46.9	236.8	110.7	20.25	1.53	-0.89±0.13	1834± 65	M	1834± 65
3355	12:29:34.40	7:58:51.5	210.6	248.0	20.84	1.37	-1.28±0.10	1436± 72	1	1436± 72
3361	12:29:34.46	7:58:52.0	209.5	248.0	20.34	1.55	-0.85±0.10	1392± 33	Z	1392± 33
3372	12:29:52.46	7:58:52.7	106.8	136.8	21.59	1.60	-0.74±0.10	1331±183	3	1331±183
3422	12:29:37.93	7:58:56.3	160.9	242.6	20.87	1.76	-0.36±0.12	1265± 81	1	1265± 81
3434	12:29:22.62	7:58:56.8	377.4	258.8	22.10	1.19	-1.70±0.10	255± 75	2	255± 75
3545	12:29:52.22	7:59:03.5	96.6	134.0	20.84	1.83	-0.19±0.12	1046±101	3	1046±101
3584	12:29:35.50	7:59:06.6	189.9	250.4	21.70	1.98	0.16±0.11	952±158	1	952±158
3603	12:29:46.71	7:59:07.9	63.8	191.1	20.47	1.75	-0.39±0.09	1026± 25	4	1026± 25
3628	12:29:33.14	7:59:09.3	222.5	254.1	21.22	1.90	-0.02±0.09	1008± 49	S	1008± 49
3635	12:29:56.57	7:59:10.1	147.2	114.3	20.86	1.34	-1.35±0.09	893± 65	1	907± 53
								936± 94	Z	
3651	12:29:58.02	7:59:10.7	166.8	111.0	21.75	1.71	-0.47±0.12	1252± 54	3	1252± 54
3757	12:29:45.94	7:59:17.3	58.3	204.1	21.02	1.82	-0.23±0.11	1220± 95	Z	1220± 95
3788	12:29:47.87	7:59:19.6	51.2	174.5	20.80	1.87	-0.10±0.11	1174± 25	4	1174± 25
3808	12:29:39.15	7:59:19.9	134.5	248.0	20.35	1.83	-0.21±0.12	832± 35	S	832± 35
3900	12:29:49.53	7:59:25.7	53.7	146.6	21.04	1.89	-0.05±0.11	662± 50	4	662± 50
3909	12:30:06.11	7:59:26.1	279.4	99.2	21.43	1.36	-1.31±0.07	1253± 90	Z	1253± 90
3980	12:29:35.60	7:59:30.8	181.8	257.4	21.15	1.28	-1.48±0.10	1112± 45	S	1134± 43
								1369±144	1	

Table 2—Continued

ID	α (J2000)	δ (J2000)	R (arcsec)	Θ (deg)	T_1 (mag)	$(C - T_1)$ (mag)	[Fe/H] (dex)	$v_{p,i}$ (km s ⁻¹)	Source ¹	$\langle v_p \rangle$ (km s ⁻¹)
3990	12:29:52.89	7:59:31.7	88.4	116.1	21.23	2.12	0.49±0.12	1286± 89	3	1286± 89
4017	12:29:57.59	7:59:33.6	153.8	103.9	20.92	1.42	-1.17±0.09	949± 96	1	900± 44
								888± 50	4	
4062	12:29:45.38	7:59:36.9	46.4	223.7	20.77	2.01	0.23±0.14	614± 50	4	614± 50
4125	12:29:39.16	7:59:41.6	127.8	257.0	22.11	1.72	-0.47±0.15	1435±169	1	1435±169
4144	12:30:02.01	7:59:43.1	216.7	97.3	20.74	1.33	-1.37±0.06	884± 25	4	884± 25
4168	12:29:40.18	7:59:44.8	112.2	256.8	20.36	1.68	-0.55±0.10	1384± 44	S	1445± 21
								1465± 25	4	
4187	12:30:00.02	7:59:46.6	186.9	97.4	21.75	1.90	-0.03±0.10	981±156	1	981±156
4210	12:30:06.78	7:59:48.6	286.6	94.4	20.53	1.62	-0.69±0.05	1910± 29	Z	1910± 29
4216	12:29:25.97	7:59:49.0	321.0	266.2	22.25	1.14	-1.83±0.10	591± 70	2	591± 70
4217	12:29:52.04	7:59:49.4	70.1	107.5	20.66	1.79	-0.29±0.09	887±135	1	1067± 23
								1040± 76	3	
								1077± 25	4	
4296	12:30:04.68	7:59:54.1	255.1	93.7	20.79	1.27	-1.52±0.07	1212± 25	4	1214± 23
								1234± 67	3	
4297	12:29:37.74	7:59:54.1	146.5	263.6	21.41	1.49	-0.98±0.11	1435±163	1	1435±163
4332	12:30:01.46	7:59:56.4	207.3	93.9	21.95	1.16	-1.78±0.09	878±134	1	878±134
4351	12:29:49.03	7:59:57.5	25.6	120.4	20.38	1.37	-1.27±0.12	263± 25	4	263± 25
4386	12:29:51.70	8:00:00.2	62.6	99.5	19.83	1.94	0.05±0.10	1197± 33	S	1197± 33
4401	12:30:00.25	8:00:01.8	189.0	92.7	20.85	1.91	0.00±0.08	1286± 25	4	1286± 25
4436	12:29:41.01	8:00:03.7	97.2	266.0	21.29	1.90	-0.04±0.12	1047±119	1	1047±119
4443	12:29:55.86	8:00:04.0	123.8	93.0	21.53	1.72	-0.47±0.12	1126±124	3	1126±124
4494	12:29:37.06	8:00:07.2	155.7	268.8	20.99	1.42	-1.15±0.10	1132±166	1	1132±166
4513	12:29:42.31	8:00:08.2	77.7	268.3	20.10	1.85	-0.14±0.13	908± 80	S	991± 23
								1000± 25	4	
4541	12:29:54.22	8:00:10.3	99.3	90.1	20.83	1.56	-0.79±0.10	733± 25	4	733± 25
4582	12:29:38.23	8:00:13.0	138.2	271.1	21.66	1.93	0.04±0.13	475±136	1	475±136
4628	12:29:26.21	8:00:16.3	316.8	271.1	20.66	1.29	-1.47±0.09	726± 52	3	726± 52
4663	12:29:59.27	8:00:18.9	174.3	91.6	20.38	1.87	-0.10±0.08	1194± 25	4	1194± 25
4682	12:29:55.55	8:00:20.2	119.4	85.4	21.42	1.55	-0.86±0.09	900± 50	4	900± 50
4721	12:29:51.42	8:00:23.2	59.0	77.6	21.32	1.77	-0.34±0.13	386±131	1	386±131
4731	12:29:42.09	8:00:23.5	82.0	279.2	19.96	1.43	-1.14±0.10	698± 57	S	698± 57
4780	12:29:53.32	8:00:26.4	87.4	79.5	19.52	1.95	0.09±0.10	971± 45	S	971± 45
4834	12:29:44.50	8:00:30.1	49.2	293.5	20.24	1.47	-1.04±0.09	1221± 50	4	1221± 50
4852	12:29:56.33	8:00:31.1	132.2	81.1	21.13	2.04	0.30±0.11	1127± 25	4	1127± 25
4862	12:29:42.19	8:00:31.7	82.2	285.0	21.07	1.73	-0.42±0.12	1028±108	1	1028±108
4864	12:29:57.01	8:00:31.9	142.3	81.4	20.63	1.99	0.18±0.09	385±161	1	312± 24
								311± 25	4	
4882	12:29:28.46	8:00:32.9	284.3	274.6	20.68	1.35	-1.32±0.07	564± 62	3	564± 62
4959	12:29:55.58	8:00:37.5	122.5	77.3	21.38	1.33	-1.38±0.10	1449± 44	S	1449± 44
5003	12:29:43.05	8:00:40.2	73.0	294.0	20.72	1.43	-1.13±0.12	770± 25	4	770± 25
5018	12:29:43.78	8:00:41.4	63.8	299.0	20.70	2.04	0.30±0.11	614± 50	4	614± 50
5090	12:29:41.97	8:00:45.6	89.9	293.1	19.83	1.61	-0.70±0.12	582± 46	S	582± 46
5097	12:29:37.74	8:00:46.3	149.8	283.8	20.76	2.18	0.62±0.11	864± 70	1	824± 40
								804± 50	4	
5182	12:29:58.80	8:00:50.4	172.0	76.6	20.94	1.57	-0.79±0.08	1292± 84	1	1292± 84
5213	12:29:40.13	8:00:52.0	117.6	290.7	20.89	1.64	-0.65±0.10	954± 69	1	954± 69
5217	12:29:52.92	8:00:52.5	90.3	62.3	20.60	1.32	-1.39±0.08	553± 50	4	553± 50
5281	12:29:37.49	8:00:56.7	156.2	287.3	21.28	1.38	-1.25±0.10	1400±131	1	1400±131
5282	12:30:03.57	8:00:56.9	242.5	79.0	21.90	1.95	0.08±0.13	1356± 68	3	1356± 68

Table 2—Continued

ID	α (J2000)	δ (J2000)	R (arcsec)	Θ (deg)	T_1 (mag)	$(C - T_1)$ (mag)	[Fe/H] (dex)	$v_{p,i}$ (km s ⁻¹)	Source ¹	$\langle v_p \rangle$ (km s ⁻¹)
5400	12:29:43.70	8:01:03.6	77.9	313.0	20.70	1.32	-1.40±0.07	918±113	1	918±113
5456	12:29:45.03	8:01:06.9	67.6	326.6	19.26	1.39	-1.23±0.10	882± 65	M	882± 65
5501	12:29:34.11	8:01:10.1	208.2	286.7	21.63	1.48	-1.01±0.12	799±158	1	799±158
5561	12:29:29.39	8:01:13.6	276.9	283.2	20.82	1.39	-1.22±0.08	903± 48	S	903± 48
5564	12:30:07.38	8:01:14.2	301.6	77.8	21.26	1.37	-1.29±0.06	862± 19	Z	862± 19
5629	12:29:44.44	8:01:17.7	81.4	325.6	21.09	1.36	-1.29±0.12	522± 52	S	522± 52
5694	12:29:57.41	8:01:21.0	162.7	64.3	21.89	2.02	0.25±0.10	1185±130	1	1185±130
5707	12:29:45.17	8:01:21.4	79.1	333.6	21.47	1.44	-1.11±0.12	1712± 30	Z	1712± 30
5750	12:29:44.62	8:01:24.4	85.7	329.6	21.50	1.47	-1.05±0.10	1063± 89	Z	1063± 89
5821	12:30:09.22	8:01:29.8	331.7	76.2	21.73	1.30	-1.44±0.07	928± 59	3	928± 59
5856	12:29:41.64	8:01:32.1	119.7	313.0	21.03	1.13	-1.84±0.13	1059±104	1	1053± 65
								1050± 84	Z	
6051	12:29:39.09	8:01:44.7	156.9	306.9	20.94	1.31	-1.41±0.07	973± 88	1	927± 40
								1000±110	1	
								897± 50	4	
6092	12:29:52.17	8:01:47.4	118.8	35.4	20.92	1.54	-0.88±0.09	804±147	1	804±147
6108	12:29:57.19	8:01:48.4	173.6	55.7	21.49	1.42	-1.15±0.07	913± 39	Z	913± 39
6164	12:29:44.79	8:01:52.6	110.0	338.2	19.79	1.65	-0.61±0.09	426± 30	S	426± 30
6177	12:30:02.82	8:01:53.6	249.3	65.6	21.02	1.45	-1.10±0.06	1187± 86	1	1187± 86
6198	12:30:05.76	8:01:55.4	290.3	68.8	20.75	1.51	-0.94±0.07	306± 53	3	306± 53
6220	12:29:37.87	8:01:57.3	179.0	306.7	21.50	1.32	-1.39±0.12	1213±145	1	1213±145
6231	12:29:49.09	8:01:58.0	110.0	12.2	20.77	1.82	-0.22±0.09	1119± 87	1	1100± 36
								1046± 50	Z	
								1182± 65	M	
6284	12:29:57.92	8:02:02.4	190.5	54.1	19.44	1.57	-0.81±0.10	569± 54	S	569± 54
6294	12:29:33.84	8:02:03.1	232.5	299.0	21.02	1.64	-0.63±0.09	1034± 84	S	1034± 84
6344	12:29:40.14	8:02:07.0	160.1	316.7	20.89	2.01	0.23±0.11	1266± 60	1	1257± 34
								1337± 79	1	
								1220± 50	Z	
6357	12:29:52.67	8:02:07.4	139.6	33.1	20.47	1.26	-1.53±0.09	958± 29	Z	958± 29
6388	12:29:55.68	8:02:10.1	170.0	45.4	20.18	1.36	-1.30±0.07	1212± 24	Z	1212± 24
6394	12:29:35.57	8:02:10.4	214.4	304.0	21.40	1.42	-1.16±0.11	760± 85	Z	760± 85
6427	12:29:45.01	8:02:13.0	128.1	343.0	21.11	1.79	-0.28±0.10	1141± 50	S	1141± 50
6476	12:30:15.54	8:02:15.9	434.5	73.3	20.94	2.23	0.74±0.12	966± 36	Z	966± 36
6479	12:29:41.04	8:02:16.1	158.5	322.5	21.60	1.94	0.07±0.10	1124±132	1	1124±132
6485	12:29:55.03	8:02:16.8	168.3	41.4	21.07	1.53	-0.89±0.09	510± 82	Z	510± 82
6511	12:29:57.40	8:02:18.5	194.5	48.9	21.76	1.95	0.08±0.09	1029±127	1	1029±127
6519	12:29:42.42	8:02:19.2	149.5	329.4	21.03	1.26	-1.54±0.09	347± 79	1	347± 79
6520	12:29:49.28	8:02:19.0	131.1	11.4	20.06	1.86	-0.14±0.10	607± 57	S	607± 57
6564	12:29:43.31	8:02:22.7	146.4	334.6	20.03	1.34	-1.34±0.11	1077± 31	S	1077± 31
6615	12:30:14.00	8:02:27.0	416.1	70.9	20.48	1.47	-1.05±0.11	1923± 49	Z	1923± 49
6647	12:29:38.13	8:02:29.2	196.9	314.8	21.33	1.30	-1.44±0.09	672±125	1	672±125
6696	12:29:53.98	8:02:34.0	172.5	33.7	20.08	1.59	-0.76±0.09	550± 52	S	559± 21
								561± 23	Z	
6701	12:29:26.20	8:02:33.9	347.9	294.4	20.97	2.00	0.19±0.06	1092±141	Z	1303± 50
								1334± 54	3	
6721	12:29:39.90	8:02:35.9	184.5	322.1	21.09	1.73	-0.44±0.08	1180± 45	S	1209± 40
								1329± 91	1	
6748	12:29:40.78	8:02:37.8	178.3	325.8	20.21	1.53	-0.90±0.09	817± 20	Z	817± 20
6872	12:29:41.75	8:02:46.1	177.8	331.1	20.15	1.46	-1.08±0.10	870± 41	S	870± 41
6905	12:29:29.53	8:02:48.9	310.8	300.7	22.18	1.67	-0.58±0.12	1065± 69	3	1065± 69

Table 2—Continued

ID	α (J2000)	δ (J2000)	R (arcsec)	Θ (deg)	T_1 (mag)	$(C - T_1)$ (mag)	[Fe/H] (dex)	$v_{p,i}$ (km s ⁻¹)	Source ¹	$\langle v_p \rangle$ (km s ⁻¹)
6989	12:29:54.53	8:02:56.2	195.5	32.1	20.61	1.75	-0.38±0.07	1009± 24	Z	1028± 21
								1154± 87	1	
								1071± 50	S	
7028	12:30:12.03	8:02:59.2	401.1	65.2	21.40	1.38	-1.24±0.07	1548± 39	Z	1548± 39
7043	12:29:29.23	8:02:59.7	320.2	301.9	20.47	1.78	-0.31±0.08	808± 67	Z	808± 67
7095	12:30:01.57	8:03:05.4	272.1	50.0	21.43	1.56	-0.83±0.08	1285± 80	Z	1285± 80
7110	12:29:41.98	8:03:06.6	194.6	334.9	21.82	1.35	-1.32±0.09	1242±138	1	1242±138
7157	12:29:36.85	8:03:11.0	240.4	318.7	21.52	1.57	-0.81±0.10	804± 90	1	804± 90
7197	12:29:40.98	8:03:13.6	207.5	332.0	20.94	1.50	-0.96±0.11	782± 50	S	782± 50
7281	12:29:53.17	8:03:19.4	206.5	23.9	21.43	1.25	-1.55±0.10	389±123	Z	389±123
7340	12:29:49.93	8:03:24.5	197.2	10.4	20.91	1.77	-0.33±0.08	1067± 29	Z	1079± 28
								1308±124	S	
7364	12:29:31.27	8:03:26.8	311.3	309.1	21.36	1.36	-1.31±0.08	1522±100	Z	1522±100
7382	12:29:41.39	8:03:29.0	218.4	335.3	21.12	1.56	-0.83±0.09	860±131	1	860±131
7390	12:29:40.01	8:03:29.8	228.6	330.7	21.48	1.73	-0.43±0.09	301± 89	1	301± 89
7399	12:29:33.87	8:03:30.5	285.0	314.6	20.35	1.40	-1.20±0.07	1005± 44	S	1005± 44
7430	12:29:25.60	8:03:31.8	383.1	301.7	20.76	1.41	-1.18±0.08	862± 66	Z	895± 48
								934± 70	3	
7449	12:29:19.99	8:03:33.0	456.5	296.4	20.75	1.65	-0.62±0.05	724± 65	Z	724± 65
7458	12:29:44.76	8:03:34.1	207.7	348.6	20.75	1.84	-0.18±0.09	807± 57	S	807± 57
7478	12:29:51.98	8:03:35.8	215.7	17.8	21.10	1.47	-1.05±0.08	791±154	1	791±154
7531	12:29:25.10	8:03:38.8	393.1	302.0	19.71	2.07	0.38±0.07	818± 72	Z	818± 72
7548	12:29:41.51	8:03:40.7	228.5	337.0	20.57	1.62	-0.68±0.08	1110± 76	1	1136± 59
								1175± 94	1	
7616	12:29:49.08	8:03:45.7	216.4	6.1	21.35	1.49	-0.99±0.08	600± 90	Z	600± 90
7638	12:29:54.52	8:03:47.8	240.8	25.6	21.19	2.05	0.32±0.09	1219±127	1	1219±127
7659	12:29:43.09	8:03:49.5	228.7	343.3	19.87	1.34	-1.34±0.10	1520± 44	Z	1539± 34
								1571± 56	S	
7702	12:30:11.38	8:03:53.1	418.3	57.9	21.19	1.88	-0.07±0.09	1388± 58	Z	1388± 58
7746	12:29:59.53	8:03:57.1	288.2	38.2	21.29	1.42	-1.15±0.07	712± 68	Z	755± 60
								932±137	1	
7784	12:29:55.74	8:03:60.0	259.8	28.0	19.20	1.52	-0.92±0.10	868± 51	S	868± 51
7798	12:30:05.08	8:04:01.1	347.9	48.5	20.96	1.39	-1.23±0.07	1340± 39	Z	1340± 39
7872	12:29:47.24	8:04:07.5	237.0	359.0	20.33	1.45	-1.08±0.08	908± 77	Z	908± 77
7883	12:30:01.27	8:04:09.3	314.1	40.5	21.32	1.33	-1.36±0.08	1079±108	1	1079±108
7886	12:29:28.54	8:04:09.4	369.7	310.3	20.62	1.58	-0.78±0.07	1208± 57	3	1229± 28
								1236± 33	Z	
7889	12:29:58.01	8:04:09.1	284.8	33.1	18.84	1.58	-0.78±0.10	770± 65	M	770± 65
7894	12:29:34.53	8:04:09.6	302.0	320.3	21.61	1.73	-0.43±0.11	730± 81	S	730± 81
7914	12:29:50.60	8:04:11.9	245.7	10.7	21.20	1.33	-1.37±0.08	1101± 29	Z	1101± 29
7938	12:29:44.44	8:04:13.4	247.2	349.3	20.92	1.44	-1.12±0.08	1298± 96	1	1261± 44
								1251± 50	S	
7945	12:29:24.47	8:04:13.5	420.0	305.4	19.79	1.59	-0.76±0.05	651± 33	Z	651± 33
8000	12:30:00.95	8:04:18.9	318.4	38.8	21.08	1.49	-1.00±0.05	368± 40	Z	399± 36
								544± 86	1	
8090	12:29:45.67	8:04:26.4	257.4	353.8	20.51	1.46	-1.06±0.11	903± 66	S	903± 66
8143	12:30:04.26	8:04:30.4	359.4	43.7	20.96	1.52	-0.91±0.05	672±109	Z	672±109
8164	12:29:58.85	8:04:32.5	311.2	32.7	21.32	2.04	0.29±0.09	738± 40	Z	769± 36
								916± 86	1	
8165	12:29:56.09	8:04:32.4	291.1	25.9	20.22	1.39	-1.24±0.06	1027± 47	S	1027± 47
8210	12:29:26.69	8:04:35.4	407.5	310.6	20.43	1.32	-1.40±0.07	576± 88	Z	576± 88

Table 2—Continued

ID	α (J2000)	δ (J2000)	R (arcsec)	Θ (deg)	T_1 (mag)	$(C - T_1)$ (mag)	[Fe/H] (dex)	$v_{p,i}$ (km s ⁻¹)	Source ¹	$\langle v_p \rangle$ (km s ⁻¹)
8228	12:29:41.74	8:04:37.6	280.7	342.2	21.48	1.77	-0.33±0.11	910±168	1	910±168
8254	12:29:26.30	8:04:40.3	415.0	310.6	21.40	1.44	-1.12±0.07	1025± 77	3	1025± 77
8273	12:29:33.64	8:04:41.3	340.5	322.7	20.60	1.43	-1.14±0.11	784± 90	Z	784± 90
8332	12:29:43.83	8:04:46.8	281.8	348.8	21.09	1.41	-1.19±0.08	1109± 99	1	1167± 70
								1226±100	Z	
8353	12:29:41.24	8:04:48.2	293.1	341.4	20.03	1.98	0.15±0.10	928± 40	S	928± 40
8357	12:29:36.87	8:04:48.3	319.8	330.3	20.26	1.45	-1.10±0.07	981± 61	Z	981± 61
8384	12:29:47.83	8:04:49.9	279.4	0.9	21.39	1.41	-1.18±0.07	768± 54	S	768± 54
8409	12:29:22.37	8:04:51.6	467.7	307.0	21.18	1.39	-1.23±0.08	1089± 62	3	1089± 62
8596	12:30:06.88	8:05:10.3	415.2	43.8	19.73	1.31	-1.42±0.11	888± 31	Z	888± 31
8606	12:29:24.43	8:05:10.7	456.0	311.2	21.13	1.80	-0.26±0.06	1380± 67	3	1380± 67
8630	12:29:38.30	8:05:12.4	331.7	335.6	22.22	1.57	-0.82±0.10	1082±141	1	1082±141
8653	12:29:16.38	8:05:14.7	553.8	303.4	20.50	1.26	-1.53±0.09	744± 44	Z	744± 44
8712	12:30:13.50	8:05:20.4	494.7	51.2	20.93	1.49	-0.98±0.06	817± 63	Z	817± 63
8740	12:29:42.30	8:05:23.2	322.2	346.1	21.27	2.14	0.53±0.07	380±124	1	688± 80
								913±106	Z	
8890	12:29:48.29	8:05:39.5	329.2	2.0	20.41	1.88	-0.08±0.06	870± 65	S	870± 65
8919	12:29:34.36	8:05:41.4	384.4	329.4	19.87	1.45	-1.08±0.13	1014± 65	Z	1014± 65
9009	12:29:44.80	8:05:49.8	341.8	353.2	21.28	1.99	0.18±0.08	1218±120	1	1218±120
9087	12:29:58.26	8:05:59.2	383.3	24.6	22.25	1.97	0.12±0.13	1262±157	1	1262±157
9145	12:30:14.87	8:06:04.8	538.9	48.9	19.79	1.76	-0.35±0.14	973± 38	Z	973± 38
9360	12:29:19.15	8:06:32.0	568.6	312.2	21.00	1.67	-0.58±0.09	1191± 99	Z	1191± 99
9414	12:29:38.63	8:06:39.9	411.3	341.3	20.82	1.74	-0.41±0.06	664±111	1	813± 37
								832± 40	Z	
9527	12:29:32.40	8:06:57.4	464.8	331.1	20.91	1.58	-0.78±0.10	941± 61	Z	941± 61
9666	12:29:51.39	8:07:16.8	430.2	7.7	20.04	1.74	-0.42±0.07	811± 71	Z	811± 71
9991	12:29:58.92	7:58:01.0	212.9	127.5	19.41	1.27	-1.51±0.10	1156± 65	M	1156± 65
9992	12:29:48.34	8:00:42.2	33.9	20.5	19.99	1.47	-1.04±0.10	795± 65	M	795± 65
<u>Foreground Stars and Background Galaxies</u>										
902	12:29:30.17	7:55:27.1	383.2	222.3	20.55	1.15		-19± 65	2	-19± 65
1608	12:29:27.99	7:56:35.0	361.6	233.5	21.39	2.24		-40± 48	2	-40± 48
1824	12:29:33.92	7:56:52.9	282.9	225.7	21.61	1.24		242± 63	2	242± 63
2071	12:29:57.92	7:57:14.9	233.7	138.7	21.03	1.38		-25± 73	1	-25± 73
2668	12:30:10.37	7:58:06.5	361.1	110.1	20.72	1.10		228± 72	3	228± 72
2860	12:29:54.56	7:58:18.4	153.1	137.1	20.27	1.21		-10± 15	4	-10± 15
4497	12:30:00.58	8:00:07.4	193.7	91.0	22.18	1.33		6960±146	1	6960±146
5323	12:29:48.83	8:00:59.3	52.4	21.4	20.33	0.82		1357± 65	M	1357± 65
8096	12:29:20.93	8:04:26.8	471.1	303.0	21.81	1.68		75± 51	3	75± 51
9086	12:29:27.33	8:05:59.0	459.9	319.3	21.80	1.30		10± 54	3	10± 54
9228	12:29:41.62	8:06:16.2	376.1	346.5	21.02	1.61		155±172	1	155±172
<u>Discrepant Objects²</u>										
1982	12:29:41.67	7:57:07.4	202.8	205.5	20.89	1.01	-2.02±0.11	648± 43	Z	2558± 41
								25800±150	4	
2256	12:29:47.53	7:57:31.4	159.1	180.1	21.24	1.90	0.08±0.13	242± 61	3	830± 25
								954± 28	Z	

¹Key to Source codes: (M) Mould *et al.* (1990); (S) Sharples *et al.* (1998); (Z) Zepf *et al.* (2000); (1-4) as given in Table 1.

²Omitted from final GC sample.

Table 3. Kinematics of the M49 Globular Cluster System¹

R (arcsec)	$\langle R \rangle$ (arcsec)	N	\overline{v}_p (km s ⁻¹)	σ_p (km s ⁻¹)	Θ_0^2 (deg)	ΩR^2 (km s ⁻¹)	$\sigma_{p,r}^2$ (km s ⁻¹)
Full Sample: 263 Clusters with $1.00 \leq (C - T_1) \leq 2.25$							
25–570	234	263	973 ⁺²² ₋₂₃	313 ⁺²⁷ ₋₉	105 ⁺⁴⁵ ₋₄₅	53 ⁺⁵² ₋₂₅	312 ⁺²⁷ ₋₈
25–150	110	58	910 ⁺⁴³ ₋₅₄	328 ⁺³³ ₋₃₂	-168 ⁺⁴¹ ₋₄₂	115 ⁺¹⁰³ ₋₆₀	335 ⁺³⁶ ₋₃₆
150–250	207	87	1025 ⁺³⁵ ₋₃₈	306 ⁺³⁵ ₋₂₁	96 ⁺⁵³ ₋₄₈	55 ⁺⁸¹ ₋₄₇	302 ⁺³³ ₋₂₂
250–350	300	69	993 ⁺³⁹ ₋₄₆	294 ⁺⁴¹ ₋₂₆	74 ⁺²⁴ ₋₂₅	223 ⁺⁸⁰ ₋₅₅	307 ⁺⁴⁴ ₋₃₆
350–570	418	49	925 ⁺⁴⁸ ₋₅₁	329 ⁺⁵⁰ ₋₄₈	-56 ⁺⁴⁴ ₋₃₈	123 ⁺¹³⁵ ₋₇₈	331 ⁺⁴³ ₋₄₈
Metal-poor Sample: 158 Clusters with $1.00 \leq (C - T_1) < 1.625$							
25–570	251	158	957 ⁺³² ₋₂₈	345 ⁺³⁴ ₋₁₈	100 ⁺³⁷ ₋₄₀	93 ⁺⁶⁹ ₋₃₇	342 ⁺³³ ₋₁₈
25–150	107	26	869 ⁺⁷² ₋₆₄	326 ⁺⁶² ₋₇₀	50 ⁺⁴⁵ ₋₃₅	-180 ⁺¹¹⁴ ₋₁₆₄	353 ⁺⁶⁴ ₋₈₉
150–250	209	53	1017 ⁺⁵⁵ ₋₄₇	350 ⁺³⁹ ₋₃₂	96 ⁺³¹ ₋₃₅	162 ⁺¹⁰⁷ ₋₆₆	324 ⁺⁴¹ ₋₃₈
250–350	296	48	985 ⁺⁵¹ ₋₅₈	333 ⁺⁴⁸ ₋₄₇	73 ⁺³⁰ ₋₂₆	233 ⁺¹¹⁶ ₋₈₁	352 ⁺⁴² ₋₅₃
350–570	415	31	878 ⁺⁷⁷ ₋₅₈	359 ⁺⁶⁸ ₋₆₉	-58 ⁺⁴⁶ ₋₅₀	127 ⁺¹⁸⁸ ₋₁₄₃	367 ⁺⁵² ₋₇₀
Metal-rich Sample: 105 Clusters with $1.625 \leq (C - T_1) \leq 2.25$							
25–570	202	105	999 ⁺³¹ ₋₂₉	265 ⁺³⁰ ₋₁₄	195 ⁺⁵⁶ ₋₅₈	12 ⁺⁷⁶ ₋₇₄	265 ⁺³⁴ ₋₁₃
25–150	110	32	946 ⁺⁹⁸ ₋₈₁	334 ⁺³³ ₋₆₂	153 ⁺⁵⁵ ₋₅₄	93 ⁺¹⁴¹ ₋₁₃₆	329 ⁺³⁵ ₋₅₉
150–250	196	34	1047 ⁺⁴³ ₋₄₅	231 ⁺⁴⁶ ₋₃₅	97 ⁺⁴¹ ₋₃₅	-86 ⁺²² ₋₆₁	199 ⁺⁵³ ₋₂₈
250–350	311	21	1008 ⁺⁵⁸ ₋₅₉	208 ⁺⁴⁴ ₋₁₆
350–570	435	18	993 ⁺⁶¹ ₋₉₅	274 ⁺⁵⁷ ₋₅₆	130 ⁺⁴⁶ ₋₄₆	-114 ⁺⁹⁵ ₋₁₅₂	277 ⁺³⁸ ₋₇₄

¹All uncertainties correspond to 68% (1- σ) confidence intervals.

²Systemic velocity held fixed in fit of sine curve: $v_{\text{sys}} \equiv 997 \text{ km s}^{-1}$.

Table 4. Global Kinematic Properties of GCs in M87 and M49¹

	M87					M49 ²				
	N	$\sigma_{p,r}$ (km s ⁻¹)	ΩR (km s ⁻¹)	Θ_0^3 (deg)	$\Omega R/\sigma_{p,r}$	N	$\sigma_{p,r}$ (km s ⁻¹)	ΩR (km s ⁻¹)	Θ_0^4 (deg)	$\Omega R/\sigma_{p,r}$
All GCs	278	383 ⁺³¹ ₋₇	171 ⁺³⁹ ₋₃₀	70 ⁺¹¹ ₋₁₄	0.45 ^{+0.09} _{-0.09}	253	316 ⁺²⁷ ₋₈	48 ⁺⁵² ₋₂₆	109 ⁺⁴⁴ ₋₄₇	0.15 ^{+0.15} _{-0.08}
Metal-Poor GCs	161	397 ⁺³⁶ ₋₁₄	186 ⁺⁵⁸ ₋₄₁	61 ⁺¹⁷ ₋₁₈	0.47 ^{+0.13} _{-0.11}	158	342 ⁺³³ ₋₁₈	93 ⁺⁶⁹ ₋₃₇	100 ⁺³⁷ ₋₄₀	0.27 ^{+0.19} _{-0.11}
..... $R \leq 2R_{\text{eff}}$ ⁵	46	345 ⁺⁵¹ ₋₄₂	81 ⁺¹¹⁸ ₋₈₅	-14 ⁺⁴⁷ ₋₄₆	0.23 ^{+0.34} _{-0.25}					
Metal-Rich GCs	117	365 ⁺³⁸ ₋₁₈	155 ⁺⁵³ ₋₃₇	81 ⁺¹⁷ ₋₂₀	0.43 ^{+0.14} _{-0.12}	95	265 ⁺³⁴ ₋₁₃	-26 ⁺⁶⁴ ₋₇₉	45 ⁺⁵⁵ ₋₅₄	0.10 ^{+0.27} _{-0.25}

¹All uncertainties correspond to 68% confidence intervals.

²The 10 metal-rich clusters between $302'' \leq R \leq 337''$ in M49 have been omitted.

³The rotation axis of the galaxy has position angle $-23^\circ \pm 10^\circ$ inside $R \lesssim R_{\text{eff}}$ (Davies & Birkinshaw 1988).

⁴The rotation axis of the galaxy has position angle $59^\circ \pm 3^\circ$ (Davies & Birkinshaw 1988).

⁵ $R_{\text{eff}} = 96'' \simeq 7$ kpc for M87 (de Vaucouleurs & Nieto 1978).

REFERENCES

- Bahcall, J.N., & Soneira, R.M. 1980, *ApJS*, 44, 73
- Bahcall, J.N. 1986, *ARA&A*, 24, 577
- Beasley, M.A., Sharples, R.M., Bridges, T.J., Hanes, D.A., Zepf, S.E., Ashman, K.M., & Geisler, D. 2000, *MNRAS*, 318, 1249
- Beers, T. C., Flynn, K., & Gebhardt, K. 1990, *AJ*, 100, 32
- Binggeli, B., Tammann, G.A., & Sandage, A.R. 1987, *AJ*, 94, 251
- Binggeli, B., Popescu, C.C., & Tammann, G.A. 1993, *A&AS*, 98, 275
- Blakeslee, J.P., Tonry, J.L., & Metzger, M.R. 1997, *AJ*, 114, 482
- Blakeslee, J.P. 1999, *AJ*, 118, 1506
- Brighenti, F., & Mathews, W.G. 1997, *ApJ*, 486, L83
- Caon, N., Capaccioli, M.; D’Onofrio, M. 1994, *A&AS*, 106, 199
- Caon, N., Macchetto, D., & Pastoriza, M. 2000, *A&AS*, 127, 39
- Cohen, J.G., & Ryzhov, A. 1997, *ApJ*, 486, 230
- Cohen, J.G., Blakeslee, J.P., & Ryzhov, A. 1998, *ApJ*, 496, 808
- Cohen, J.G., Blakeslee, J.P., & Côté, P. 2003, *AJ*, submitted.
- Cohen, J.G. 2000, *AJ*, 119, 162
- Côté, P. 1999, *AJ*, 118, 406
- Côté, P., McLaughlin, D.E., Hanes, D.A., Bridges, T.J., Geisler, D., Merritt, D., Hesser, J.E., Harris, G.L.H., & Lee, M.G. 2001, *ApJ*, 559, 828
- Côté, P. 2003, in *New Horizons in Globular Cluster Astronomy*, ed. G. Piotto, G. Meylan, S.J. Djorgovski & M. Riello (San Francisco: ASP), in press
- Davies, R.L., & Birkinshaw, M. 1988, *ApJS*, 68, 409
- Dehnen, W. 1993, *MNRAS*, 265, 250
- de Vaucouleurs, G., & Nieto, J.-L. 1978, *ApJ*, 220, 449
- Gebhardt, K. & Kissler-Patig, M. 1999, *AJ*, 118, 1526
- Geisler, D., & Forte, J.C. 1990, *ApJ*, 350, 5

- Geisler, D. 1996, *AJ*, 111, 480
- Geisler, D., Lee, M.G., & Kim, E. 1996, *AJ*, 111, 1529
- Harris, W.E., & Petrie, P.L. 1978, *ApJ*, 223, 88
- Harris, W.E. 1991, *ARA&A*, 29, 543
- Hanes, D.A., Bridges, T.J., Côté, P., Geisler, D., McLaughlin, D.E., Hesser, J.E., & Harris, G.L.H. 2001, *ApJ*, 559, 812
- Heisler, J., Tremaine, S., & Bahcall, J.N. 1985, *ApJ*, 298, 8
- Huchra, J.P., & Brodie, J.P. 1987, *AJ*, 93, 779
- Irwin, J.A., & Sarazin, C.L. 1996, *ApJ*, 471, 683
- Jordán, A., Côté, P., West, M.J., & Marzke, R.O. 2002, *ApJ*, 576, L113
- Kissler-Patig, M., & Gebhardt, K. 1998, *AJ*, 116, 2237
- Kim, E., Lee, M.G., & Geisler, D. 2000, *MNRAS*, 314, 307
- Kronawitter, A., Saglia, R. P., Gerhard, O., & Bender, R. 2000, *A&AS*, 144, 53
- Kundu, A., Whitmore, B.C., Sparks, W.B., Macchetto, F.D., Zepf, S.E., & Ashman, K.M. 1999, *ApJ*, 513, 733
- Larson, S.S., Brodie, J.P., Huchra, J.P., Forbes, D.A., & Grillmair, C.J. 2001, *AJ*, 121, 2974
- Lee, M.G., Kim, E., & Geisler, D. 1998, *AJ*, 115, 957
- Lee, M.G., & Kim, E. 2000, *AJ*, 120, 260
- McLaughlin, D.E. 1999a, *AJ*, 117, 2398
- McLaughlin, D.E. 1999b, *ApJ*, 512, L9
- McLaughlin, D.E., & Côté, P. 2003, in preparation.
- Merritt, D., & Tremblay, B. 1993, *AJ*, 106, 2229
- Merritt, D., & Ferrarese, L. 2001, *MNRAS*, 320, L30
- Mould, J.R., Oke, J.B., & Nemec, J. 1987, *AJ*, 93, 53
- Mould, J.R., Oke, J.B., de Zeeuw, P.T., & Nemec, J. 1990, *AJ*, 99, 1823
- Navarro, J.F., Frenk, C.S., & White, S.D.M. 1997, *ApJ*, 490, 493

- Oke, J.B., Cohen, J.G., Carr, M., Cromer, J., Dingizian, A., Harris, F.H., Labrecque, S., Lucinio, R., Schaal, W., Epps, H., & Miller, J. 1995, *PASP*, 107, 375
- Perrett, K.M., Bridges, T.J., Hanes, D.A., Irwin, M.J., Brodie, J.P., Carter, D., Huchra, J.P., & Watson, F.G. 2002, *AJ*, 123, 2490
- Puzia, T.H., Kissler-Patig, M., Brodie, J.P., & Huchra, J.P. 1999, *AJ*, 118, 2734
- Rhode, K. L., & Zepf, S. E. 2001, *AJ*, 121, 210
- Romanowsky, A.J., & Kochanek, C. S. 2001, *ApJ*, 553, 722
- Saglia, R.P., Bertin, G., Bertola, F., Danziger, J., Dejonghe, H., Sadler, E.M., Stiavelli, M., de Zeeuw, P.T., & Zeilinger, W.W. 1993, *ApJ*, 403, 567
- Schindler, S., Binggeli, B. & Böhringer, H. 1999, *A&A*, 343, 420
- Schlegel, D.J., Finkbeiner, D.P., & Davis, M. 1998, *ApJ*, 500, 525
- Secker, J., Geisler, D., McLaughlin, D.E., & Harris, W.E. 1995, *AJ*, 109, 1019
- Sembach, K.R., & Tonry, J.L. 1996, *AJ*, 112, 797
- Sharples, R.M., Zepf, S.E., Bridges, T.J., Hanes, D.A., Carter, D., Ashman, K.M., & Geisler, D. 1998, *AJ*, 115, 2337
- Tonry, J., & Davis, M., 1979, *AJ*, 82, 954
- van der Marel, R.P. 1994, *MNRAS*, 270, 271
- Zepf, S.E., Beasley, M.A., Bridges, T.J., Hanes, D.A., Sharples, R.M., Ashman, K.M., & Geisler, D. 2000, *AJ*, 120, 2928

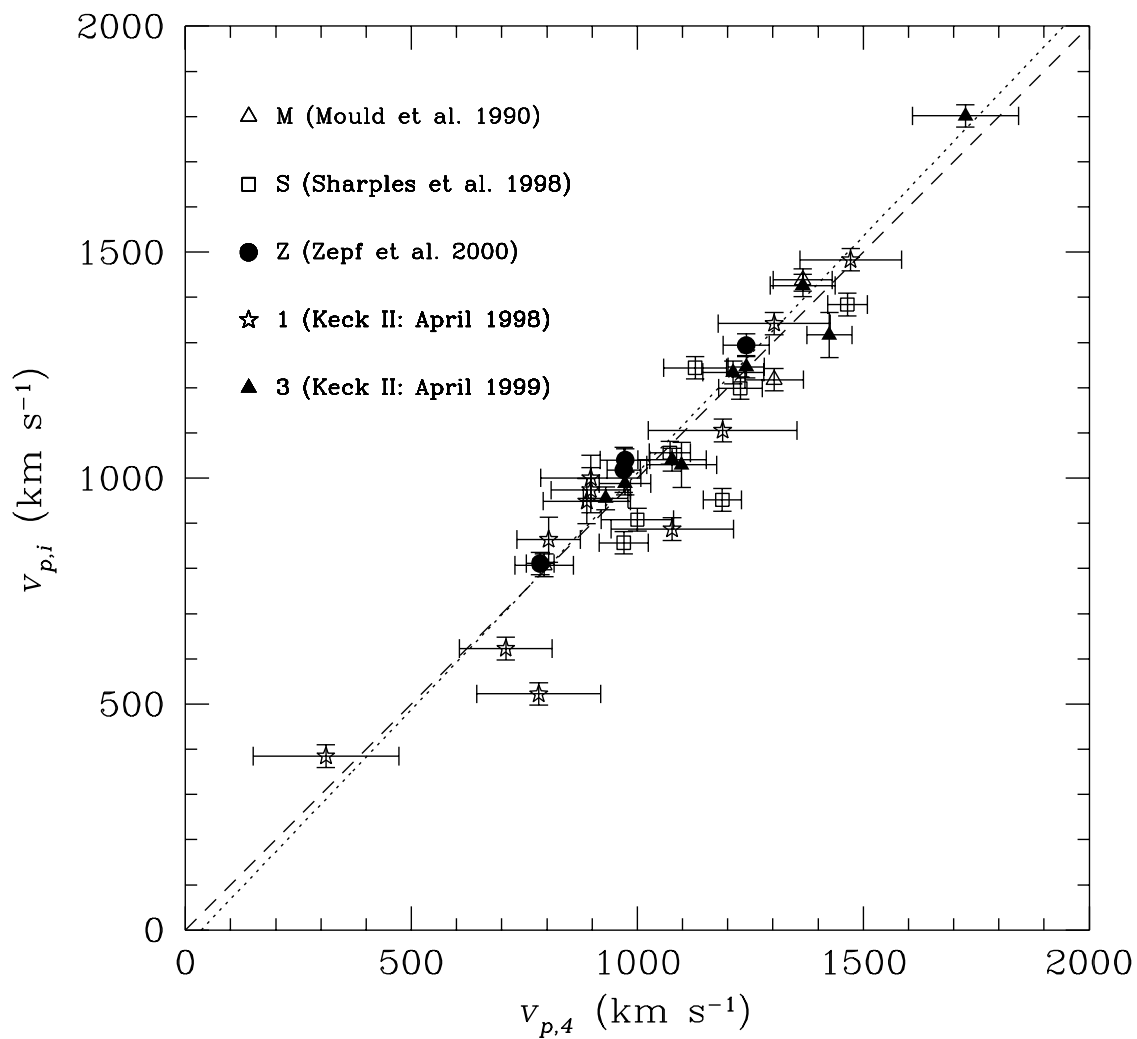


Fig. 1.— Radial velocities measured for M49 globular clusters from spectra obtained in April 2000 (i.e., run #4) plotted against independent velocity measurements from other datasets. The dashed line shows the one-to-one relation, while the dotted line shows the least-squares line of best fit.

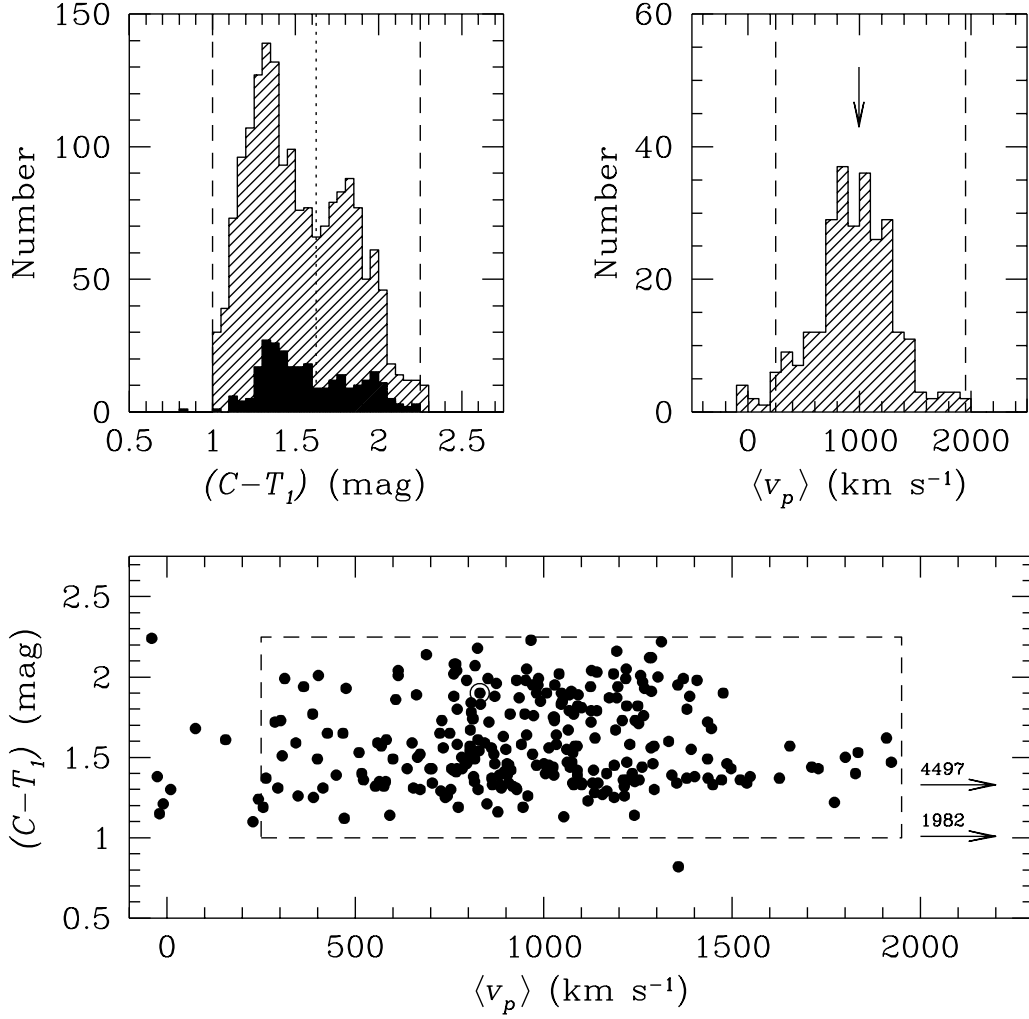


Fig. 2.— (*Upper Left Panel*) $(C - T_1)$ colors for all 1774 g lobular cluster candidates from the photometric survey of Geisler, Lee & Kim (1996) are shown as the dashed histogram. The solid histogram shows the color distribution for the 276 globular cluster candidates with measured radial velocities. The dashed lines indicate our adopted selection criteria on color: $1.00 \leq (C - T_1) \leq 2.25$ mag, while the dotted line shows the color selection used to isolate metal-rich and metal-poor subsamples: $(C - T_1) = 1.625$. (*Upper Right Panel*) Radial velocity histogram for the 276 candidate globular clusters. The vertical lines show our adopted selection criteria on velocity: $250 \leq v \leq 1950$ km s^{-1} . (*Lower Panel*) Color versus radial velocity for our initial sample of 276 objects (two objects which fall outside the plotted region — #1982 and #4497 — are indicated by the arrows). The dotted region shows the joint selection criteria on color and radial velocity. The lone circled point in this box refers to object 2256, which was discarded from the dynamical analysis due to discrepant radial velocity measurements. Excluding this object, the dashed box contains a total of 263 globular clusters.

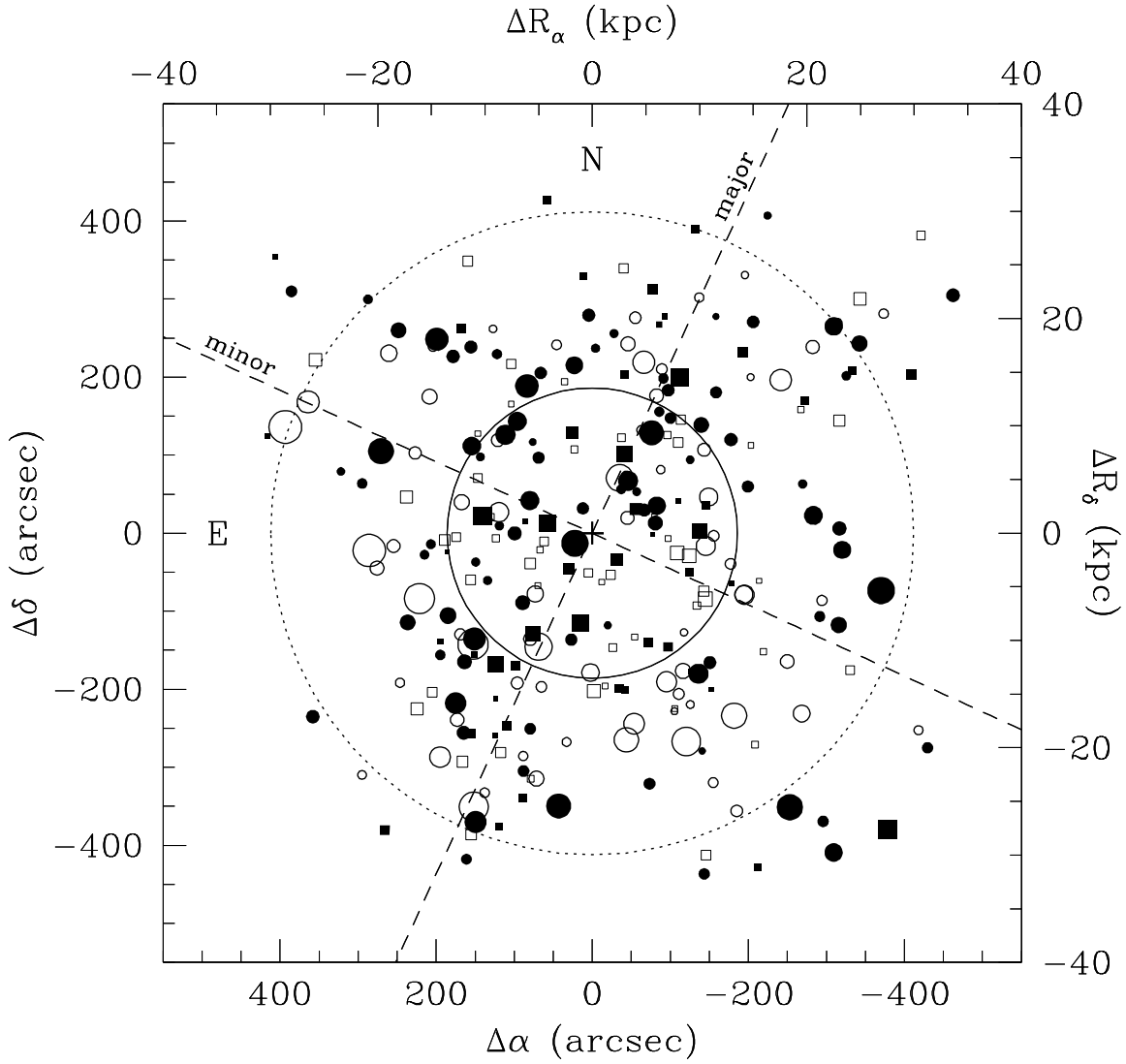


Fig. 3.— Spatial distribution of the 263 globular clusters with measured velocities. Circles and squares indicate metal-poor and metal-rich globular clusters, respectively (see text for details). For both subsamples, open and filled symbols indicate objects having positive and negative velocity residuals, $\Delta v_p = \langle v_p \rangle - v_{\text{gal}}$, respectively, where $v_{\text{gal}} = 997 \text{ km s}^{-1}$. The size of the symbol is proportional to the absolute value of the velocity residual. The center of the galaxy is marked by the cross, while the solid circle shows our estimate for the galaxy’s effective radius, $R_{\text{eff}} = 3'.1 \simeq 13.5 \text{ kpc}$, based on a fit (see §4.2) of the surface photometry of Kim *et al.* (2000). The diagonal lines show the photometric major and minor axes of the galaxy as determined by Kim *et al.* (2000). Exterior to the large, dotted circle at $R = 30 \text{ kpc}$, our sample shows an apparent dearth of globular clusters with $\langle v_p \rangle \gtrsim 1500 \text{ km s}^{-1}$. Conclusions about the kinematics of the globular cluster system beyond this point should be considered provisional.

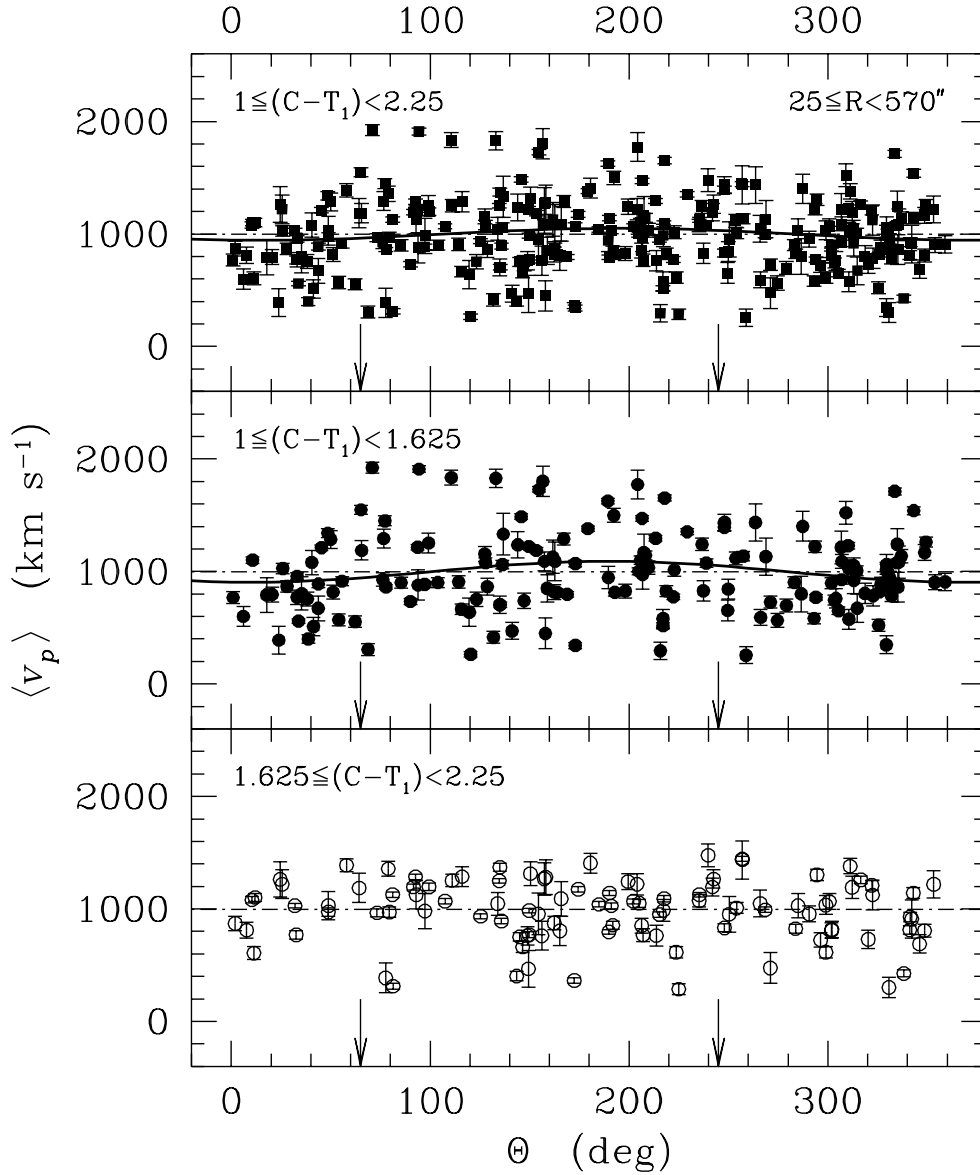


Fig. 4.— (*Upper Panel*) Radial velocity, $\langle v_p \rangle$, plotted against position angle, Θ , for the full sample of 263 globular clusters. (*Middle Panel*) $\langle v_p \rangle$ versus Θ for the sample of 158 metal-poor clusters. (*Lower Panel*) $\langle v_p \rangle$ versus Θ for the sample of 105 metal-rich globular clusters. In all three panels, the broken horizontal line indicates the galaxy’s velocity, $v_{\text{gal}} = 997 \text{ km s}^{-1}$; in the top two, the best-fit sine functions from Table 3 are shown as bold, solid curves. The position angles of the photometric minor axis of M49 (Kim *et al.* 2000) are indicated by the vertical arrows at $\Theta = 65^\circ$ and 245° .

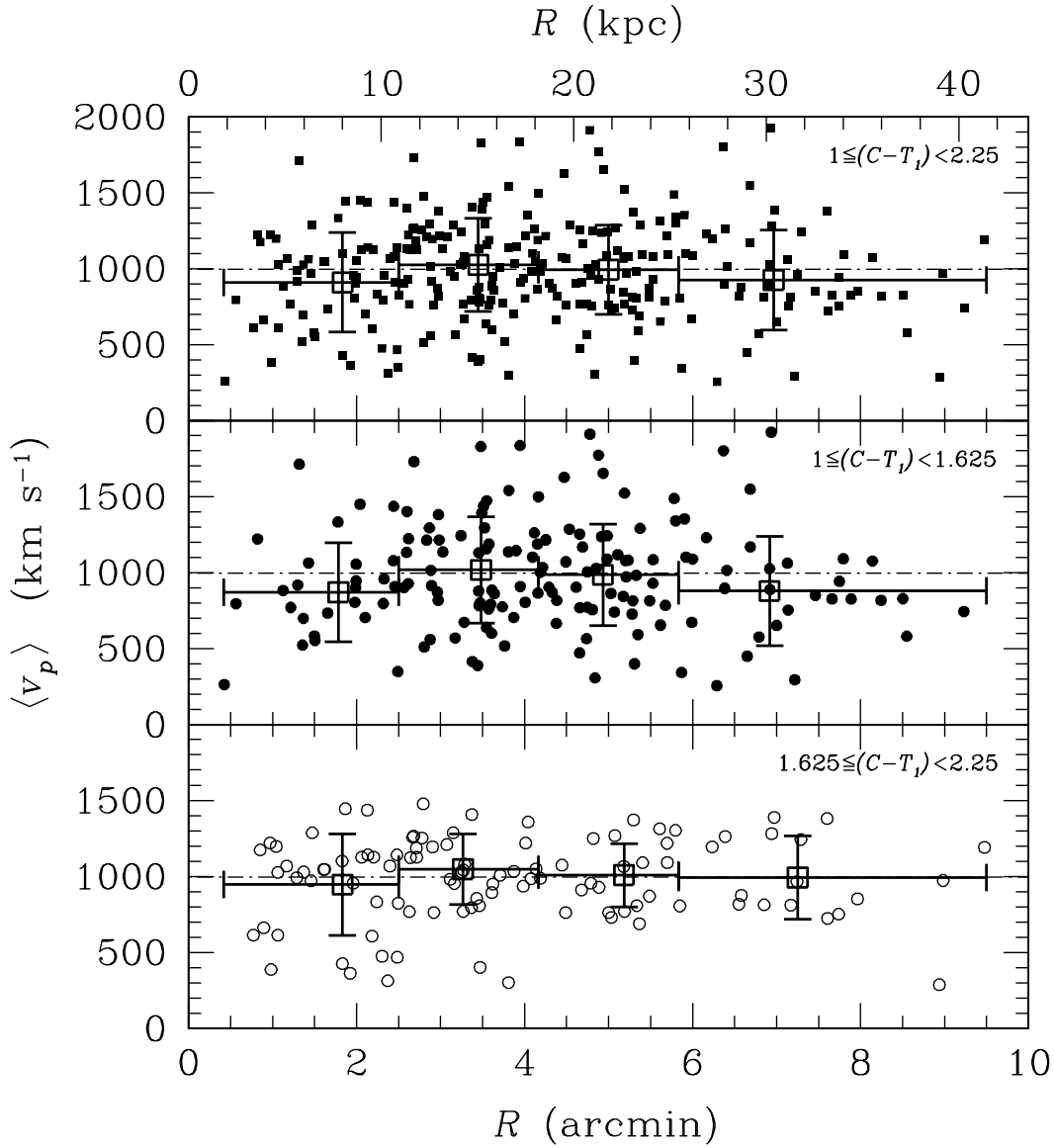


Fig. 5.— (*Upper Panel*) Radial velocity, $\langle v_p \rangle$, plotted against projected galactocentric distance, R , for the full sample of 263 globular clusters. The broken horizontal line shows the velocity of M49. (*Middle Panel*) $\langle v_p \rangle$ versus R for the sample of 158 metal-poor clusters. (*Lower Panel*) $\langle v_p \rangle$ versus R for the sample of 105 metal-rich globular clusters. In each panel, the large, open squares are at the median R and average velocity, \bar{v}_p , of the globular clusters in the four coarse radial bins of Table 3. Horizontal errorbars define the limiting radii of the bins, and vertical errorbars represent the velocity dispersion, σ_p , in each bin.

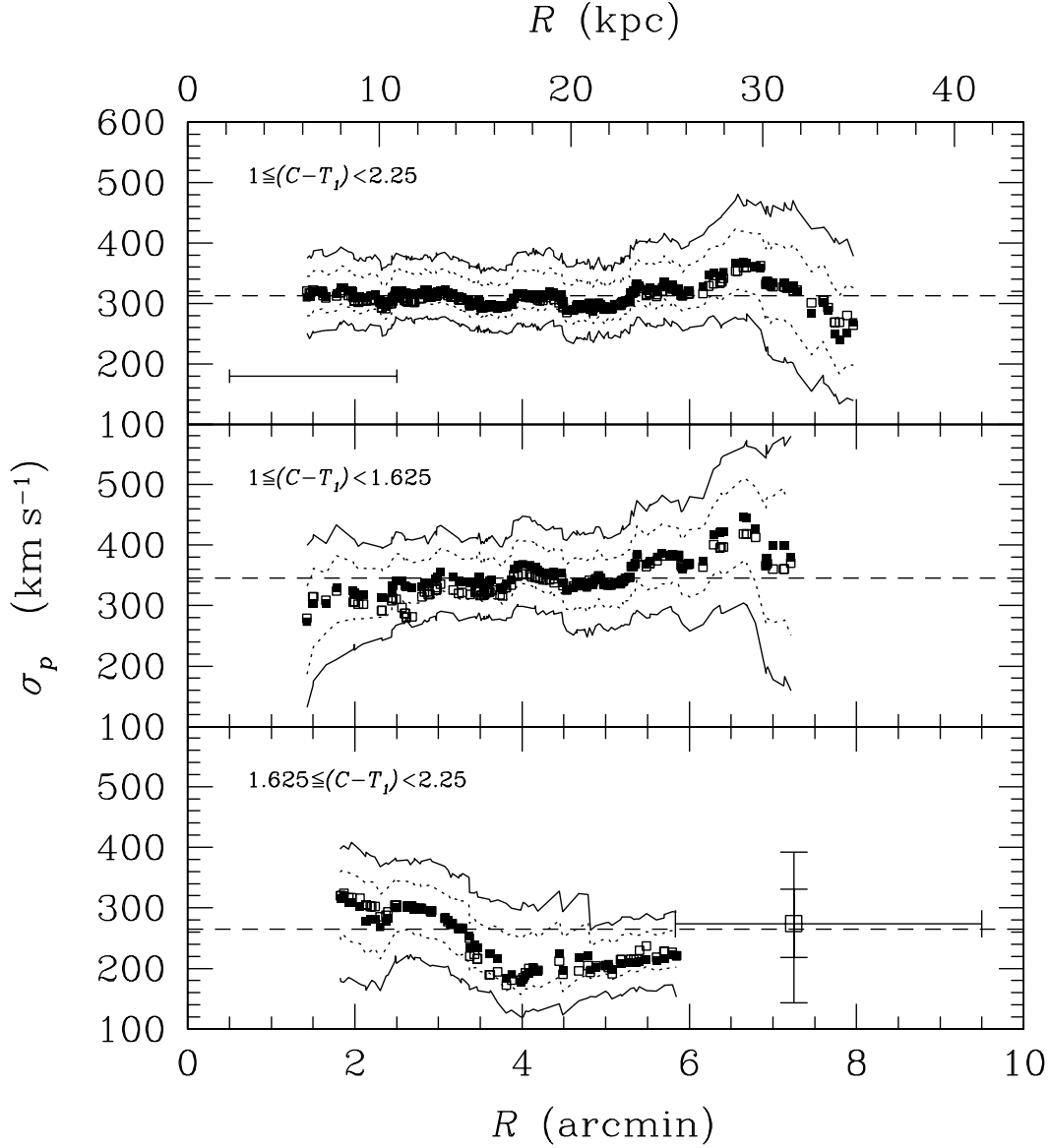


Fig. 6.— (*Upper Panel*) Biweight estimates of velocity dispersion as a function of galactocentric radius in the full sample of 263 M49 globular clusters. Solid squares represent the dispersion, σ_p , about the average globular cluster velocity at each point; open squares show the dispersion, $\sigma_{p,r}$, about the best-fit sine curve describing the variation of $\langle v_p \rangle$ with Θ at each radius. Dotted and solid lines around the points delineate the 68% and 95% confidence intervals on the dispersion estimates. The dashed horizontal line shows the global value of the velocity dispersion for the sample, and the horizontal errorbar shows the width ($2' \simeq 8.7$ kpc) of the sliding radial bin used to compute this smoothed profile. (*Middle Panel*) As above, but for the 158 metal-poor globular clusters. (*Lower Panel*) As above, but for the 105 metal-rich clusters. Also shown is a large open square representing the single bin containing the 18 metal-rich globular clusters beyond $R = 350'' \simeq 25.5$ kpc.

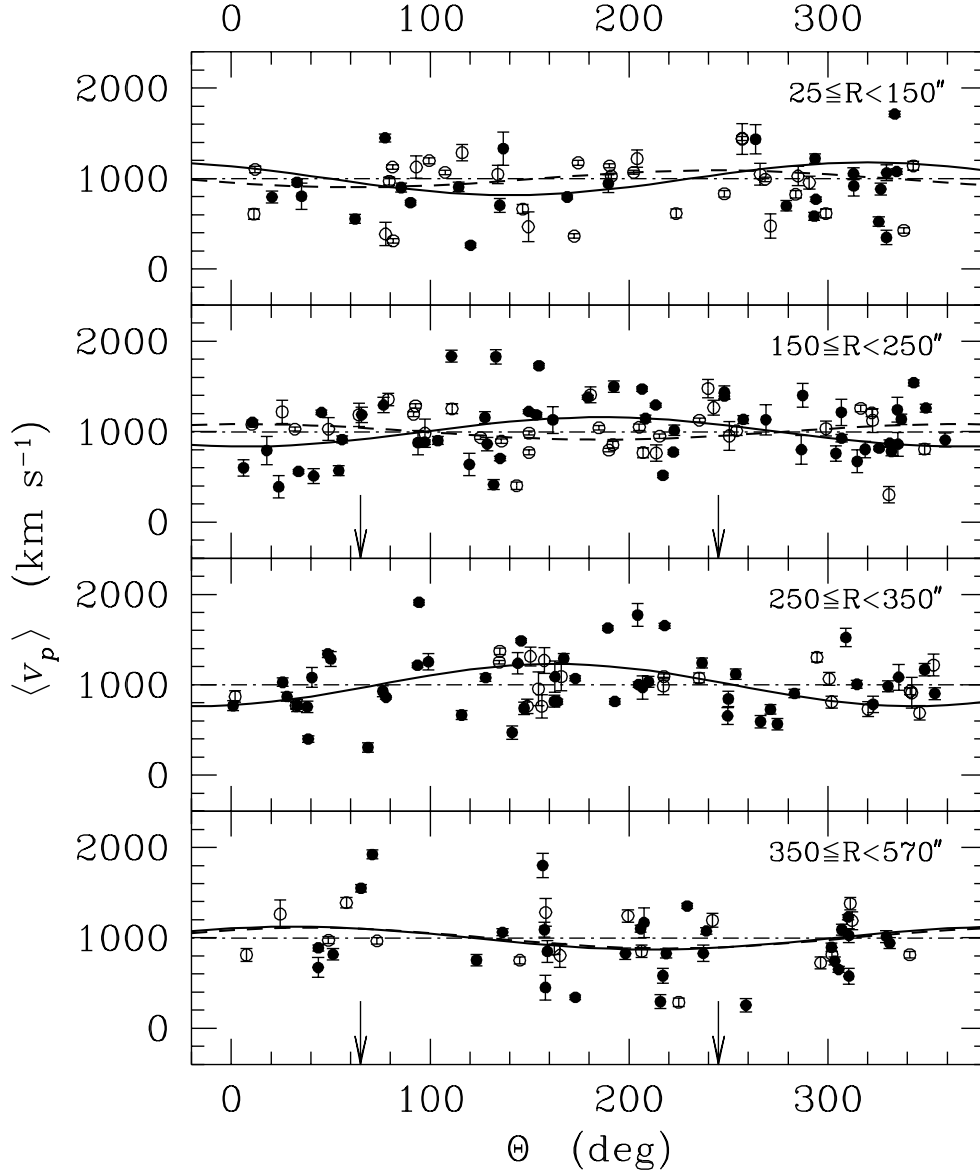


Fig. 7.— Radial velocity versus projected position angle for metal-poor and metal-rich globular clusters (filled and open points) in each of the four coarse radial bins whose kinematics are summarized in Table 3. The broken, horizontal lines in each panel represent the systemic velocity of M49. The bold solid and dashed curves are the sine curves that best fit the data for the metal-poor and metal-rich globular clusters (with parameters taken from Table 3). Vertical arrows in the second and bottom panels mark the position angle of the galaxy’s photometric minor axis ($\Theta = 65^\circ$ and 245°).

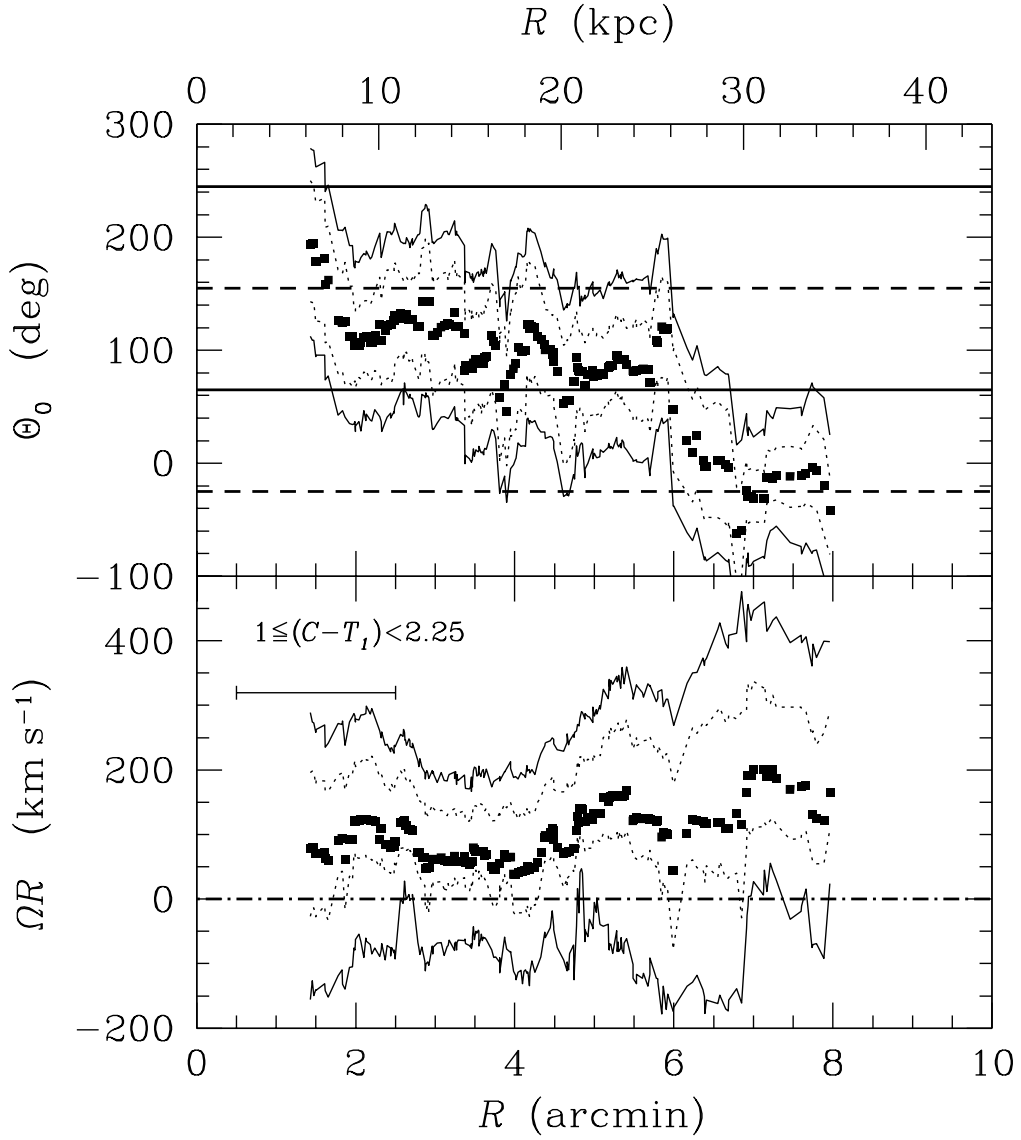


Fig. 8.— (*Upper Panel*) Projected position angle of the rotation axis of the globular cluster system of M49 (all metallicities), as a function of galactocentric radius. The bold, solid lines at $\Theta_0 = 65^\circ$ and 245° represent the minor axis of the galaxy light; bold, dashed lines at $\Theta_0 = -25^\circ$ and 155° , the photometric major axis. 68% and 95% confidence bands for the fitted Θ_0 are shown as dotted and solid lines around the points. (*Lower Panel*) Projected amplitude of rotation as a function of radius for the full globular cluster sample. The 68% and 95% confidence bands are indicated as in the upper panel, and the horizontal errorbar has a width of $2'$: the size of the sliding radial bin used to construct the profiles.

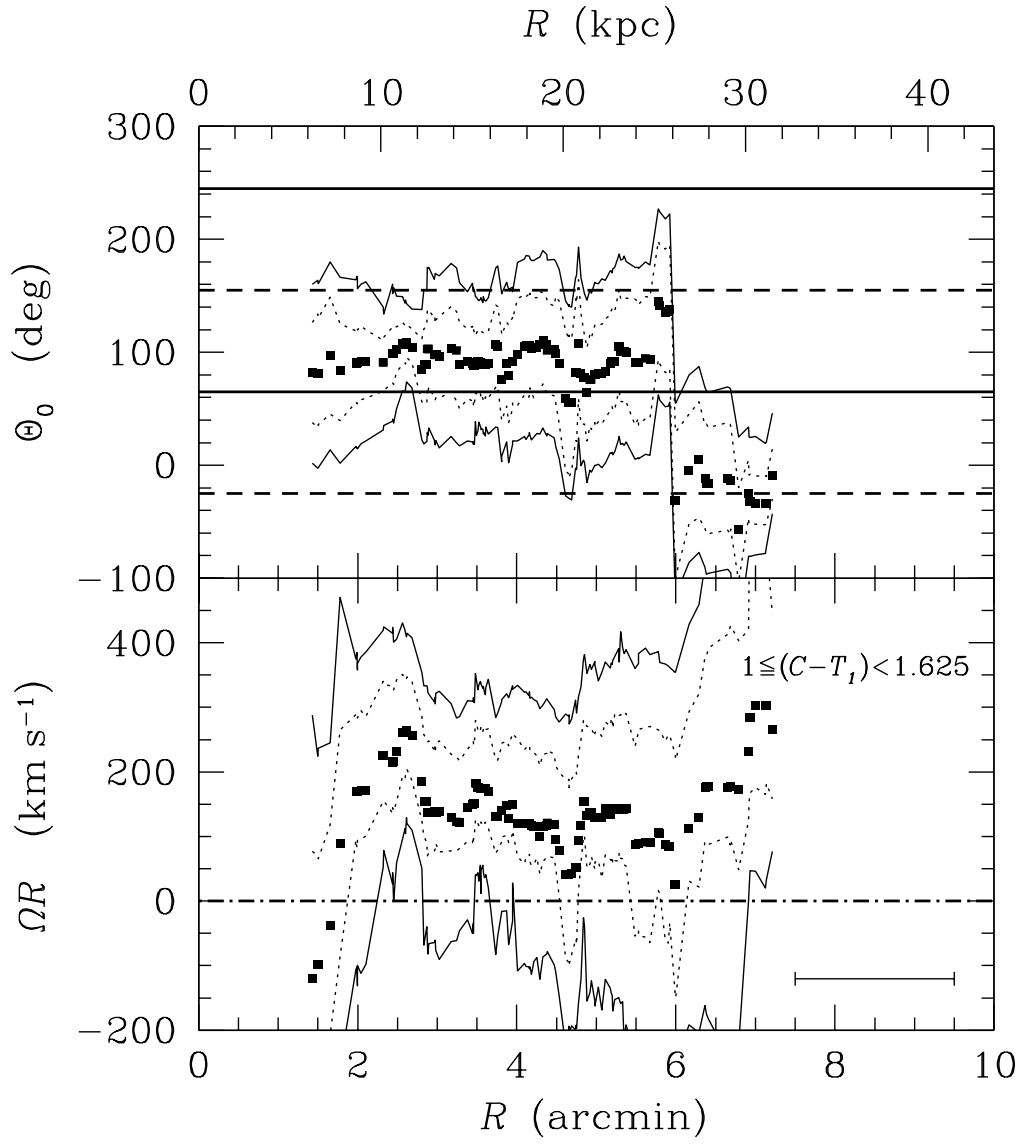


Fig. 9.— Same as Figure 8, but for the metal-poor globular clusters.

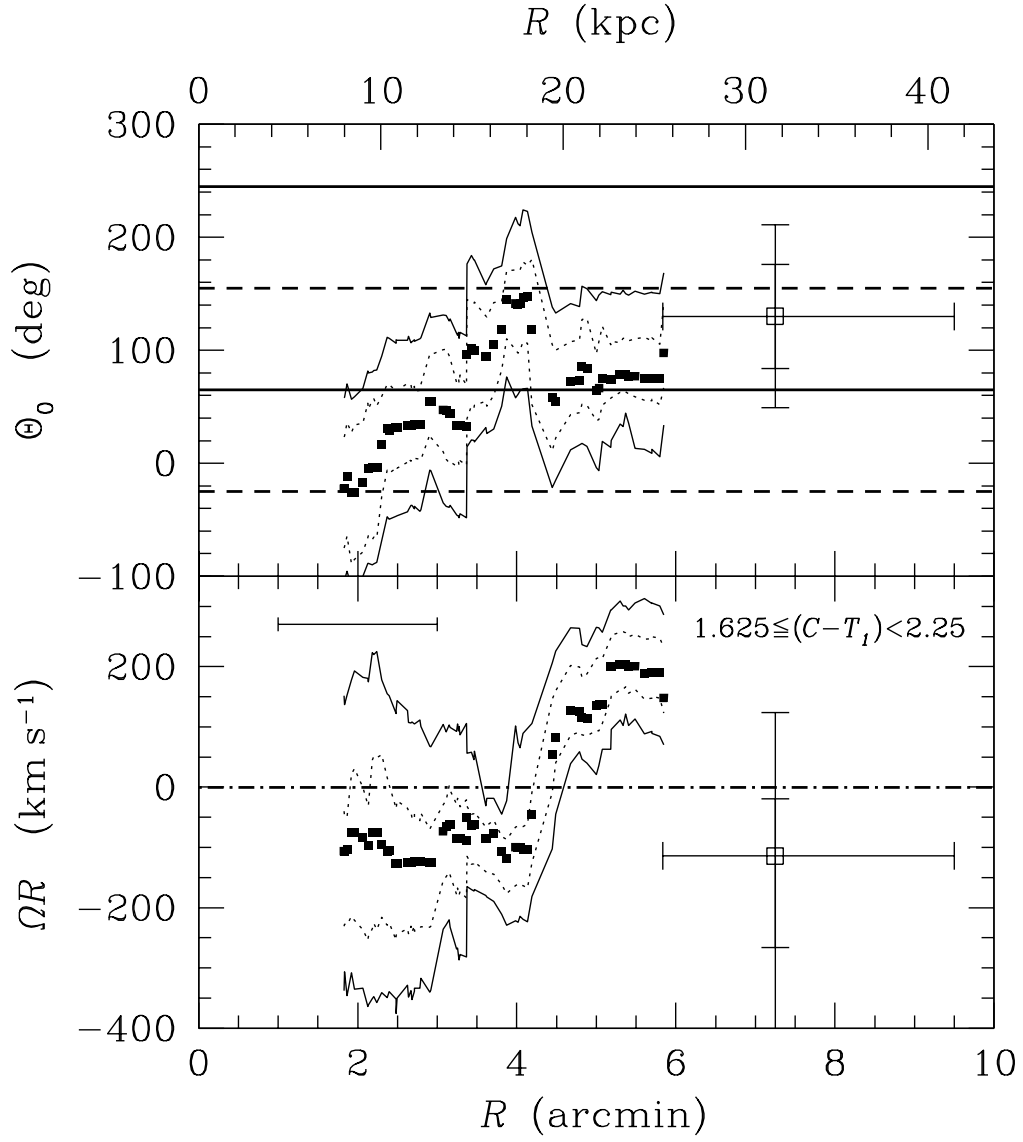


Fig. 10.— Same as Figure 8, but for the metal-rich globular clusters. Also shown, as the large open squares, are the best-fit Θ_0 and ΩR , with 1- and 2- σ errorbars, in the wide, outermost radial bin of Table 3.

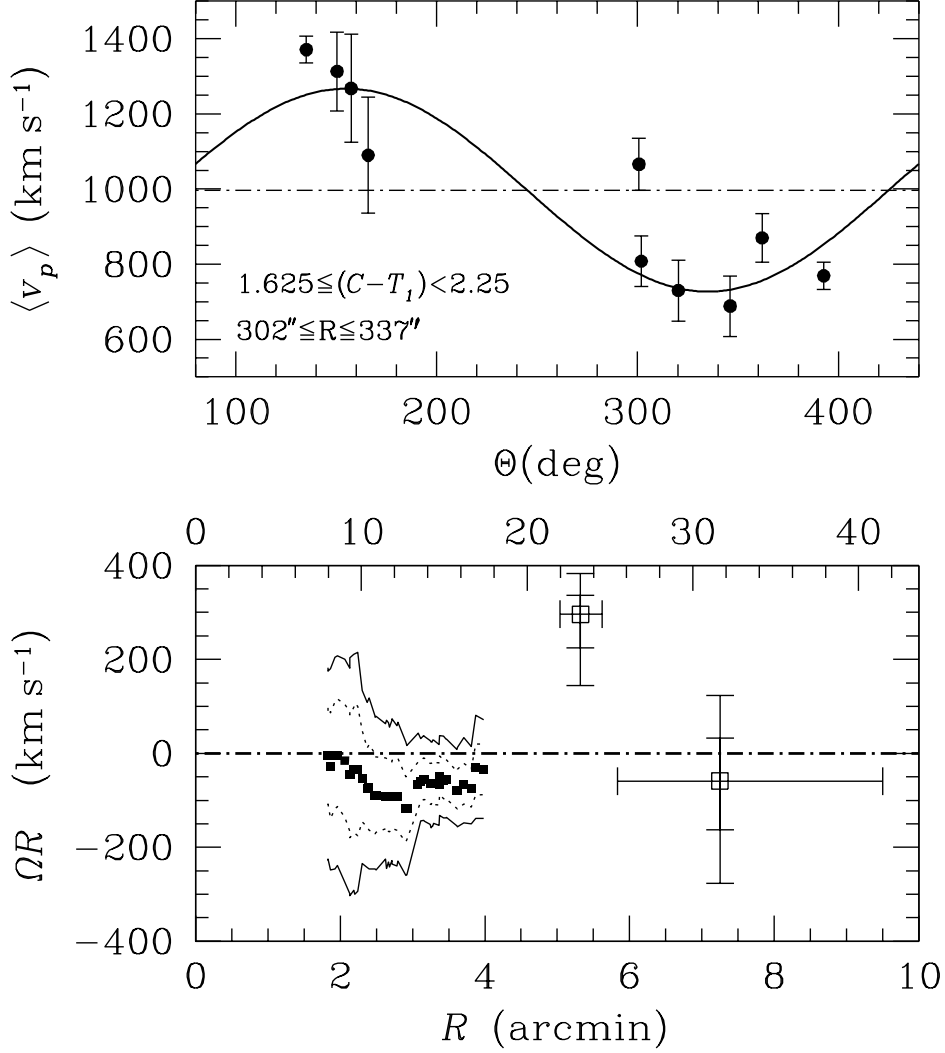


Fig. 11.— *Upper Panel*) Detection of strong rotation from 10 metal-rich globular clusters within a narrow range of galactocentric radius, $22 \leq R \leq 24.5$ kpc. The sine curve drawn has a zero at the photometric minor axis of the galaxy, *i.e.*, $\Theta_0 = 245^\circ$ (Kim *et al.* 2000), and an amplitude of 296 km s^{-1} (with $1\text{-}\sigma$ uncertainties of $+50 \text{ km s}^{-1}$ and -70 km s^{-1} ; and $2\text{-}\sigma$ uncertainties of $+90 \text{ km s}^{-1}$ and -150 km s^{-1}). *Lower Panel*) Projected rotation amplitude as a function of galactocentric radius in the metal-rich globular cluster system, for fits of the sine curve in equation (5) with both the systemic velocity held fixed (at the velocity of M49 itself) and the position angle of the rotation axis forced to coincide with the photometric minor axis of the galaxy. The smoothing process of Figure 10 is used only on those globular clusters with $R < 302'' = 22$ kpc. The large point at $R = 5.3$ and $\Omega R = 296 \text{ km s}^{-1}$ represents the 10 globular clusters isolated in the upper panel, while that at $R = 7.25$ and $\Omega R = -59 \text{ km s}^{-1}$ represents the sine fit with v_{sys} and Θ_0 both fixed in the outermost radial bin, $350'' \leq R < 570''$.

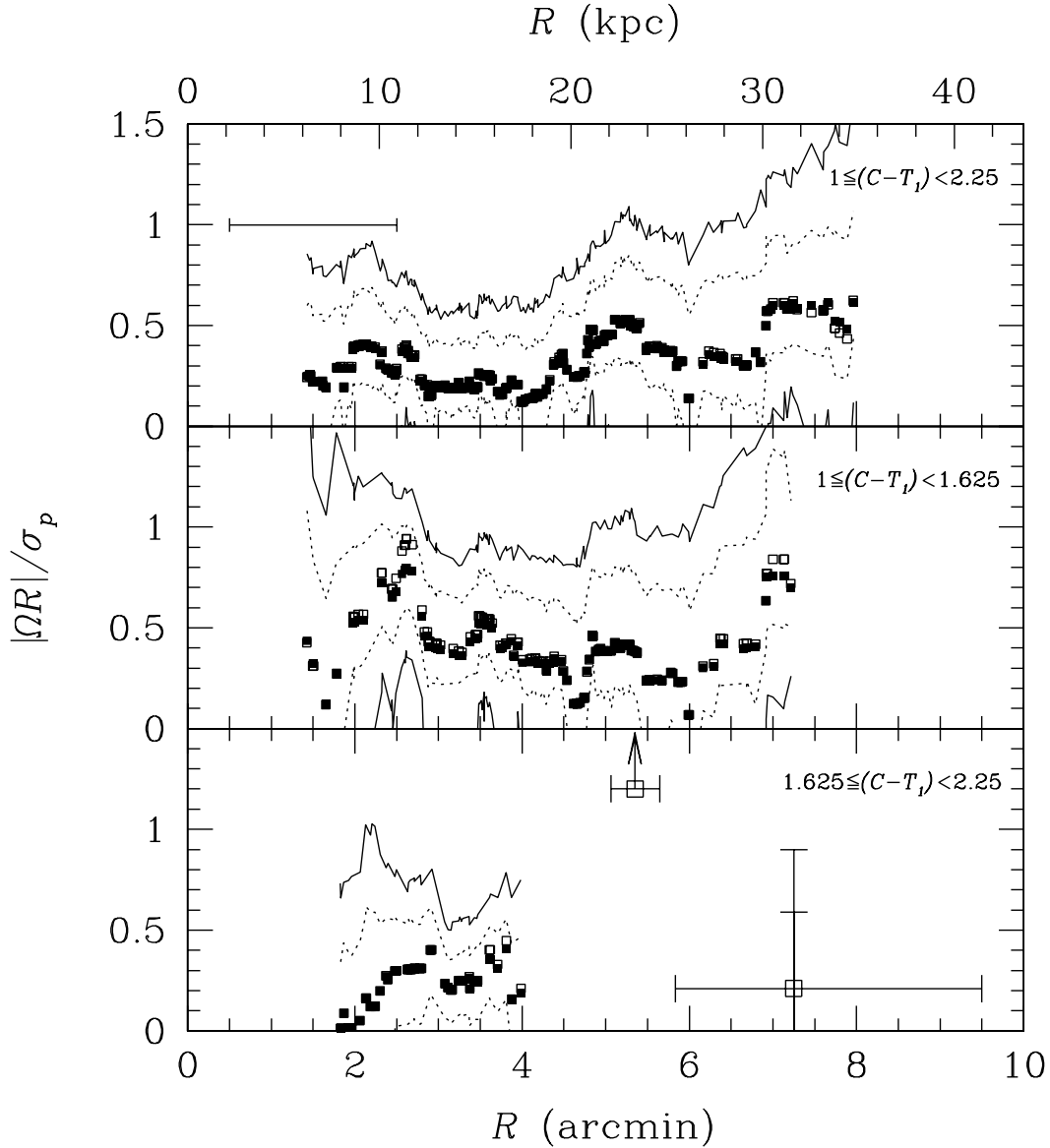


Fig. 12.— (*Upper Panel*) Ratio of the projected rotation amplitude to the line-of-sight velocity dispersion for M49 globular clusters, plotted as a function of distance from the galaxy center. Filled points take the ratio relative to the dispersion, σ_p , about the average globular cluster velocity; open points use the dispersion, $\sigma_{p,r}$, about the best fit of equation (5) at every radius. The horizontal errorbar shows the $2'$ width of the sliding radial bin used to “smooth” the data. (*Middle Panel*) As above, but for the metal-poor globular clusters. (*Lower Panel*) As above, but for the metal-rich globular clusters. The rotation amplitude in question is taken from the lower panel of Figure 11 rather than that in Figure 10. The large open square represents the 10 rapidly rotating, metal-rich globular clusters in the upper panel of Figure 11. For these objects, $|\Omega R|/\sigma_p = 1.2$; the corresponding rotation-corrected value is $|\Omega R|/\sigma_{p,r} = 2.9$.

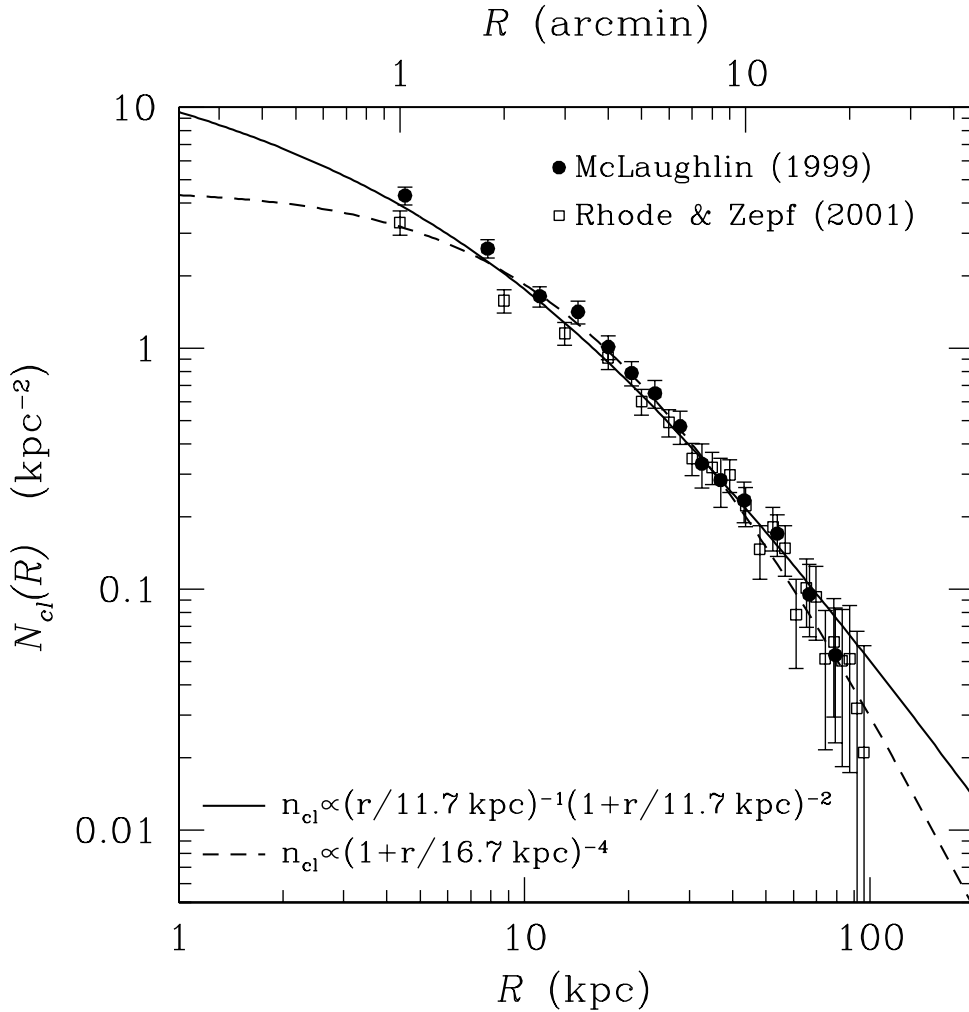


Fig. 13.— Projected number-density profile for the M49 globular cluster system. Filled circles are data compiled by McLaughlin (1999a); open squares come from the independent study of Rhode & Zepf (2001). Both profiles already include all scalings and corrections to account for background and foreground contamination, and for photometric incompleteness in the relevant globular cluster number counts. Solid line shows the best fit of a projected three-dimensional law of the NFW form, as indicated on the graph. The broken curve is the best-fitting projection of one of the family of density models developed by Dehnen (1993). (See also eqs. [9] and [10] in the text.)

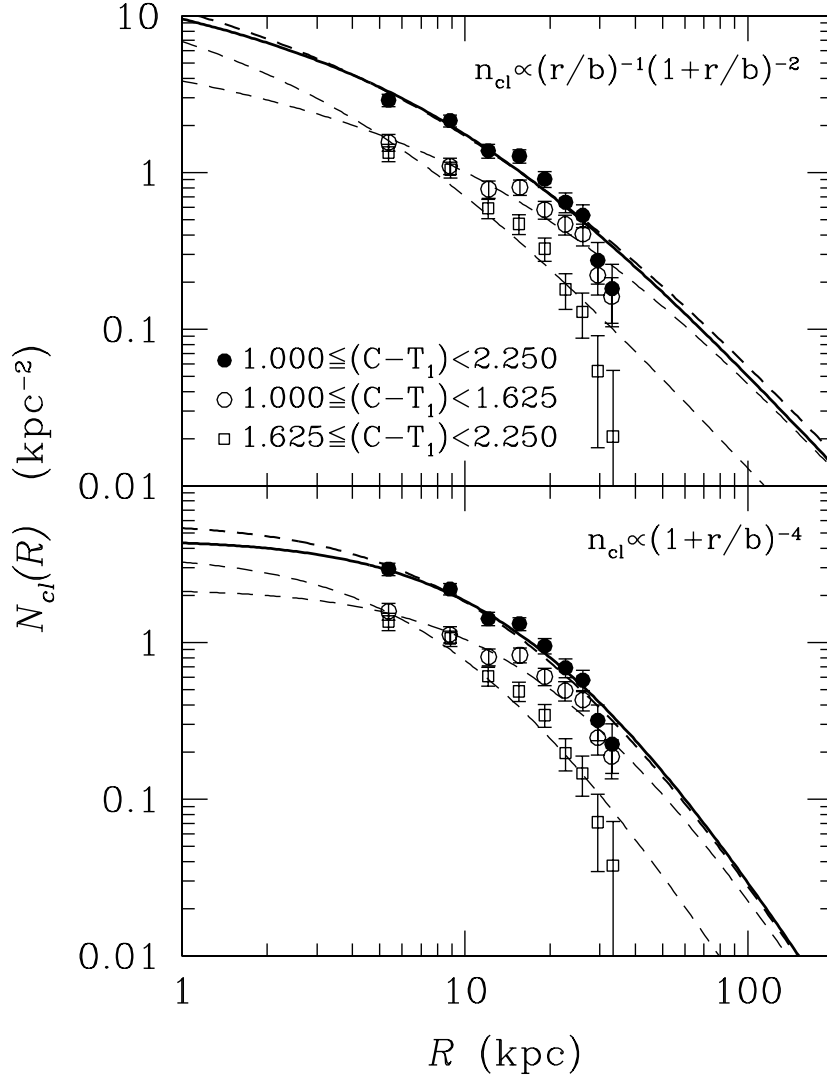


Fig. 14.— Fits to the projected number-density profiles of metal-poor and metal-rich globular clusters in M49 (open circles and squares), defined by us from the catalog of Lee *et al.* (1998), for two assumed functional forms of the three-dimensional $n_{cl}(r)$ (see eqs. [11] and [12]). See the text for a description of the various curves.

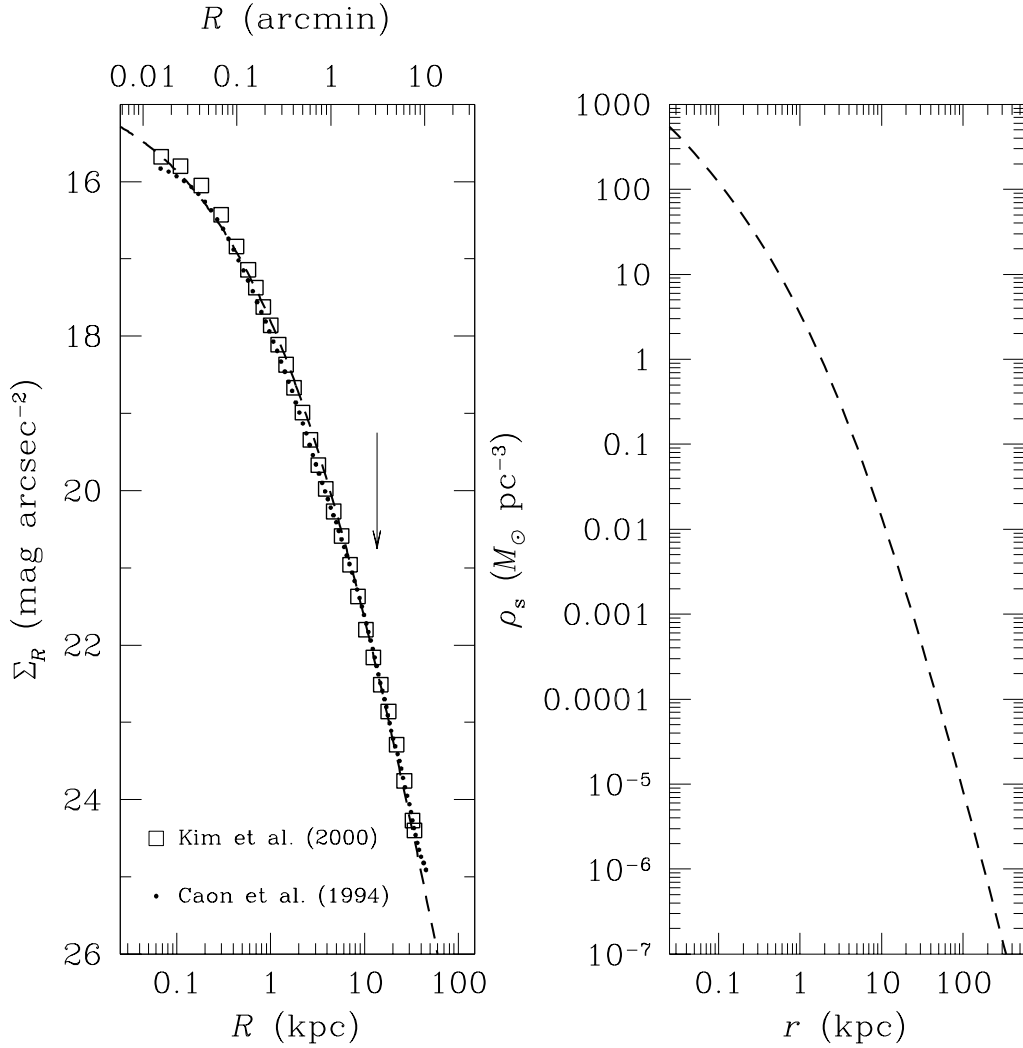


Fig. 15.— (Left Panel) R -band surface brightness profile for M49 (open squares) derived from the CT_1 photometry of Kim *et al.* (2000). The dashed curve is the best fit, in projection, of the model in equation 13. Dots show the B -band surface brightness profile of Caon *et al.* (1994) after shifting by the mean galaxy color of $\langle B - R \rangle = 1.52$. The arrow shows our estimate for the galaxy’s effective radius, $R_{\text{eff}} = 3'1$. (Right Panel) Three-dimensional stellar mass density profile corresponding to the model shown in the previous panel, for a spatially constant stellar mass-to-light ratio of $\Upsilon_0 = 5.7 M_{\odot} L_{R,\odot}^{-1}$ in the R -band (see §4.3).

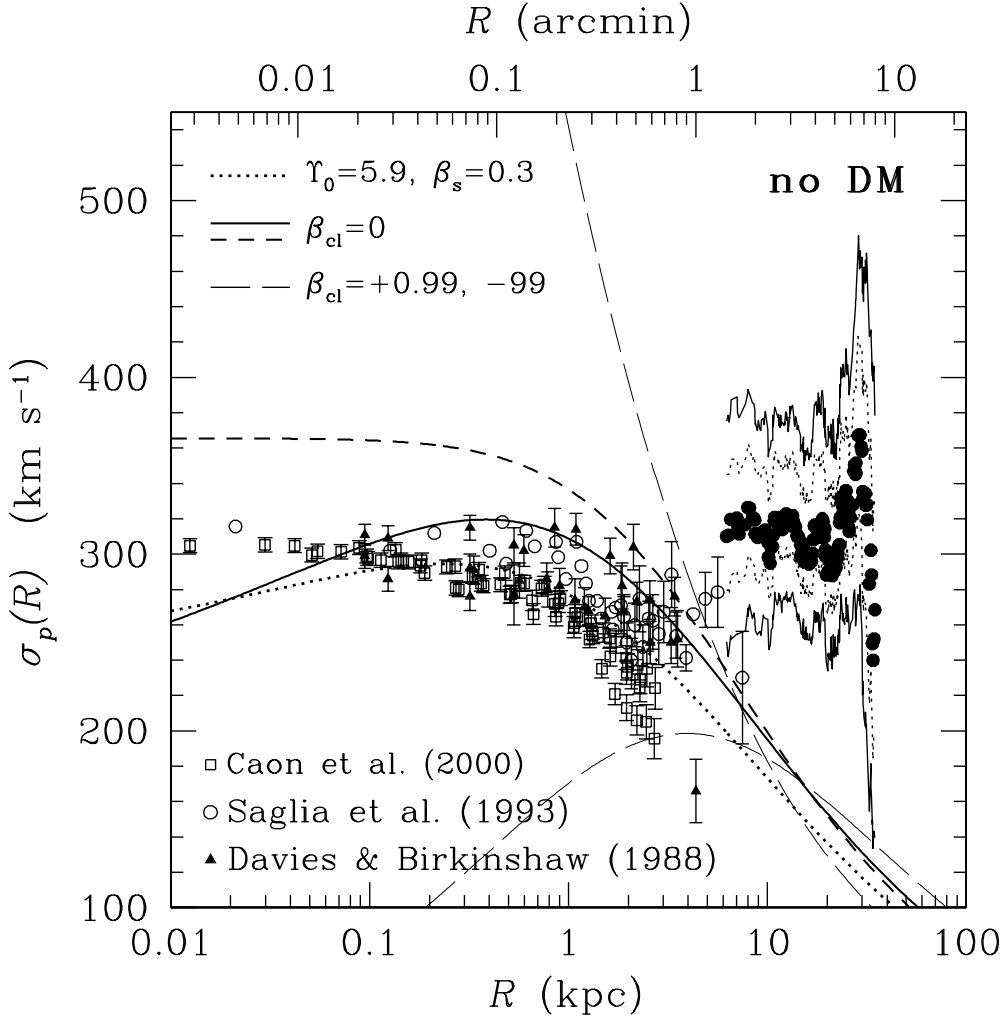


Fig. 16.— Evidence from the motions of its globular clusters that M49/Virgo B must contain a massive dark halo. Data points at small galactocentric radii are stellar velocity-dispersion measurements from Davies & Birkinshaw (1988), Saglia *et al.* (1993), and Caon *et al.* (2000). Filled circles show our velocity dispersion profile for the full sample of globular clusters, taken from the upper panel of Figure 6. The heavy, dotted curve is the stellar velocity dispersion profile that would be produced in a self-consistent galaxy model: *i.e.*, one with no dark-matter halo, a constant R -band mass-to-light ratio of $\Upsilon_0 = 5.9$ in solar units and a stellar velocity anisotropy $\beta_s = 0.3$. The heavy solid line is the velocity dispersion profile predicted for the full globular cluster system in such a model, if the density profile $n_{cl}(r)$ is given by equation (9) and an isotropic velocity dispersion is assumed. Lighter, long-dashed curves refer to models incorporating strong radial and tangential velocity anisotropy in the globular cluster system. The heavy, dashed line is the prediction for an isotropic globular cluster system if $n_{cl}(r)$ is given instead by equation (10).

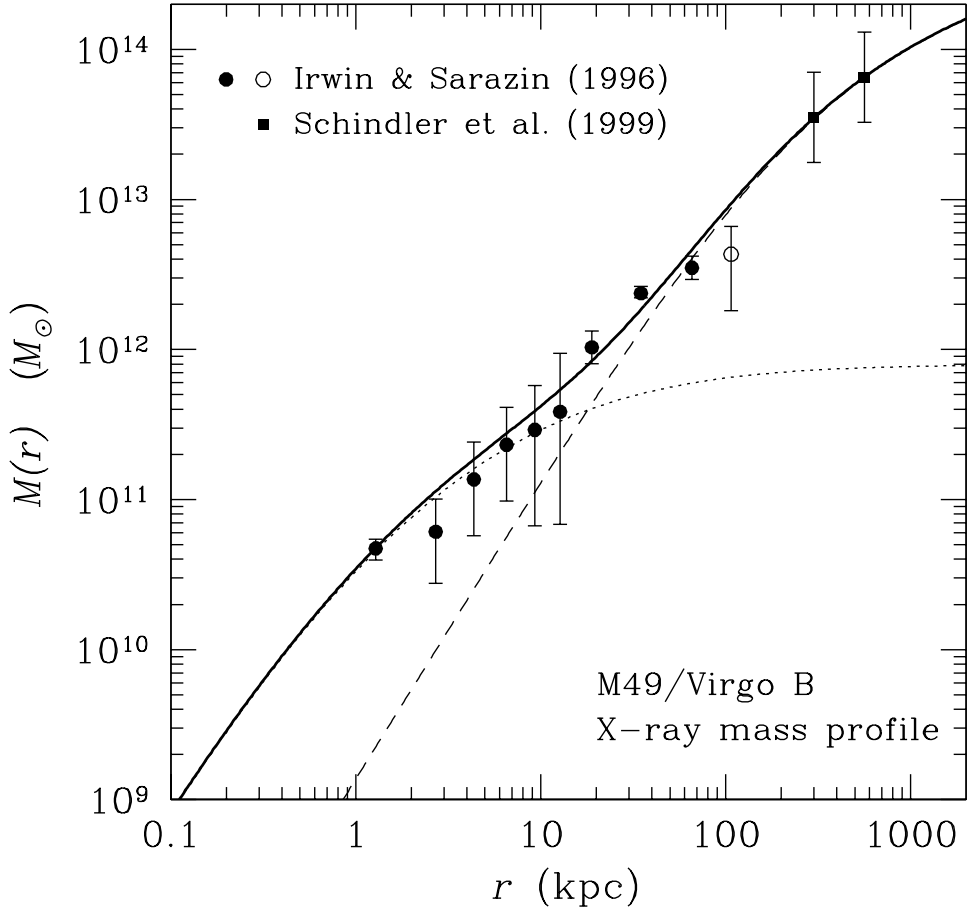


Fig. 17.— Adopted mass model for M49 and the surrounding Virgo B subcluster, from McLaughlin & Côté (2003). Dotted and dashed curves show the separate mass profiles for the galaxy and the surrounding dark matter halo; their sum is the total gravitating mass, $M_{\text{tot}}(r)$, drawn as the bold, solid curve. See equation (16) of the text for details. Points represent the X-ray mass measurements used to fit the model: filled circles are from Irwin & Sarazin (1996), with $2\text{-}\sigma$ errorbars indicated (and one point not used in the fit shown as an open circle), while squares are from Schindler *et al.* (1999) with approximate, factor-of-two errorbars attached.

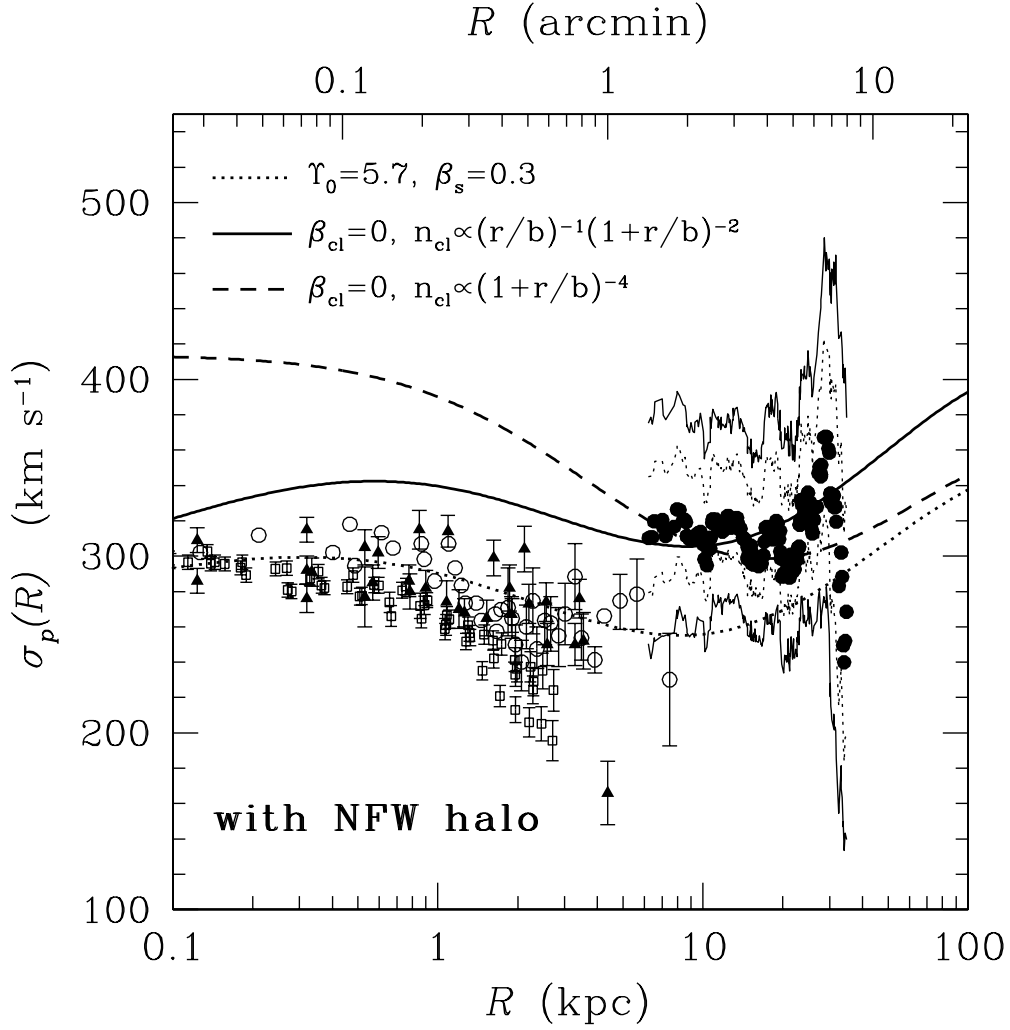


Fig. 18.— Comparison of the observed stellar velocity dispersion profile (symbol types as in Figure 16) with the predicted profile (heavy, dotted curve) given the mass model of Figure 17 and equation (16), for a stellar velocity anisotropy $\beta_s = 0.3$. Velocity dispersion data for the full globular cluster system are shown as filled circles, with 68% and 95% confidence bands indicated. The bold solid and dashed curves are predicted $\sigma_p(R)$ profiles for the globular cluster system assuming an isotropic velocity ellipsoid and adopting the density-profile fits of equations (9) and (10).

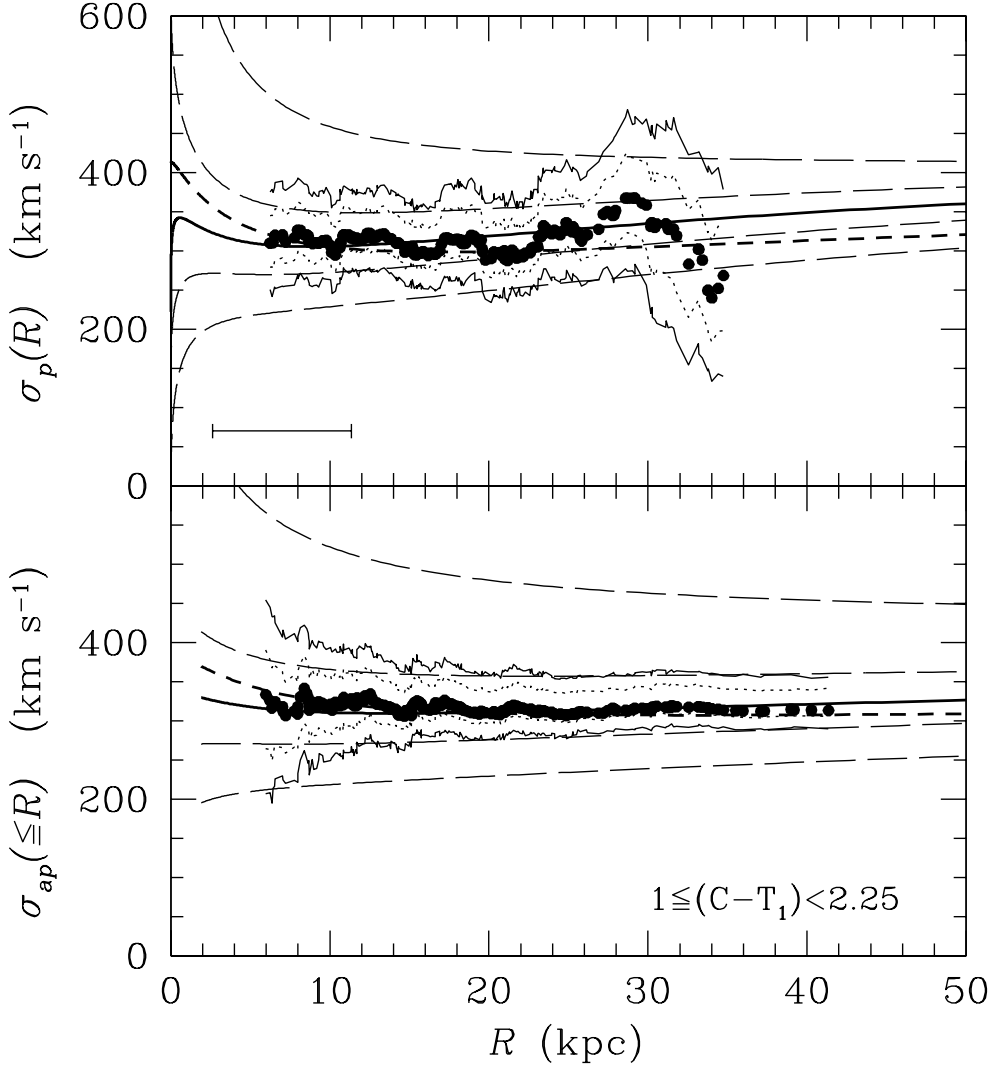


Fig. 19.— (*Upper Panel*) Velocity dispersion profile, $\sigma_p(R)$, for the full sample of 263 globular clusters along with bootstrap estimates of the 68% and 95% confidence intervals (from Figure 6). The heavy solid curve is the predicted profile for clusters that are embedded in the mass distribution given by equation (16), follow the density profile of equation (9), and have an isotropic velocity dispersion tensor. Lighter, long-dashed curves vary the assumption on the velocity anisotropy: from top to bottom, $\beta_{cl}(r) \equiv 0.99, 0.5, -1, \text{ and } -99$. The bold, short-dashed curve is a model assuming isotropy but using the fit of equation (10) to $n_{cl}(r)$. The horizontal errorbar in the lower left corner represents the $2'$ smoothing width used to construct the empirical profile. (*Lower Panel*) Aperture velocity dispersion profile for the complete sample of globular clusters. Smooth curves are the models of the upper panel, spatially averaged through equation (17) in the text.

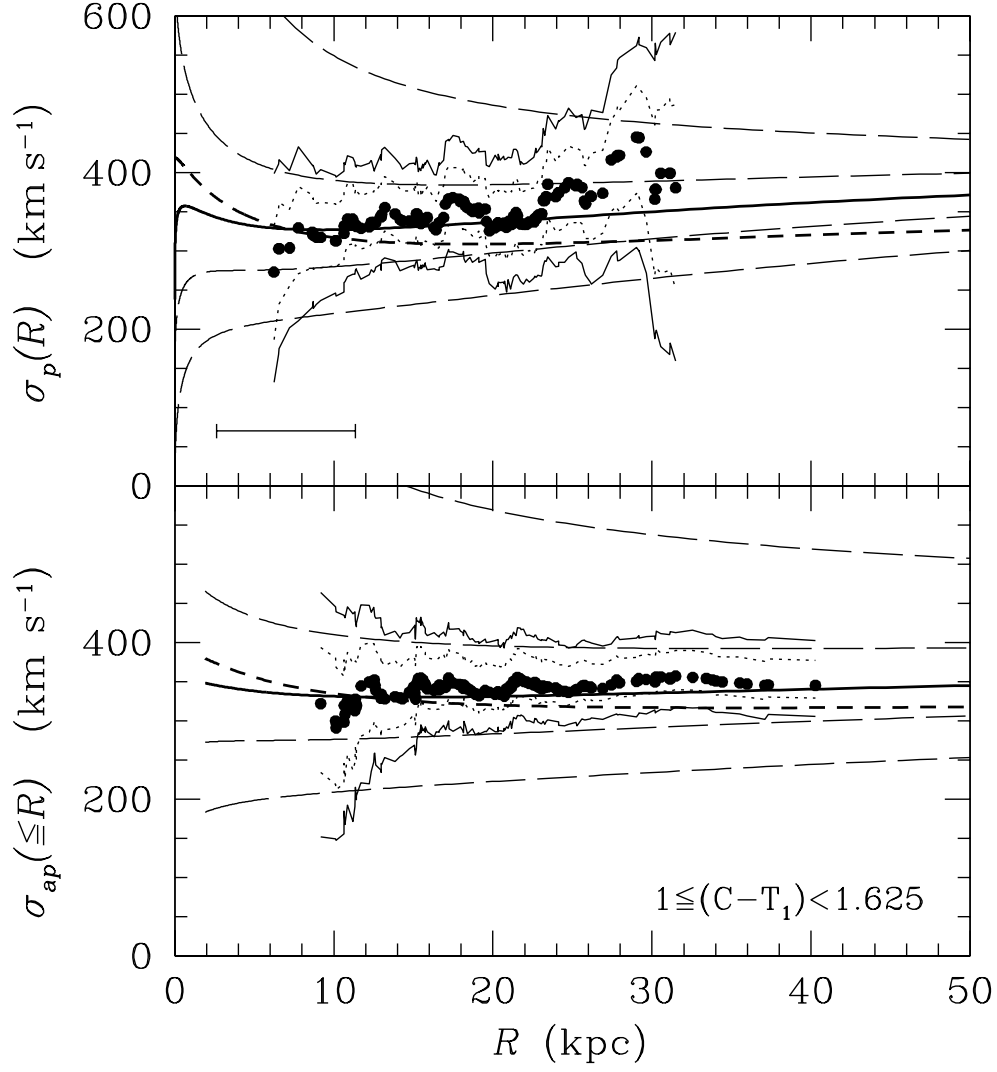


Fig. 20.— Similar to Figure 19, except for the sample of 158 metal-poor globular clusters. Model curves now use the density-profile fits for $n_{\text{cl}}^{\text{MP}}(r)$ in equations (11) (bold solid and light, long-dashed curves) and (12) (bold, short-dashed curves).

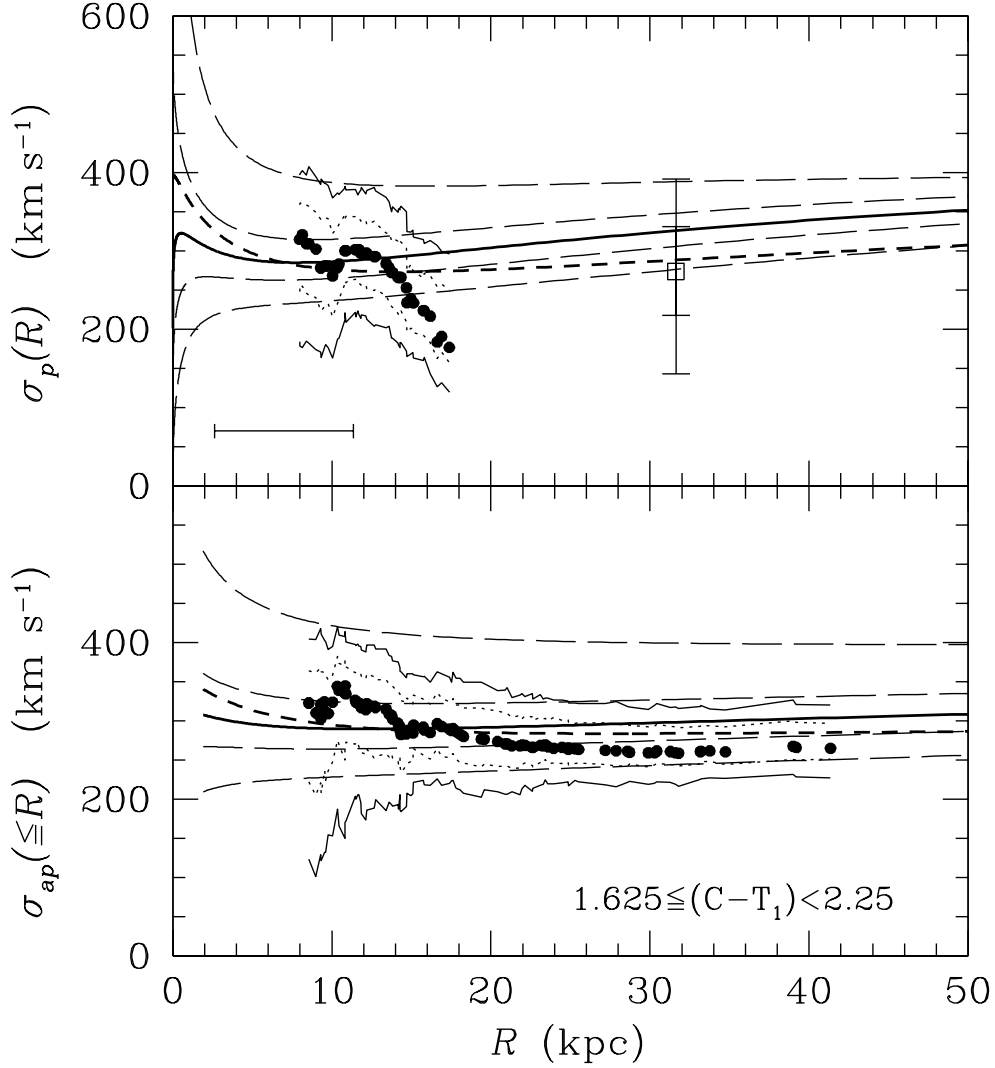


Fig. 21.— Similar to Figures 19 and 20, but for a sample of metal-rich globular clusters. Objects with $300'' < R < 350''$ ($21.8 \text{ kpc} < R < 25.5 \text{ kpc}$) are excluded from the data in the upper panel, though not from the spatially averaged, aperture dispersion profile in the lower panel. The large, open square in the upper panel represents the velocity dispersion (with 1- and 2- σ errorbars) of all metal-rich globular clusters beyond $R = 350'' = 25.5 \text{ kpc}$. Model curves are analogous to those in the previous Figures but employ the density-profile fits for $n_{\text{cl}}^{\text{MR}}(r)$ in equations (11) (bold solid and light, long-dashed curves) and (12) (bold, short-dashed curves).